Propagating kink waves in the solar corona

Ajay K Tiwari

Supervisor: Prof. James A. McLaughlin

Department of Mathematics, Physics and Electrical Engineering
University of Northumbria at Newcastle

A thesis submitted in partial fulfilment of the requirements for the degree of
Doctor of Philosophy

May 2020

Propagating kink waves in the solar corona

AJAY KUMAR TIWARI

A thesis submitted in partial fulfilment
of the requirements of the
University of Northumbria at Newcastle
for the degree of
Doctor of Philosophy
Research undertaken in the
Department of Mathematics, Physics and Electrical Engineering

Friends and family

Declaration

I hereby declare that except where specific reference is made to the work of others, the contents of this thesis are original and have not been submitted in whole or in part for consideration for any other degree or qualification in this, or any other university. This thesis is my work and contains nothing which is the outcome of work done in collaboration with others, except as specified in the text and acknowledgments.

Any ethical clearance for the research presented in this thesis has been approved. Approval has been sought and granted by the Faculty Ethics Committee on 16 March 2018.

I also declare that the word count of this thesis is 31,593 words.

May 2020 .....

Ajay K Tiwari .....
Signature .....

Acknowledgements

This thesis would not have been possible without the support of so many people over the course of the last three years. Firstly to my supervision team at the Northumbria University. My supervisors James McLaughlin and Richard Morton have always been available for my queries, whether about MHD or some silly programming bug. They gave me an opportunity to pursue a thesis and I am ever so grateful. The Northumbria community including Stephane, Eamon, Shaun and Patrick helped me with several discussions and talks about solar physics and the PhD experience. My master's thesis supervisor Dipankar Banerjee and Prasad Subramanian for my solar physics knowledge and constant advice. I would also like to extend my gratitude to the IT team at Northumbria University especially the Linux group, thank you for your support.

The work would not have been achievable without the much cherished public data. I would like to extend my gratitude to the people maintaining data archives at MLSO. I would also like to thank the AIA and HMI science teams. I would like to acknowledge the effort of teams associated with the various computational tools used, Anaconda (*Anaconda Software Distribution*, Computer software, Vers. 2-2.4.0, Anaconda, Nov. 2016), Astropy (Astropy Collaboration et al., 2013, 2018), IPython (Pérez & Granger, 2007), Jupyter (Kluyver et al., 2016; Morin et al., 2013), Matplotlib (Hunter, 2007), NumPy (Jones et al., 2001), pandas (pandas development team, 2020; Wes McKinney, 2010), Seaborn (Waskom et al., 2020), SolarSoft (Freeland & Handy, 1998), and SunPy (The SunPy Community et al., 2020; SunPy Community et al., 2015; Mumford et al., 2020b,a).

To my family, Daddy, Mummy, Sushma didi, Supriya, Ankita and Ankur, I will not have been here if it wasn't for you. I will try to meet your expectations, know that I love you and I miss you all dearly. My officemates at Northumbria University, André, Linh, Tom, Giacomo and Martha, contributed to discussions and helped me by accompanying me to a pub after a long week or after the bug between the human and the computer was discovered. The Newcastle experience would not have been the same without Anastasia, thanks for inspiring me to do salsa and for much needed coffee breaks. To the city of Newcastle, I can say I am pleasantly surprised that I like calling you home. I would like to thank the staff of the Royal Victoria Infirmary for getting me in shape after my TB diagnosis.

To a lot of people I met over the years and have lost touch but had an immediate intense connection, giving me solace of a kind, wherever you are I thank you and wish you are doing great. Hopefully we meet again sometime somewhere.

This work would not have been possible without the constant love and support of you, Shivangee, thank you so much for the physics conversations, you know you are the person I will come to if I have any python or physics doubts. You are my lobster. I apologise for the frustrating long distance fights. You inspire me, with you organisational skills, creativity, dedication, perseverance and humility, you are my rock. We will definitely go to Scotland for sure after this.

UNacknowledgements:

I would not like to thank *Mycobacterium tuberculosis* and COVID-19 both of these ruined my after party plans and took up more than a month of work. I am not going to miss the heavy dose of antibiotics.

Abstract

The solar atmosphere is known to host various modes of MHD waves. Transverse waves are thought to play an important role in energy transfer in the atmosphere and thus in solar coronal heating and the acceleration of the solar wind. The transverse waves studied so far have predominantly been interpreted as standing kink waves and, via coronal magneto-seismology, they can offer insight into the physical conditions of coronal plasmas. In addition, the excitation of these standing kink waves are associated with low coronal eruptions and thus need special conditions or drivers.

Propagating kink waves have been reported recently and have been found to be ubiquitous in the solar corona including in the quiet Sun. It is imperative to understand the mechanisms that enable their energy to be transferred to the plasma. Carrying on the legacy of the standing kink waves, mode conversion via resonant absorption is thought to be one of the main mechanisms for damping of these propagating kink waves, and is considered to play a key role in the process of energy transfer. The propagating kink waves are best observed in the Doppler velocity images of the Coronal Multi-channel Polarimeter (CoMP). The damping is observed using data from this instrument to study the energetics of the propagating kink waves in quiescent coronal loops.

A coherence-based method is used to track the Doppler velocity signal of the waves, enabling an investigation into the spatial evolution of velocity perturbations. To enable accurate estimates of these quantities, the first derivation is provided of a likelihood function suitable for fitting models to the ratio of two power spectra obtained from discrete Fourier transforms. Maximum likelihood estimation is used to fit an exponential damping model to the observed variation in power ratio as a function of frequency. This also confirms earlier indications that propagating kink waves are undergoing frequency-dependent damping. Additionally, it is found that the rate of damping decreases, or equivalently the damping length increases, for longer coronal loops that reach higher in the corona.

The analysis techniques are used to create a statistical sample of quiescent loops to study the statistical properties of propagating kink waves and compare it to the studies of standing kink waves. It is noted that the damping for the propagating waves appears to be significantly weaker than that found from measurements of

standing kink modes. The propagating kink waves also exhibit signatures of power amplification of waves.

Publications

- Tiwari, A. K., Morton, R. J., Régnier, S., & McLaughlin, J. A. 2019, The Astrophysical Journal, 876, 106

Outline

MHD waves in the solar atmosphere are one of the most important and widely studied features in the Sun. The MHD waves provide us with a unique opportunity to measure the physical properties of the coronal plasma. The coronal magneto-seismology techniques can be used to calculate the magnetic field of coronal loops. This thesis focuses on the study of propagating kink waves, their damping mechanism and their statistical properties. A comparative study of the propagating and standing kink waves is also conducted. The thesis is outlined as follows:

Chapter 1: Introduction

This chapter introduces the vast field of solar physics. A brief overview of the history of the field is presented. Some fundamental information about the Sun, the interior of the Sun and the solar atmosphere is discussed briefly. The important developments and the fundamentals of theory of magnetohydrodynamics are introduced. The analytical discussion about the MHD waves is presented as well.

Chapter 2: Overview of data sources and analysis techniques

The data sources and analysis are discussed in this chapter. The various instruments and telescopes that were used to obtain data for the study are briefly discussed. The analysis techniques such as the discrete Fourier transform, Fast Fourier transform, parameter estimation, maximum likelihood estimation are introduced briefly.

Chapter 3: Damping of Propagating Kink Waves in the Solar Corona

The propagating kink waves are explored and studied in this chapter. The statistics of the power ratio of kink waves are explored. The likelihood function for the ratio of two power spectra is derived, the use of this likelihood function is quite novel. The

damping mechanism is investigated, the results of which further support the claim that the damping of the propagating kink waves is via resonant absorption. The rate of damping is found to be dependent on the loop length. The need for a statistical study of these waves is emphasised.

Chapter 4: Statistical study of damping of kink waves

The statistics of the propagating kink waves is discussed. The distribution of various oscillation parameters is presented for the first time. The study also compares the statistics of propagating and standing kink waves in the solar atmosphere. The relation between the rate of damping and the loop length is explored, also including the standing kink waves.

Chapter 5: Conclusion and Future Work

The thesis is summarised and brief results are discussed. Future work and open research questions are discussed.

Table of contents

List of figures

Chapter 1

Introduction

ॐ भूर्भुवः स्वः
तत्सवितुर्वरेण्यं
भर्गो देवस्य धीमहि
धियो योनः प्रचोदयात्

Gayatri mantra, a hymn from the ancient sacred vedic text of Rigveda, 3.62.10 [11].

General meaning: We meditate on that most adored Supreme Lord, the creator, whose effulgence (divine light) illumines all realms (physical, mental and spiritual). May this divine light illumine our intellect.

1.1 The Sun

To our long lost ancestors, in whichever part of the globe they resided, the Sun would have appeared nothing more than a big ball of light and fire in the sky providing heat and causing day and nights. The motion of the Sun across the sky and its association with several phenomena must have been of interest to even the earliest of our civilisations, and they were based on several archaeological pieces of evidence and calendars that they left behind. This dependence of several aspects of civilisations on the Sun must have contributed to the Sun becoming the centre of mythology as it is today, cutting across geographical distances from Mesopotamia to Egypt, India to China, Inca to Maya. In recent times there has been an increasing interest in archeoastronomy, and there are pieces of evidence that support the claim that the ancient Chinese observers were probably one of the earliest to be able to record sunspots. Quite a handful of the civilisations also developed calendars based on the Sun. In Hindu mythology, the Sun *(*Surya) enjoys one of the most important positions. He was one of the most powerful gods of the ancient gods (Rigvedic gods). In the ancient religious Hindu texts, called Vedas, the Sun is mentioned as a god called *Surya*. *Surya* represents the Sun god, Figure 1.1. *Surya* is depicted as a red man with three eyes and four arms, riding in a chariot drawn by seven mares. *Surya* holds water lilies with two of his hands. With his third hand, he encourages his worshipers whom he blesses with his fourth hand. In India, *Surya* is believed to be a benevolent deity capable of healing sick people. Even today, people place the symbol of the Sun over shops because they think it would bring good fortune. When *Surya* married *Sanjna*, his wife could not bear the intense light and heat. Therefore, she fled into a forest where she transformed herself into a mare to prevent *Surya* from recognizing her. But *Surya* soon discovered *Sanjna's* refuge. He went to the same forest disguised as a horse. *Sanjna* gave birth to several children and eventually reunited with her husband. However, the heat and the light of Surya were so intolerable that *Sanjna* was always exhausted doing her domestic duties. Finally, *Sanjna's* father decided to help her and trimmed *Surya's* body reducing his brightness by an eighth. Thus, *Sanjna* could more easily live close to her husband. For a review of solar and stellar observations and mythologies, good sources include Olcott (1914); Tassoul & Tassoul (2004).

The telescope is one of humankind's most important inventions. The simple device that made far away things look near gave observers a new perspective. When curious men pointed the spyglass toward the sky, our view of Earth and our place in the universe changed forever. The first person to apply for a patent for a telescope was a Dutch eyeglass maker named Hans Lippershey (or Lipperhey). In 1608, Lippershey laid claim to a device that could magnify objects three times. His telescope had a concave eyepiece aligned with a convex objective lens. One story goes that he got

Fig. 1.1 The Sun temple situated in Konark, India, was built sometime during 13th-century CE.

the idea for his design after observing two children in his shop holding up two lenses that made a distant weather vane appear close. Others charged at the time that he stole the design from another eyeglass maker, Zacharias Jansen. It was, however, Galileo who changed the course of astronomy and arguably of our very civilisation with his telescope (Tassoul & Tassoul, 2004). When Galileo pointed his telescope at the Sun he could see it in great detail. The left panel in Figure 1.2 reveals some of the features of the solar disk, and just like that Sun was no more just a big ball of fire. The improvement in the technology of telescopes led to discoveries of various layers of atmosphere of the Sun. These developments paved the way for further discoveries including but not limited to, the sunspot cycle, active regions, solar flares and many more as we know today, with implications not only for solar physics but the early developments in astronomy as well. Even after the invention of telescopes, astronomy was considered a benign science. The birth of quantitative astrophysics can be attributed to Meghnad Saha who applied the concept of ionization equilibrium to astronomy. He was able to show how the degree of ionization of an atomic species is dependent on the temperature and pressure of the surrounding (Saha, 1921). The solar chromosphere became the first laboratory for Saha to experiment with his new theory.

Another such gem of astronomy is Cecilia Payne-Gaposchkin who, in her doctoral thesis (Payne, 1925), was able to accurately relate the spectral classes of stars

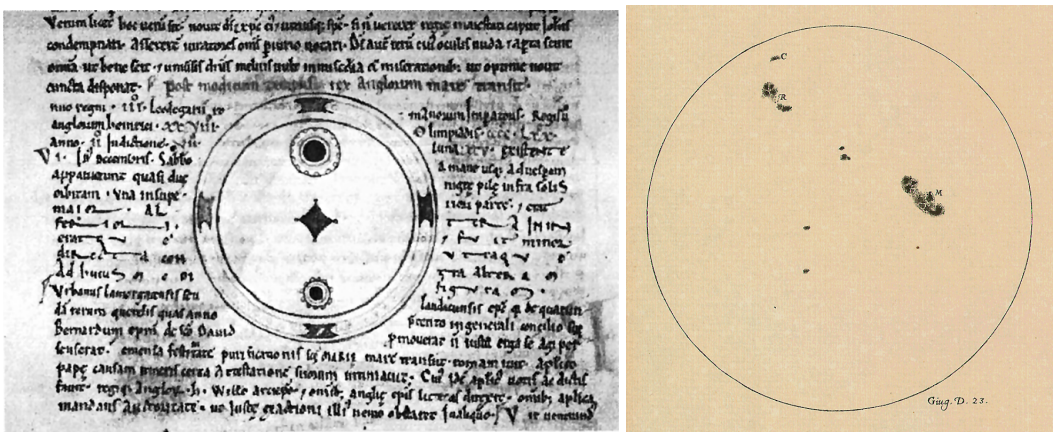

Fig. 1.2 *Left:* The earliest known record of a sunspot drawing in 1128, by John of Worcester. *'In the third year of Lothar, emperor of the Romans, in the twenty-eighth year of King Henry of the English...on Saturday, 8 December, there appeared from the morning right up to the evening two black spheres against the Sun.' Right:* Galileo's sunspot observation, also including some details.

to their effective temperatures. The effective temperature is the photospheric temperature that produces the general blackbody shape of the stars spectra. She showed that the great variation in stellar absorption lines was due to varying amounts of ionization at different temperatures and not due to different amounts of elements. She found that silicon, carbon, and other common metals are seen in the Sun's spectrum were present in about the same relative amounts as on Earth, in agreement with the accepted belief of the time, which held that the stars had approximately the same elemental composition as the Earth. However, contrary to the belief at that time she found that helium and particularly hydrogen were vastly more abundant. Her thesis challenged the strongly held view of the scientific community by concluding that hydrogen was the overwhelming constituent of stars, and thus is the most abundant element in the universe (Payne, 1925). The scientific understanding of the Sun has advanced by leaps and bounds, especially during the past six to seven decades. This is mainly due to the access of space as a frontier for solar observations, starting with Skylab and the more recent and ambitious missions focussed on the Sun. The removal of the Earth's atmosphere was a decisive step, allowing the observation of spectral lines not possible on Earth and vastly improving the quality of observational data. The progress in the solar physics community has been commendable, however, the three longstanding problems are yet to be resolved.

The study of the Sun can be broadly classified into two parts for convenience, the interior (Section 1.2) and the atmosphere (Section 1.3).

1.2 Solar interior

The physical structure of the solar interior is mostly based on theoretical models that are constrained (1) by global quantities (age, radius, luminosity, total energy output), (2) by the measurement of global oscillations (helioseismology), and (3) by the neutrino flux, which can constrain the elemental abundances in the solar interior since the neutrino problem has been solved in the year 2001. The Sun's internal structure can be divided into four sections; the core, the radiative zone, the tachocline and the convective zone. The regions are themselves hidden from our eyes. Figure 1.3 showcases the layered structure of the solar interior. The innermost layer called the core and follows all the other interior layers, the solar atmosphere and, as one moves radially outwards, follows all the way to the interplanetary medium. This understanding of the structure of the Sun and stars is built over decades of observations and improved mathematical models. For a more holistic historical perspective, Cowling (1966) is a very good place to start.

1.2.1 Core

The core is the innermost region of the Sun. The core holds more than 60% of the total mass of the Sun and reaching up to 25% of the total solar radius. The core has a density of around 1.5×10^5 kg m^{-3} and a temperature around 16 MK (Basu et al., 2009). The intense pressure and temperature are strong enough to force the hydrogen atoms together, leading to the fusion of hydrogen atoms and generation of energy. Thus the core is a giant fusion reactor. The energy released as a consequence of this reaction is what makes the Sun the life-giving force for the Earth.

1.2.2 Radiative zone

The radiative zone is the next layer in the solar interior as one moves radially outwards. The energy generated in the core is transported towards the exterior by the processes of radiative diffusion and thermal conduction. The photons' mean free path in this region is so small, it can take as much as 170,000 years for a photon to reach up to the solar surface. The radiative zone extends to about 70% of the solar radius (Cox et al., 1991).

1.2.3 Tachocline

The tachocline is the region that marks the transition from the radiative zone into the Convection zone. It is thought to be quite thin, with a width of only 200-300 km (0.04% of $R_\odot$) (Stix, 2004). This layer is at the heart of the debate in the solar dynamo community and by extension stellar (Sun-like stars) community. There have

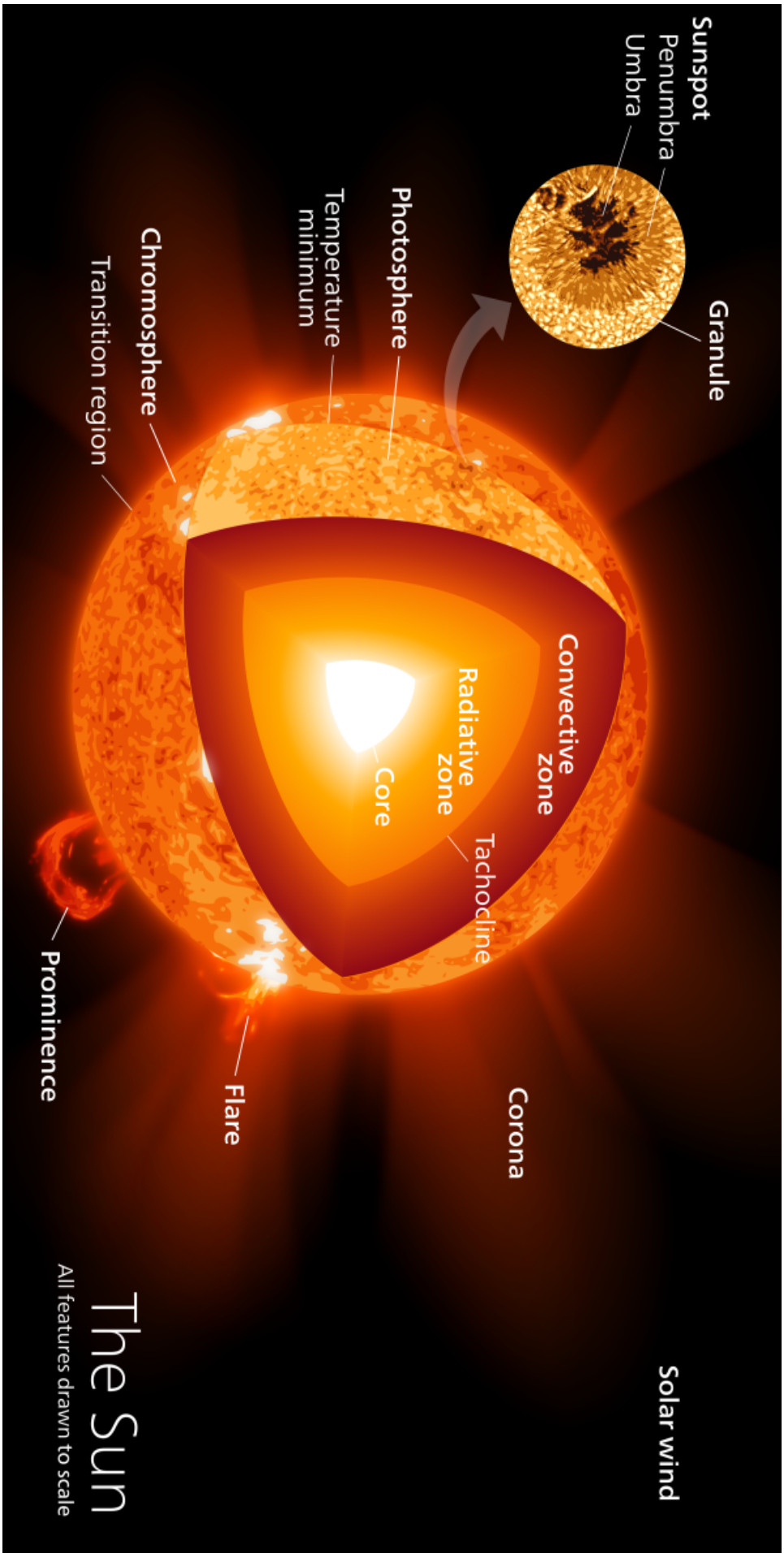

Fig. 1.3 A schematic representation various layers both interior and exterior layers of the Sun. Image credits: Kelvinsong (2015).

been several studies looking into the possibilities of the origin of the magnetic field within this layer due to a dynamo process (Ossendrijver, 2003; Soward et al., 2005).

1.2.4 Convection zone

Beyond the tachocline, temperature and pressure continue to drop. The ions now can recombine with electrons as the temperature decreases leading to increased opacity and the photons are absorbed by the atoms. This creates a temperature gradient between the tachocline and the Sun's surface, and convection starts taking place. This layer has the characteristic properties of convection such as thermal columns are formed, carrying plasma to the surface and as it gets cooled, the cool dense plasma falls due to gravity (Eddington, 1942). This convection process is theorised to be responsible for causing gravity waves in the solar interior (Schou et al., 1998), although detection of these waves has eluded us so far. The solar granulation pattern is a pronounced effect of convection, it can be seen in the continuum images of the photosphere of the Sun.

1.3 Solar atmosphere

The solar atmosphere is significantly different from the terrestrial atmosphere we encounter every day on Earth albeit with a few similarities. The similarity ends at both of the atmospheres being multi-layered. These two atmospheres have vastly different characteristics and scales. The top of the convection zone demarcates the interior from the atmosphere, reaching up to the very first layer of the solar atmosphere, called the photosphere. The photosphere and other layers become visible as the optical depth becomes $\lesssim 1$ at the top of the convection layer. Optical depth is defined as the fraction of photons that can pass through a layer without being scattered within that layer. For a value of $\lesssim 1$, this means that approximately a third of all photons will pass through this layer unhindered (Heintze et al., 1964; Rouse, 1966). There are three layers of the solar atmosphere: the chromosphere, the transition region and the corona (see Figure 1.3). Then the solar atmosphere transitions into the solar wind which fills the interplanetary medium. One of the popular semi-empirical models of the lower solar atmosphere is called the "VALIIIc". The model is illustrated in Figure 1.4 (Vernazza et al., 1981). The density and temperature are represented in blue and red, respectively. The full model offers a range of additional parameters such as number density, total pressure and optical depth all as a function of height in the atmosphere.

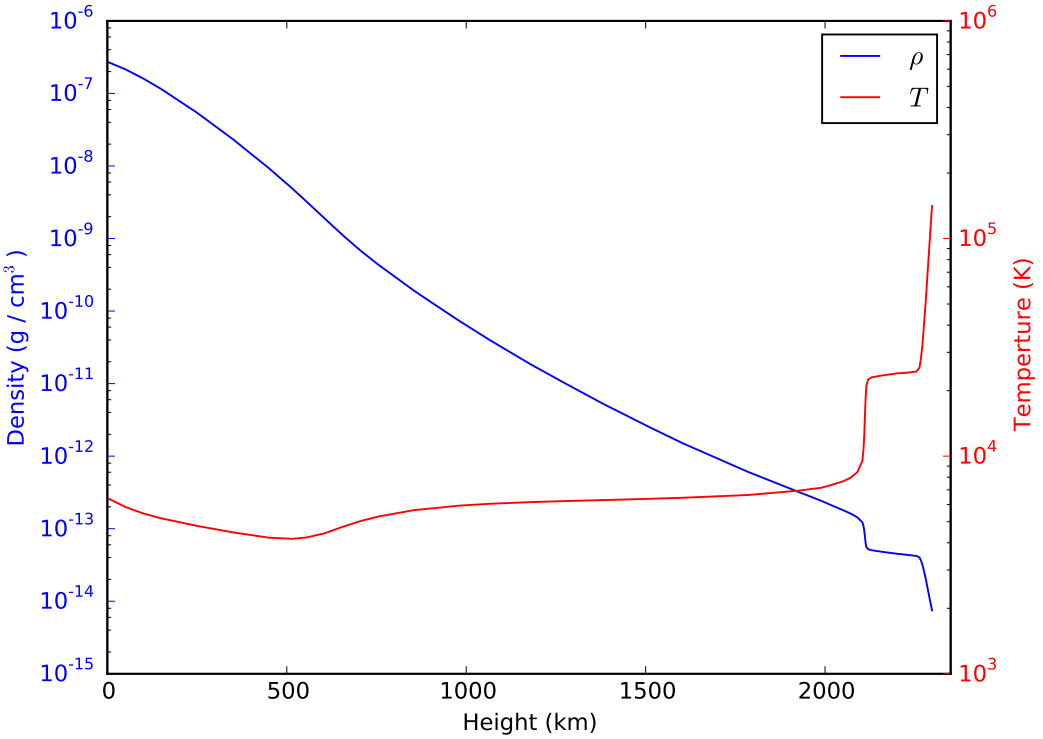

Fig. 1.4 The VALIIIc (Vernazza et al., 1981) model of the quiet Sun. The density and temperature are shown in *blue* and *red* respectively. The temperature minimum region and the transition region can be observed with these two parameters.

1.3.1 Photosphere

From the top of the convection zone, the temperature and density drop to 5700 K and 0.0002 kg m^{-3} respectively (Page & Hirsch, 2000). This leads to the first visible layer of the Sun called the photosphere. The word photosphere comes from the ancient Greek word 'photos' meaning 'light'. The photosphere has an approximate thickness of 500 km. The photosphere starts with a temperature of 5700 K which drops as you move away from the surface, reaching approximately 4500 K. The photosphere has a granular pattern resulting from the ascending warmer gas in the centres of the granules and descending cooler gas in the intergranular lanes separating them. These are short-lived, with a lifetime less than 10 minutes, resulting in a repeating pattern at small-scales (Rutten & Severino, 2012), they are on average 1 Mm in diameter as seen in Fig 1.5. The Fig 1.5 is a testament of how far we have come in our imaging capabilities. These granules are clearly visible in Figure 1.5, this is the most detailed image of any star that humankind has ever taken. On larger scales, the photosphere is dominated by a cell-like flow pattern with diameters of 30 Mm, called supergranulation, which can last for a day or longer (Rieutord & Rincon, 2010).

The convective nature of the Sun offers us the possibility to use techniques similar to seismological investigations of our own planet, to probe its interior. The turbulence

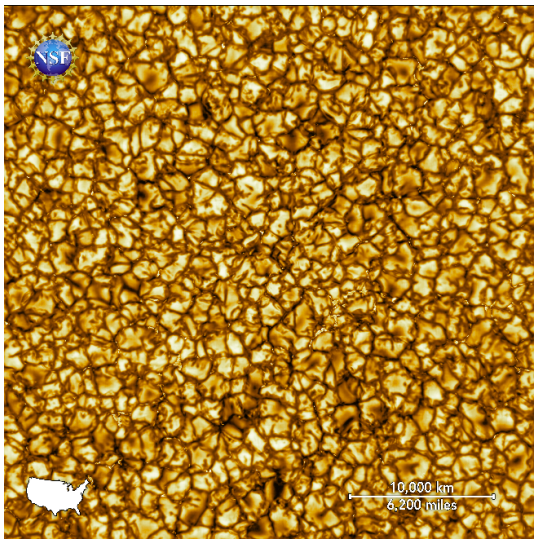

Fig. 1.5 The Daniel K. Inouye Solar Telescope(DKIST) has produced the highest resolution image of the Sun's surface ever taken. In this picture taken at 789 nm, features as small as 30 km can be seen, for the first time ever. The image shows a pattern of turbulent, "boiling" gas that covers the entire Sun. The cell-like structures – each about the size of Texas – are the signature of violent motions that transport heat from the inside of the Sun to its surface. Hot solar material (plasma) rises in the bright centres of "cells", cools off and then sinks below the surface in dark lanes in a process known as convection. In these dark lanes, one can also see the tiny, bright markers of magnetic fields. These bright specks are thought to channel energy up into the outer layers of the solar atmosphere called the corona. Image credits: NSO.

within the convection zone creates an entire spectrum of acoustic waves, named *p*-modes, where *p* stands for pressure, which can be exploited with helioseismology techniques. These acoustic waves penetrate into the solar interior and at certain frequencies, they form standing waves. The line-of-sight (LOS) Doppler images of the photosphere give an indication of these standing modes. These wave modes' overall properties are affected by the physical conditions where the maximum amplitude for that mode occurs. This allows us to be able to build an image at varied depths within the solar interior. Fourier transforms discussed in Chapter 2 are of great use in carrying out these studies. For reviews on this topic, see Deubner & Gough (1984) and Christensen-Dalsgaard (2002). The photosphere is quite a dynamic layer. The dynamics of which are determined by two processes, 1) convection as discussed above, and 2) the solar magnetic field, which is discussed in Section 1.4.

1.3.2 Chromosphere

The next layer is visible to the naked (human) eye only during a total solar eclipse. It is seen as an intense red region which was given the name, the chromosphere, from the Greek word 'chroma', meaning colour. This layer is visible during the total solar eclipse as a 'pink' coloured layer (Frankland & Lockyer, 1869). The density

of the chromosphere is just 10^{-4} times that of the photosphere. It is roughly 2 Mm thick and is a highly complex layer and dynamic in nature. The temperature of the chromosphere increases with height and reaches around 20,000 K at the boundary where it meets the next layer, the transition region. To observe the chromosphere from Earth, it is common to use either a Hα filter or a Ca II filter. The very large range of structures and the inhomogeneity of the chromosphere are best revealed when it is observed at different wavelengths, from the EUV to the radio domain. The chromosphere is host to many small-scale structures, e.g. spicules, that have been discovered due to the increasing resolution of solar telescopes over the past few decades. Some of the structures in the chromosphere (see Figure 1.6) are **(a)** plages (seen in EUV emission lines, or at longer wavelengths [Mg I h and k, or Ca II-H and K], **(b)** Sunspots (lower chromosphere, seen in EUV He II), **(c)** spicules and surges (best seen in Hα line) along with prominent fibrils and grains. This layer has been under rigorous investigations, for an overview see Narain & Ulmschneider (1990, 1996); Sterling (2000); Rutten (2007, 2012); Jess et al. (2015).

1.3.3 Transition region

Above the chromosphere, is a thin ($\approx$ 100 km) layer where the temperature rises rapidly from 20,000 K to 1,000,000 K. This is called the transition region (TR). This means that the TR is very non-uniform and Tian et al. (2009) suggests that the height varies depending on what magnetic features are below the TR. Lower transition region ($T < 5 \times 10^5$K) shows structures similar to the chromosphere, with network and plages. In the upper transition region structures are more similar to the corona. Most of the energy from the corona is thermally conducted down to the transition region where it is radiated away. Also, the brightness variability in the (quiet) transition region is larger than in any other layer of the solar atmosphere. This thin layer bridges a large difference in temperature. This layer also separates the dilute coronal plasma (with number densities of $n \leq 10^{12}\mathrm{m}^{-3}$) from the dense ($n \leq 10^{16}\mathrm{m}^{-3}$) chromosphere (Aschwanden, 2004, see chapter 1).

1.3.4 Corona

The next layer is the outermost atmosphere of the Sun, called the corona. The observations studied within this thesis are of this region (Chapter 3 and Chapter 4). Historically this was only visible during a total solar eclipse (see Figure 1.7). The corona largely emits in Extreme Ultra-Violet (EUV see Figure 1.8) and X-ray regions of the electromagnetic spectrum. These waves are absorbed by the Earth's atmosphere and thus studying the corona requires space-based observations. To study the corona from Earth, the much brighter solar disk needs to be occulted by

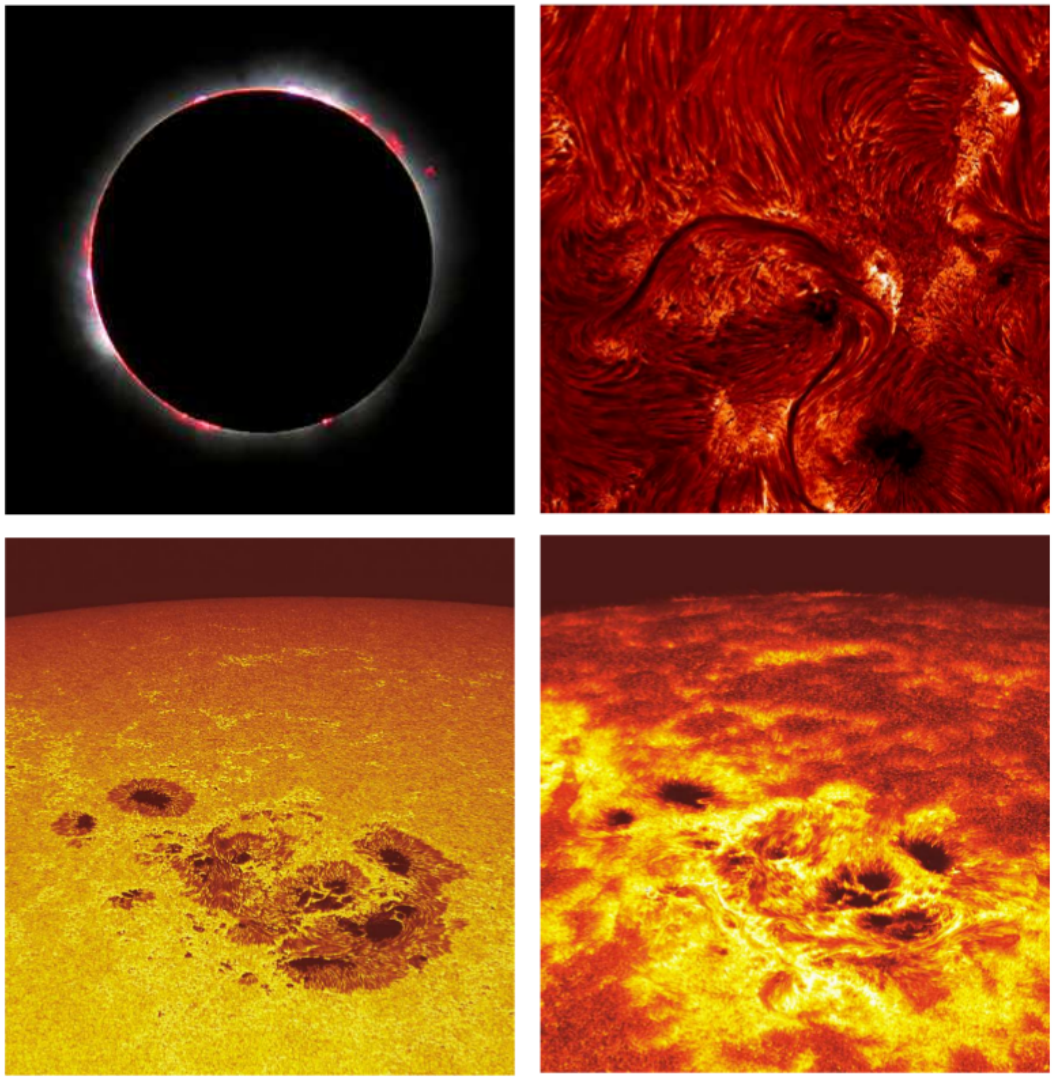

Fig. 1.6 *Top left:* Chromosphere seen during an eclipse. *Top right:* Chromosphere seen in Hα. *Bottom left:* Photospheric sunspots and bright points. *Bottom right:* Chromospheric view of *Bottom left:* (using Ca^{+}) (Ayres et al., 2009).

a device called a coronograph. A coronagraph is required for optical and infrared observations where brightness from the disk is too intense, i.e. the photosphere is a stronger emitter at these wavelengths than the corona. The solar corona extends many solar radii away from the solar surface and it is continuously expanding into the solar system, known as the solar wind. The average temperature of the corona is about 1-2 MK, however, it can reach temperatures as high as 8-10 MK, during strong flares (Aschwanden, 2004). The physical processes that account for the high temperature of the corona is an open problem still (one of the holy grails of solar physics). There are two main hypotheses in contention, hoping to provide a solution to the *coronal heating problem*. The first idea is based on magnetic reconnection. This process is where magnetic field changes its topology and the magnetic energy stored within the field is converted to kinetic and thermal energy. Thus the plasma that is present in these regions will become heated. The second idea involves the

Fig. 1.7 Corona during an eclipse (21-Aug-2017). The extent of corona and various structures such as streamers are visible. The pink structure is the visible chromosphere during eclipse. Image Credit & Copyright: Nicolas Lefaudeux.

magnetohydrodynamic (MHD) waves. The idea is that MHD waves can channel the energy through the various layers of the solar atmosphere into the solar corona. It requires that these MHD waves are able to dissipate their energy into the plasma in order to heat the plasma. However, this has yet to be directly observed. This thesis tries to further increase our understanding of these waves. Coronal heating has been thoroughly investigated for many decades and reviews by various authors exist Withbroe & Noyes (1977); Rosner et al. (1978); Erdélyi (2004); Klimchuk (2006); Parnell & De Moortel (2012); Sakurai (2017); De Moortel et al. (2020, e.g.).

The magnetic field in the corona can be broadly classified into two configurations. The field is either arranged in the form of closed loops of increased density (enhanced emission), or in the form of open field lines seemingly not connecting back to the solar surface (Wiegelmann et al., 2014). Arcades (ensembles) of bright coronal loops connect regions of opposite magnetic polarity on the solar surface and are mostly found to be rooted in an AR. Large-scale coronal loop systems can connect the neighbouring ARs and/or ARs with their quiet Sun surroundings. The observed coronal loop systems cover a wide range of length scales, from a few Mms up to giant arches reaching up to 1000 Mm. Several loop arcades neighbouring each other are often found in magnetically complex ARs and often host eruptive processes such as flares or CMEs. Therefore, in the majority of cases, bright coronal loops are concentrated around the regions of higher activity. Most of the quiet-Sun magnetic fields that reach the corona are rooted in the magnetic network (see Section 1.4.1). At

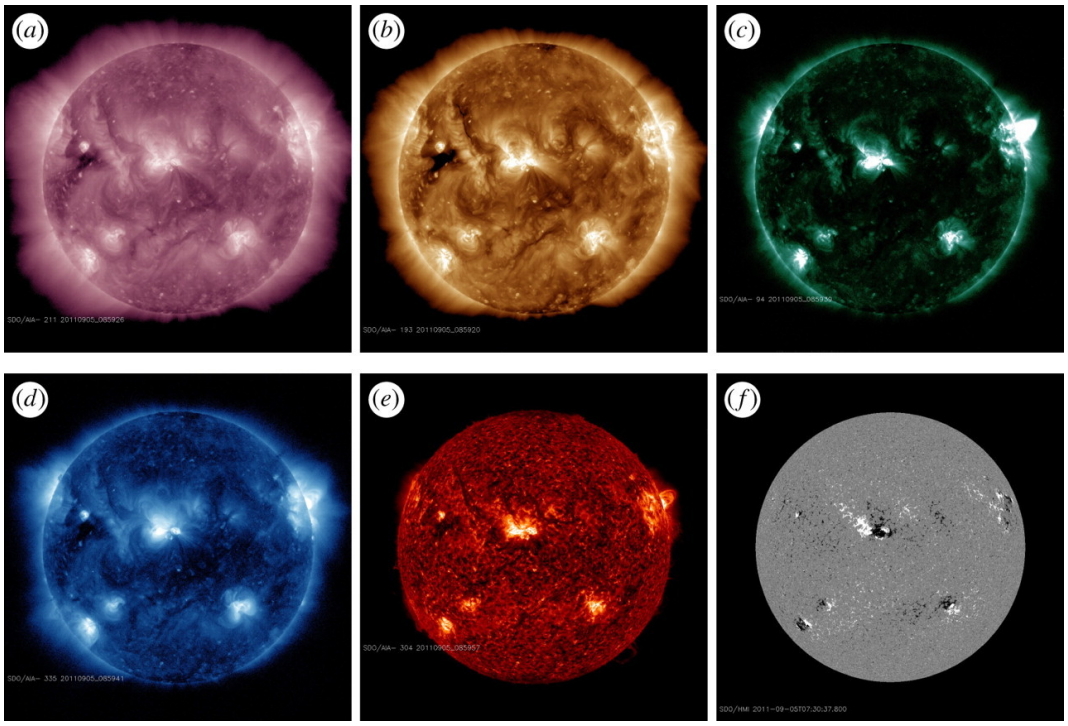

Fig. 1.8 (a-e) SDO/AIA 211 Å, 193 Å, 094 Å, 335 Å and 304 Å images of the solar corona and chromosphere showing the different structures including active regions and coronal holes. (f) SDO/HMI magnetogram of the magnetic field in the photosphere (27-Aug-2011) (taken from (Parnell & De Moortel, 2012)).

greater heights, they fan out to form funnels and to fill the coronal volume. Open field structures provide a highway for the plasma. The plasma is efficiently transported outwards along the open field lines, which allows the charged particles to escape from the solar atmosphere. Especially during minimum solar activity, open magnetic flux is concentrated around the poles, causing depleted regions which emit less than their surrounding temperatures above 1 MK and consequently appear dark in coronal images, and are called coronal holes. At lower latitudes, the coronal structure is dominated by "helmet streamers" and "pseudo streamers", extending out to several solar radii in height. For a review on coronal loops, a good resource is Reale (2010).

1.4 Magnetic field on the Sun

The solar magnetic field plays a key role in various solar phenomena and thus is imperative to understand the behaviour of solar magnetic fields. The most prevalent way to understand the magnetic field of stars is to use a method called the Zeeman effect (Phillips, 1995). The Zeeman effect can be described as a phenomenon of splitting of the spectral lines when placed in a magnetic field. Zeeman effect is dependent on the field strength and polarization. This effect can mostly be used in case of the photosphere, as only the photospheric magnetic field is strong enough to cause measurable splitting via the Zeeman effect. The images generated using the

Zeeman effect are called solar magnetograms. Magnetograms provide us with the basic magnetic field structure of the photosphere.

The magnetic field on photosphere is very weak ($\leq$ 40 Gauss) on average and is very sparse (Domínguez Cerdeña et al., 2006; Viticchié et al., 2011). This is a defining feature of the quiet Sun and is shown in Figure 1.5. The dominating feature within this image is the granulation cells, which are evidence of convection, as well as several small magnetic features. The flux emergence, as described in Section 1.4.3.1, dominates the photospheric magnetic fields, the largest of the Ω loops form the bipolar active regions. Coronal loops are a manifestation of the magnetic field, filled with heated plasma, shaped by the geometry of the coronal magnetic field, where cross-field diffusion is strongly inhibited (Ossendrijver, 2003; Jain et al., 2009). A schematic diagram representing the magnetic field structure in the atmosphere away from active regions is shown in Figure 1.9. The two different magnetic field configurations have different properties and lead to different consequences. The open-field regions connect the solar surface with the interplanetary field and are the source of the fast solar wind ($\sim$ 800 km s^{-1}) (Levine et al., 1977; Levine, 1977; Bohlin & Sheeley, 1978; Levine, 1978; Pneuman, 1980; Barnes, 1979). A consequence of the open-field configuration is efficient plasma transport out into the heliosphere, whenever chromospheric plasma is heated at the footpoints. On the other hand, closed-field regions (comprised of self-evident closed field lines) reaching altitudes of up to one solar radius. These closed-field regions contain all the bright and over-dense coronal loops, produced by filling with chromospheric plasma that stays trapped in these closed field lines (Reale, 2010).

1.4.1 Quiet Sun

Traditionally the "quiet-Sun" (QS) regions got their name because they were assumed to lack magnetic activity. However, while large-scale eruptions are mainly associated with ARs, the QS is found to be not so quiet after all. Dynamic processes that occur on smaller scales had simply not been resolved because of the technological limitations of earlier telescopes and instruments. The smallest resolved bipolar features on the solar surface are the internetwork magnetic loops emerging throughout the quiet Sun. Although ARs are regions of high magnetic flux, they constitute a significantly smaller proportion of the total magnetic flux on the surface, the majority of the magnetic flux on the solar surface is brought by the smaller scale magnetic structures that populate the photospheric surface. At photospheric levels, only a small fraction of the solar surface is occupied by a strong magnetic field. The fields take the form of kiloGauss fluxtubes, often seen as magnetic bright points in photospheric images. The bright points are swept out from the internetwork by the supergranular flows. The flux gathers at the boundaries of the super-granule flows, forming the

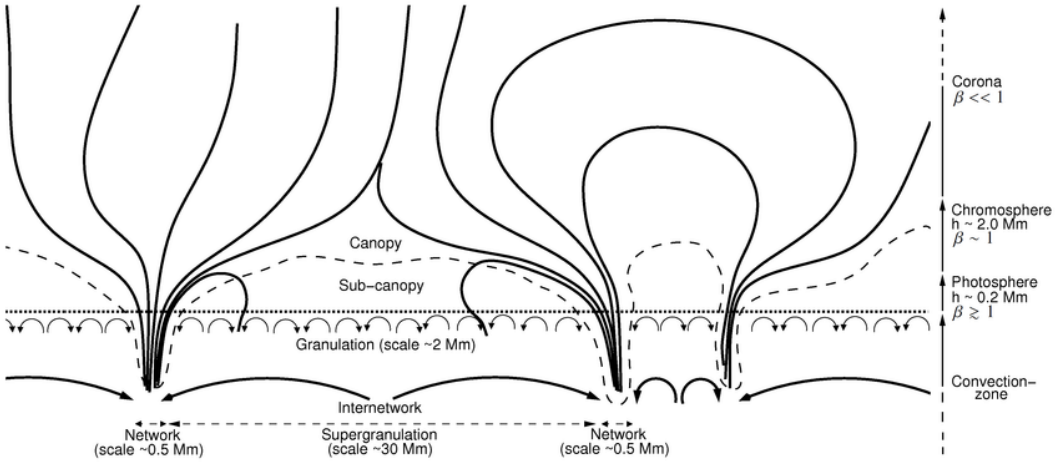

Fig. 1.9 Schematic representation of the quiet-Sun magnetic field structure in a vertical cross-section through the atmospheric layers of the Sun. Large-scale convective flows (thick, large arrows at the bottom) at the edges of the supergranular cells lead to the formation of intense magnetic network elements or sunspots. The small-scale convective flows (thin, small arrows below dotted horizontal line representing the photosphere) result in the photospheric granular pattern. The magnetic field lines (solid lines) expand at chromospheric heights and form the nearly horizontal magnetic canopy (dashed line) (Peter, 2001; Wiegelmann et al., 2014).

magnetic network. In contrast to that, the coronal magnetic field fills the entire volume of the corona, due to the density stratification along the solar atmosphere. It is distributed relatively uniformly in strength, not so much in the magnetic field orientation. Consequently, the photospheric field must spread out with increasing height in the solar atmosphere. The magnetic field expands until it either turns over and returns to connect back to the photosphere or it meets the expanding field of the neighbouring flux tubes. This forms the "magnetic canopy", transversing the various layers of solar atmosphere (see Figure 1.9).

The expansion of the magnetic field with height is a consequence of the small gas-pressure scale height ($\sim$100 km in non-magnetic regions). From the lateral pressure balance, it follows that the field strength must rapidly decrease with height. (The lateral pressure balance neccesitates the gas pressure inside to be lower than outside of the fluxtube.) As the height increases, the magnetic field strength decreases due to the falloff of the gas pressure and flux conservation imply that the magnetic field must spread out, i.e., the extension of the magnetic structures must increase rapidly. Since magnetic features are hotter than their surroundings in the middle/upper photosphere and chromosphere, the internal gas pressure drops more slowly with height than the external gas pressure. As a consequence, at certain heights, the internal pressure force exceeds the external. This removes the lateral confinement of the magnetic structures and allows the structures to expand unhindered until it hits the field from another photospheric source. This implies a significant horizontal component of the

field over a large part of the volume (see Figure 1.9 for magnetic canopy Solanki & Steiner, 1990; Bray et al., 1991)

1.4.2 Plasma-β

One of the important physical parameters in the study of plasma is the plasma-β. Plasma-β is defined as

$$\beta = \frac{plasma pressure}{magnetic pressure} = \frac{nk_BT}{\frac{B^2}{2\mu_0}}, \tag{1.1}$$

where μ_0 is the permeability in vacuum, and other symbols have the usual meaning. The solar atmosphere can also be classified based on the value of this β parameter (see Figure 1.10). In case of solar corona the plasma-$\beta << 1$ and thus the processes in the solar coorna are magnetically dominated, whereas in the Photosphere $\beta > 1$, and thus is hydrodynamically dominated. for a detailed review on the magnetic field and the plasma-β behaviors a good review paper is Wiegelmann et al. (2014).

1.4.3 Active Sun and the Solar Cycle

The active sun magnetic field is dominated by the large scale, concentrated magnetic flux such as in the active regions (see Section 1.4.3.1) or the sunspots (see Section 1.4.3.2). One of the defining features of the active sun is the solar cycle. The solar cycle is on average an 11-year variation in the activity of the Sun. This cycle manifests itself as a variation in the number of sunspots, the amount of solar irradiance and the levels of other solar activity (Burroughs, 2007). A full magnetic cycle, however, takes 22 years, which includes the reversal of magnetic polarity of the Sun. Each cycle has a solar maximum and a solar minimum. A solar maximum and a solar minimum refer to periods of maximum and minimum sunspot counts, respectively and cycles span from one minimum to the next. As of May 2020, we are heading towards the end of the solar cycle 24 and the solar cycle 25 is thought to be just around the corner (Petrovay, 2020; Bhowmik & Nandy, 2020; Nandy et al., 2020). *Nomen est omen*, there is a considerably large amount of magnetic activity towards the solar maximum, while this is significantly reduced in a solar minimum. However, it must be noted that solar activity being at a minima does not mean the Sun is no longer dynamic. Each solar cycle can be characterised by the magnetic activity, one of the most common and longest observations as a proxy for magnetic activity are the sunspots (see Subsection 1.4.3.2). This has been recorded not much after the invention of the telescope and the discovery of 'spots on the Sun'. These continuous observations date as far back as the 17^{th} century. These observations are called the sunspot number catalogue. Figure 1.11 displays this catalogue with

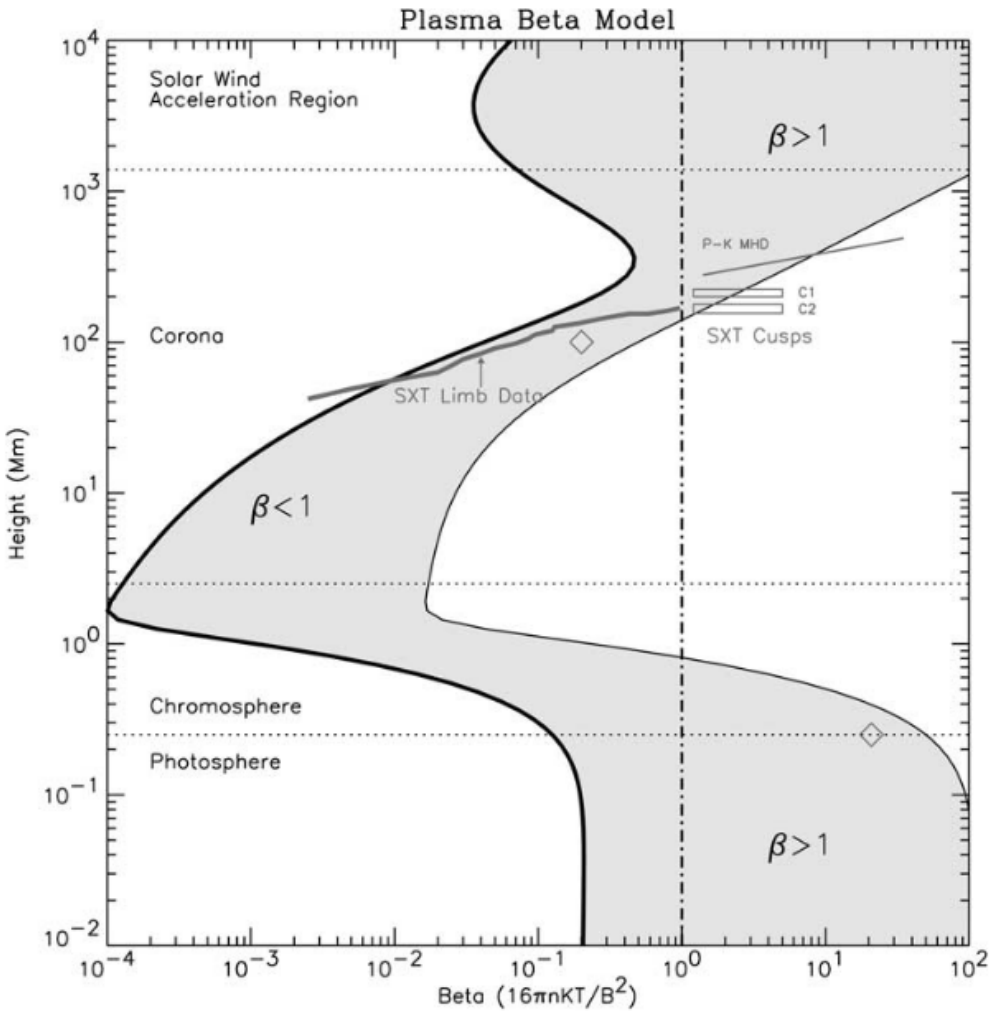

Fig. 1.10 A model of plasma-β at different altitudes in the solar atmosphere (Gary, 2001).

the raw count as the blue line and a running average in red. The main conclusion is that each cycle has a different duration and will produce a differing amount of sunspots. Since each solar cycle differs in its characteristics, strength (number of sunspots), there is also a significant variation in the number of "extreme/explosive" events, namely flares and coronal mass ejections (CMEs).

The solar cycle can even directly impact the Earth's climate, as evidenced by the long period minimas, such as Maunder and Dalton minima. The Maunder minima was an abnormally low amount of sunspots during the late seventeenth century and were the prime suspect for the Little Ice Age (Eddy, 1976; Friis-Christensen & Lassen, 1991; Burroughs, 2007) in Europe. There have been studies indicating that the solar cycle might influence the relationship between the atmospheric oscillations affecting the temperatures in the northern hemisphere (Gimeno et al., 2003; de La Torre et al., 2007; Lockwood et al., 2010).

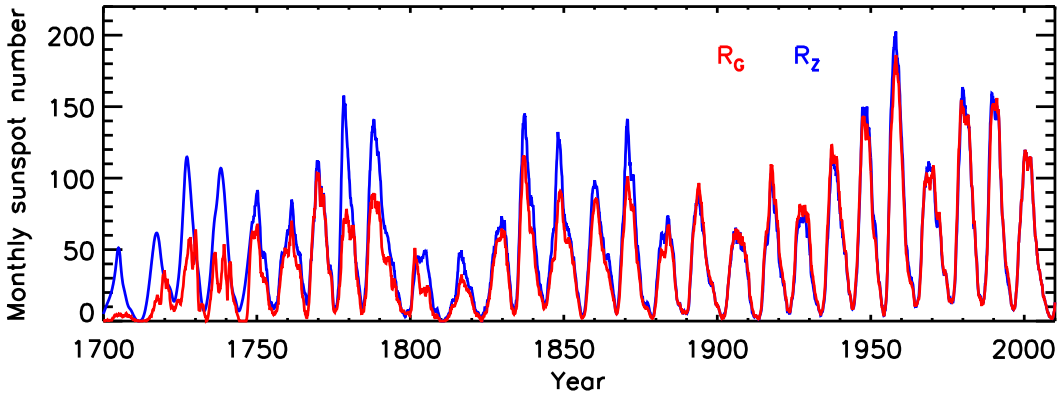

Fig. 1.11 The sunspot number record as it currently stands since continuous observations of the Sun began. The blue line is the 12 month running average of the Wolf sunspot number and the red line is the group sunspot number. The eleven year solar cycle is visible within both datasets (Jiang et al., 2011).

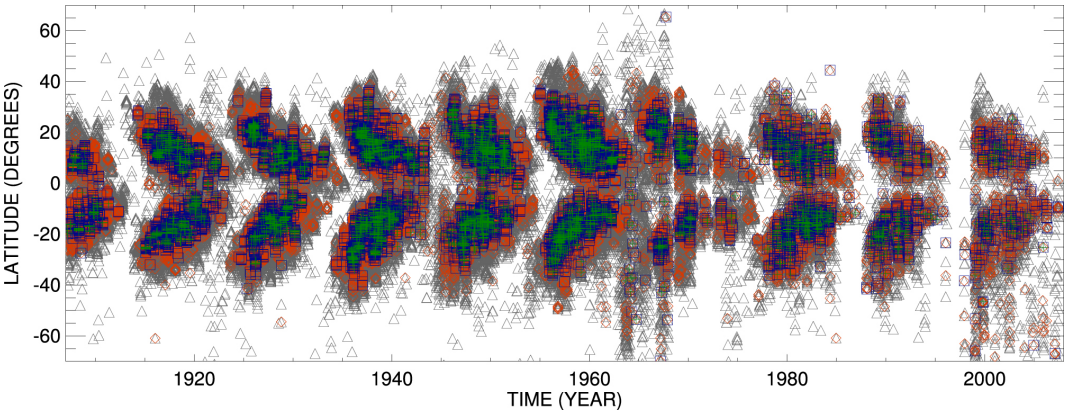

Fig. 1.12 Ca II K butterfly diagram. Grey triangles depict centroids of plages with area $\geqslant 1\,\text{arcmin}^2$. The red, blue, and green symbols depict the centroids of plages with area $\geqslant 4\,\text{arcmin}^2$, $\geqslant 7\,\text{arcmin}^2$, and $\geqslant 10\,\text{arcmin}^2$ respectively. Obtained from the long term archaic images obtained from Kodaikanal Observatory. (Chatterjee et al., 2016)

1.4.3.1 Active regions

One of the most recognisable features on the solar disk are the Active Regions (ARs). They also form a significant part of the properties of the photospheric magnetic features. These are areas of large magnetic field concentrations visible on the solar surface. They are important for the study of solar activity and space weather and hence have been catalogued regularly by various observatories and organisations. The most noticeable features in the ARs are sunspots (see Subsection 1.4.3.2) and pores. They vary in scale, lifetime and what magnetic structures are found.

ARs generally form within a latitude band of $\pm 30^\circ$ of the equator. These are generated from a large flux bundle that is formed deep in the convective zone that rises as a Ω-shaped loop that breaks through the photosphere (Meyer et al., 1974; Solanki, 2003a; Toriumi et al., 2014). The flux bundle rises through the convective

zone because of magnetic buoyancy. A schematic diagram of how magnetic flux is transported from the convective zone to the photosphere in order to form ARs is shown in Figure 1.13. The process can be classified into two distinct processes: 1) the solar dynamo to create the magnetic field and 2) formation and transport of the flux bundle on the solar surface. Active region formation takes up to a few days and a cluster of sunspots in an AR are surrounded by regions of enhanced brightness in the photosphere. Sunspots will keep forming as long as magnetic flux emerges but most sunspots decay before a single rotation. Sunspots have been found to be moving faster than the surrounding local plasma, implying that they are anchored below the surface where the rotation rate is faster (Engvold et al., 2019). Figure 1.14 shows a complex AR that was observed with the Solar Dynamics Observatory's (SDO) Helioseismic and Magnetic Imager (HMI) instrument. The top image is a white light view of the AR while the bottom image is a LOS magnetogram where blue represents positive polarity and red represents negative polarity. It has been found that the more complex the magnetic geometry is the more active the region is (source of large flares/eruptions).

ARs are the regions that play a dominant role in the dynamic behaviour of the Sun. Almost all of the solar activity originates in these regions. Most of the flares or coronal mass ejections originate from ARs since they contain large amounts of stored magnetic energy. These seemingly distant events have impacts that are felt even in our terrestrial environment, from creating spectacular auroras near the poles or in certain situations the disruption of radio transmissions, damage to satellites and electrical transmission lines.

1.4.3.2 Sunspots

Sunspots appear as dark areas on the otherwise bright Sun's surface. A sunspot is formed as a result of the internal magnetic field bursting through the visible surface and out into the corona (Romanchuk, 1963; Meyer et al., 1974). Sunspots appear dark because the magnetic fields suppress the convective process, which in turn results in a suppression of energy and heat transport to the surface. Because these areas are heated less, they can be a few thousands of degrees Kelvin cooler than the surrounding photosphere (10, 000K), making them appear dark in comparison to the rest of the surface.

The first known record of the sunspot is found in a chronicle by John of Worcester in 1128 as seen in Figure 1.2. The advantage the Sun provides is being the closest star to study, however, it was not until the invention of the telescope that sunspots were studied in detail. Early observations of sunspots were able to identify the two regions of sunspots namely, umbra and penumbra and that sunspots always appear near the solar equator. Sunspots were still an enigma in the nineteenth century.

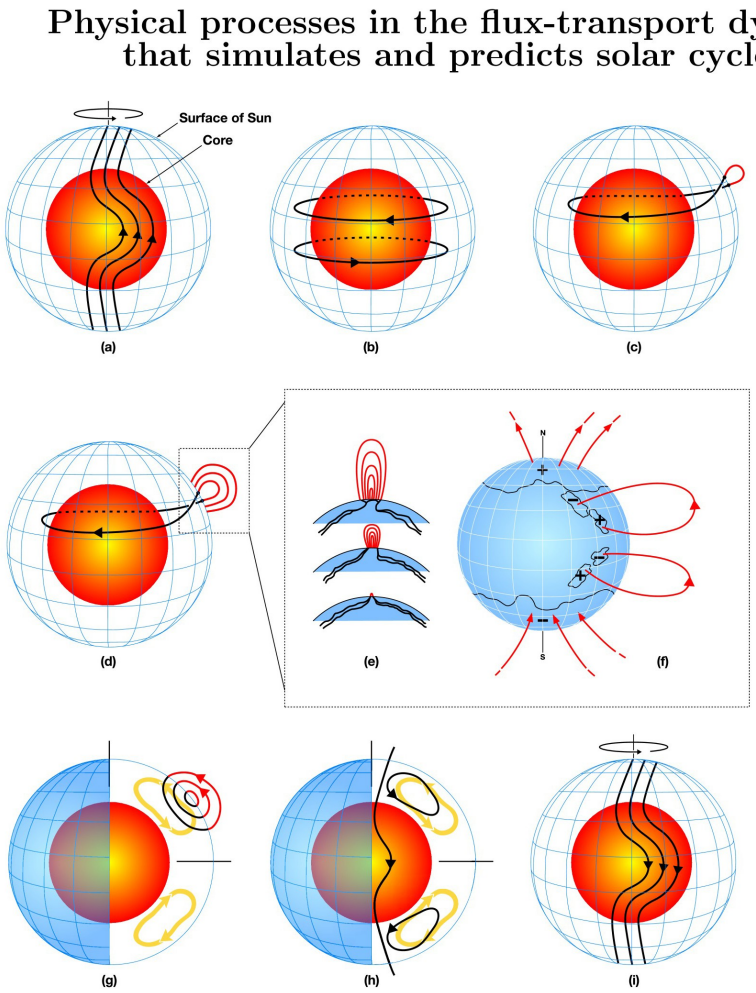

Fig. 1.13 Schematic diagram of magnetic flux emergence. The red sphere represents the Sun's inner radiative zone and the blue mesh the photosphere. The solar dynamo is located between these two layers (a) The shearing of the magnetic field due to Sun's differential rotation. (b) Formation of the toroidal magnetic field as a consequence of differential rotation. (c) Magnetically buoyant loops rise to the surface when the magnetic field is strong enough and twist as they arise due to differential rotation. sunspots are formed from these loops. (d,e) More magnetic flux emerges. (f) Magnetic flux spreads in latitude and longitude from decaying sunspots. (g) Meridional flows (yellow circulation) carries surface magnetic flux towards the poles, polar fields get reversed. (h) Flux gets transported downwards towards the equator, changing the orientation of the poloidal field from an initial configuration (a). (i) Reversed poloidal field sheared again and the cycle continues. Reproduced from Dikpati & Gilman (2007) and is available online from http://www.arrl.org/w1aw-bulletins-archive/ARLP018/2013.

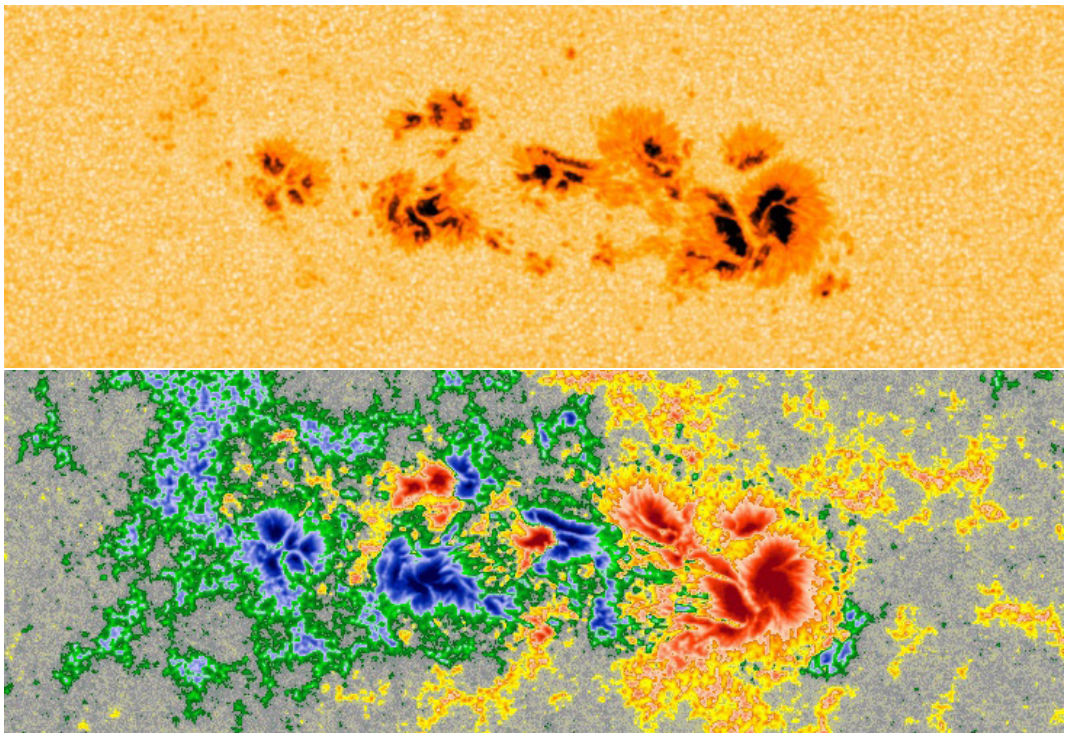

Fig. 1.14 A complex AR seen by Solar Dynamics Observatory's (SDO) Helioseismic and Magnetic Imager (HMI) instrument. The top image is a white light image of the AR. The bottom image displays the line-of-sight (LOS) magnetic field of this AR, where blue indicates positive polarity and red indicates negative polarity. Source: https://www.spaceweatherlive.com/en/help/the-magnetic-classification-of-sunspots.

Alexander Wilson also noticed that the penumbra that is farthest from the limb is narrower which led him to deduce that sunspots are on the surface of a moving sphere (Loughhead & Bray, 1958). He also discovered that a sunspot is a saucer-like depression (500-700 km) in the visible surface and this was named the Wilson effect. This effect is a result of umbra being more optically transparent. Thus light from the umbra comes from a deeper level than the photosphere itself (Priest, 2014). Many astronomers thought that sunspots were 'holes' in the photosphere, but because the Sun was presumably hotter beneath the photosphere, the sunspots should appear bright rather than dark. Then in 1872, Angelo Secchi suggested that matter was ejected from the surface of the Sun at the edges of a sunspot. This matter then cooled and fell back into the centre of the spot, so producing its dark central region. In 1843, Heinrich Schwabe found that the number of sunspots varied with a period of about 10 years (Schwabe, 1844). A little later Rudolf Wolf analyzed historical records that showed periods ranging from 7 to 17 years, with an average of 11.1 years (Wolf, 1859). Then in 1852, Sabine, Wolf, and Gautier independently concluded that there was a correlation between sunspots and disturbances in the Earth's magnetic field. There were also various unsuccessful attempts to link the sunspot cycle to the Earth's weather. But toward the end of the century, Walter Maunder pointed out that there

had been a lack of sunspots between about 1645 and 1715. He suggested that this period, now called the Maunder Minimum, could have had a more profound effect on the Earth's weather than the 11-year solar cycle. In 1858, Richard Carrington discovered that the latitude of sunspots changed over the solar cycle (Carrington, 1858). In the following year, he found that sunspots near the solar equator moved faster than those at higher latitudes, showing that the Sun did not rotate as a rigid body. This so-called differential rotation of the Sun was interpreted by Secchi as indicating that the Sun was gaseous. In the same year, Carrington and Hodgson independently observed two white light solar flares moving over the surface of a large sunspot. About 36 hours later, this was followed by a major geomagnetic storm (McFadden et al., 2007).

Sunspots form the heart of an active region. Sunspots and sunspot groups are classified according to their morphology. The brightness and thus the temperature of a sunspot is a function of spatial position within the spot. The sunspot can be classified into two regions the darker umbra and relatively brighter penumbra. The umbra is 1000-1900 K cooler than the quiet Sun, the penumbra is 250-400 K cooler. The magnetic field strength in the photosphere is approximately 1000-1500 G averaged over a sunspot. The magnetic field varies gradually from 1800-3700 G in the darkest part of the umbra to 700-1000 G at the outermost part of the penumbra. The field strength also decreases with altitude in the atmosphere. At the same time, the field fans out very rapidly. Sunspots are reviewed in Solanki (2003b); Borrero & Ichimoto (2011), and for a review of the historical sunspot observations refer to Arlt & Vaquero (2020).

1.5 Magnetohydrodynamics (MHD)

MHD is a framework that combines the fluid motions with Maxwell's equations to describe the physics of plasma (an electrically charged neutral fluid). It is one of the primary mathematical frameworks used to describe the dynamics of plasma in general and solar plasma in particular.

The displacement current is neglected in the Ampére's law, which gives,

$$\nabla \times \vec{B} = \mu_0 \vec{j}, \tag{1.2}$$

where $\vec{B}$, μ_0, and j are the magnetic field vector, magnetic permeability, and current density vector, respectively. Charge neutrality is also assumed, which implies that an electric field can only be induced by a changing $\vec{B}$ field and $\nabla \cdot \vec{E} = 0$, since excesses of charge are not allowed to accumulate.

Faraday's law dictates this induced electric field behaves as follows,

$$\frac{\partial \vec{B}}{\partial t} = -\nabla \times \vec{E}. \tag{1.3}$$

Currents are generated in the plasma by a non-zero $\vec{E}$ or a changing $\vec{B}$ and are determined by the generalized Ohm's law,

$$\vec{j} = \sigma(\vec{E} + \vec{v} \times \vec{B}), \tag{1.4}$$

where σ and $\vec{v}$ are the electrical conductivity and plasma velocity, respectively. Solving for $\vec{E}$ in Equation 1.4 and substituting it in Equation 1.3, results in,

$$\frac{\partial \vec{B}}{\partial t} = -\nabla \times \left(\frac{\vec{j}}{\sigma} - \vec{v} \times \vec{B} \right). \tag{1.5}$$

Thus, currents can be defined in terms of $\vec{B}$ alone. Equation 1.2 can then be rearranged and substituted for $\vec{j}$,

$$\frac{\partial \vec{B}}{\partial t} = \nabla \times (\vec{v} \times \vec{B}) - \nabla \times \left(\frac{\nabla \times \vec{B}}{\mu_0 \sigma} \right). \tag{1.6}$$

Using vector identities and $\nabla \cdot \vec{B} = 0$ and simplifying Equation 1.6 gives us the "induction equation".

$$\frac{\partial \vec{B}}{\partial t} = \nabla \times (\vec{v} \times \vec{B}) + \eta \nabla^2 \vec{B}, \tag{1.7}$$

where, σ is constant and magnetic diffusivity (η), is defined by $\eta \equiv 1/\mu_0 \sigma$. The induction equation is of serious consequence in the dynamics of the magnetic field in the plasma.

The first term on the right-hand side is the advective term which describes magnetic field dynamics due to plasma flows, and the second is the diffusive term which describes diffusion of the field due to gradients in the magnetic field itself. The advective timescale (Equation 1.8) is often much shorter than the diffusive timescales (Equation 1.9), so movement of the plasma via the plasma velocity tend to dominate the magnetic field dynamics. By dimensional analysis of Equation 1.7, characteristic timescales may be derived,

$$\frac{\Delta B}{\Delta t} = \frac{vB}{\Delta l} \Rightarrow \tau_{adv} = \Delta l \Delta B v B, \tag{1.8}$$

$$\frac{\Delta \vec{B}}{\Delta t} = \eta \frac{\vec{B}}{\Delta l^2} \Rightarrow \tau_{diff} = \frac{\Delta l^2 \Delta \vec{B}}{\eta \vec{B}}, \tag{1.9}$$

where Δl is a characteristic length scale, Δt is the characteristic time scale, ΔB is the difference in magnetic field between the start and end of the time-scale which is roughly equivalent to the characteristic field, B, τ_{adv} is the advection time scale and τ_{diff} is the diffusion time scale. For typical values in the solar corona with $\Delta l \sim 10^9$ m, $\Delta B \sim 1$ G, $\eta \sim 10^4$ m^{2}s^{-1}, $V \sim 10^3$ms^{-1}, the typical advection and diffusion timescales are 10^5 s and 10^13 s, respectively.

If the conductivity (σ) is assumed to be infinite, the equations give rise to ideal MHD. In ideal MHD, Equation 1.7 becomes,

$$\frac{\partial \vec{B}}{\partial t} = \nabla \times (\vec{v} \times \vec{B}) \tag{1.10}$$

The ratio of the diffusive and advective terms in the induction equation yield the magnetic Reynolds number,

$$R_m = \frac{V \Delta l}{\eta}, \tag{1.11}$$

where V is a characteristic fluid speed and Δl is a characteristic length scale. This number indicates the relative importance of fluid motions (advection) to magnetic diffusion in the evolution of the magnetic field. In most cases for the Sun $R_m >> 1$, (taking the values for the two timescales we get the $R_m \sim 10^8$) so the magnetic diffusion term in Equation 1.7 can be neglected. There are a few cases where this is far from true, such as in flares or in any reconnection process. This approximation of infinite conductivity is valid for astrophysical plasmas due to the large spatial scales that we deal with. In this ideal MHD plasma with $R_m >> 1$ Alfvén's frozen-flux theorem holds. This implies (a) magnetic flux is conserved; (b) magnetic field lines are conserved or in other words magnetic field lines are permanently embedded in the plasma they inhabit. Thus the field is advected with plasma motions or equivalently plasma is constrained to flow along field lines.

1.5.1 MHD equations

The complete set of ideal MHD equations are given as follows:

$$\frac{\partial \rho}{\partial t} + \nabla \cdot (\rho \vec{v}) = 0, \qquad \text{(Mass Conservation)}$$

$$\rho \frac{D\vec{v}}{Dt} = -\nabla p + \frac{1}{\mu_0}(\nabla \times \vec{B}) \times \vec{B} + \rho g, \qquad \text{(Equation of Motion)}$$

$$\frac{D}{Dt}\left(\frac{p}{\rho^\gamma}\right) = 0, \qquad \text{(Energy Equation)}$$

$$\frac{\partial \vec{B}}{\partial t} = \nabla \times (\vec{v} \times \vec{B}), \qquad \text{(Induction Equation)}$$

subject to,

$$\nabla \cdot \vec{B} = 0, \qquad \text{(Solenoid Equation)}$$
$$p = k_B \frac{\rho}{m} T, \qquad \text{(Ideal Gas Law)}$$
$$\vec{E} = -\vec{v} \times \vec{B}, \qquad \text{(Ohm's Law)}$$
$$\vec{j} = \nabla \times \vec{B}/\mu. \qquad \text{(Electric Current)}$$

Here ρ is the density, $\vec{v}$ is the velocity, $\frac{D}{Dt}$ is the convective derivative $\left(\frac{\partial}{\partial t} + (\vec{v} \cdot \nabla)\right)$, p is the pressure, γ is the ratio of specific heats ($5/3$ for an ideal mono-atomic gas), k_B is Boltzmann's constant, m is the mass of the gas, T is the temperature, and μ_0 is the magnetic permeability in vacuum.

These constitute eight partial differential equations for eight variables. Both $\vec{v}$ and $\vec{B}$ have three components each and there is also the density and temperature.

The energy density of a magnetic field is given by,

$$u_B = \frac{B^2}{2\mu_0}. \tag{1.12}$$

The total magnetic energy in a region of space is given by integrating over volume,

$$U_B = \int_V \frac{B^2}{2\mu_0} dV. \tag{1.13}$$

Considering the time evolution of the total energy and using a dot-product identity,

$$\frac{dU_B}{dt} = \frac{1}{2\mu_0} \int_V \frac{d}{dt}(\vec{B} \cdot \vec{B})\, dV. \tag{1.14}$$

Using the product rule,

$$\frac{dU_B}{dt} = \frac{1}{2\mu_0} \int_V \vec{B} \cdot \frac{d\vec{B}}{dt} + \frac{d\vec{B}}{dt} \cdot \vec{B}\, dV = \frac{1}{\mu_0} \int_V \vec{B} \cdot \frac{d\vec{B}}{dt} dV. \tag{1.15}$$

Equation 1.6 is then substituted for $d\vec{B}/dt$,

$$\frac{dU_B}{dt} = \frac{1}{\mu_0} \int_V \vec{B} \cdot (\vec{\nabla} \times (\vec{v} \times \vec{B}) - \vec{\nabla} \times (\eta \vec{\nabla} \times \vec{B}))\, dV. \tag{1.16}$$

The following equation can be derived from this by using a vector identity and substituting for current density,

$$\frac{dU_B}{dt} = -\int \frac{j^2}{\sigma} dV - \int \vec{v} \cdot (\vec{j} \times \vec{B})\, dV. \tag{1.17}$$

The first term on the right-hand-side represents energy lost through the dissipation of currents. This is also known as ohmic or Joule heating. The second term on the right-hand-side represents energy lost through work done on the plasma by the Lorentz force.

In addition to separating magnetic energy losses into components, the same can be done with magnetic forces. By combining Equation 1.2 and the Lorentz force in (Equation of Motion),

$$\vec{F_L} = \frac{(\nabla \times \vec{B}) \times \vec{B}}{\mu_0}. \tag{1.18}$$

is obtained. The force can then be split into two components using vector identities,

$$\vec{F_L} = \underbrace{-\nabla \frac{B^2}{2\mu_0}}_{\text{magnetic pressure}} + \underbrace{\frac{1}{\mu_0}(\vec{B} \cdot \nabla)\vec{B}}_{\text{tension}}. \tag{1.19}$$

The Lorentz force is perpendicular to the field: the magnetic pressure has a component along the field that cancels out the component of the magnetic tension that is along the field. Magnetic pressure[1], and a component acting along the field, magnetic tension. These forces can conveniently be attributed to many dynamic phenomena independently. Magnetic pressure is attributed to the apparent expansion of coronal loops as they reach higher into the atmosphere, while tension explains the restoring force that allows a coronal loop to spring back into place after it is disturbed by an external force.

Another quantity of importance is the plasma -β, it is the ratio of gas pressure to magnetic pressure,

$$\beta = \frac{P_G}{P_B} = \frac{n_e k_B T_e}{B^2/2\mu_0}. \tag{1.20}$$

In the solar interior, $\beta >> 1$ and magnetic fields' dynamics are dominated by plasma motions, while in the corona $\beta << 1$ and magnetic fields determine plasma motion. The change in plasma β above an active region is shown in Figure 1.10.

1.6 MHD waves

Magnetic tension, magnetic pressure and gas pressure are restoring forces that allow oscillations to take place along magnetic field lines in plasma. There are several types of waves that may result from these. To understand the behaviour of these waves, the case of small perturbations for the MHD quantities should be considered,

[1] The magnetic pressure, $B^2/2\mu_0$ is numerically equivalent to the magnetic energy density.

i.e.,

$$\begin{aligned}\vec{B} &= \vec{B}_0 + \vec{B}_1(\vec{r},t),\\ \vec{v} &= \vec{0} + \vec{v}_1(\vec{r},t),\\ p &= p_0 + p_1(\vec{r},t),\\ \rho &= \rho_0 + \rho_1(\vec{r},t).\end{aligned}$$

Here, subscripts are used to separate out the background ($\vec{B}_0$) and perturbation ($\vec{B}_1$) quantities. There is assumed to be no background flow and that all perturbations are much smaller than the background value (e.g., $\vec{B}_0 \gg \vec{B}_1$).

This leads to the **linearised ideal MHD equations**,

$$\frac{\partial \rho_1}{\partial t} + (\vec{v}_1 \cdot \nabla)\rho_0 + \rho_0(\nabla \cdot \vec{v}_1) = 0, \qquad \text{(Mass Conservation)}$$

$$\rho_0 \frac{\partial \vec{v}_1}{\partial t} = -\nabla p_1 + \frac{1}{\mu_0}(\nabla \times \vec{B}_1) \times \vec{B}_0 + \rho_1 \vec{g}, \qquad \text{(Equation of Motion)}$$

$$\frac{\partial p_1}{\partial t} + (\vec{v}_1 \cdot \nabla)p_0 - v_s^2 \left(\frac{\partial \rho_1}{\partial t} + (\vec{v}_1 \cdot \nabla)\rho_0 \right) = 0, \qquad \text{(Energy Equation)}$$

$$\frac{\partial \vec{B}_1}{\partial t} = \nabla \times (\vec{v}_1 \times \vec{B}_0), \qquad \text{(Induction Equation)}$$

$$\nabla \cdot \vec{B}_1 = 0, \qquad \text{(Solenoid Equation)}$$

where it is possible to define the first characteristic speed in MHD, the sound speed, $v_s^2 = \gamma p_0/\rho_0$. There is another important characteristic speed and that is the Alfvén speed, $v_A^2 = B_0^2/\mu_0\rho_0$. The type of waves supported by the plasma depends on the background plasma conditions and the geometry of the magnetic fields.

1.6.1 Waves in a uniform magnetic field

The model, in this case, is an infinite atmosphere with a background magnetic field that is purely vertical. Alfvén waves are incompressible transverse waves and with magnetic tension being the restoring force. The plasma motion due to the waves occurs perpendicular to the wave vector and the magnetic field. The group velocity $\omega/|k|$ at which Alfvén wave energy travels along field lines is the Alfvén speed, where k is the wave numnber,

$$v_A = \frac{B}{\sqrt{\mu_0 \rho}}. \tag{1.21}$$

When the ratio of gas to magnetic pressure, $\beta \ll 1$, then $v_A \gg v_s$. The phase speed of the wave pattern is given by,

$$\frac{\omega}{|k|} = \pm v_A \cos\theta \,, \tag{1.22}$$

where ω is the angular frequency of the wave, $\vec{k}$ is the wave vector, and θ is the angle between $\vec{B}$ and $\vec{k}$. Alfvén waves allow for energy to be transported into the corona. They are thought to be partially responsible for heating and accelerating the fast solar wind (Akasofu, 1981; Goldreich & Sridhar, 1995; Schwenn, 2006).

Magnetoacoustic waves come in two forms: “fast" and “slow". Fast waves propagate near isotropically and are governed by magnetic tension in media where $\beta \ll 1$ or by gas pressure when $\beta \gg 1$. The phase speed is given by,

$$v_{p,fast} = \frac{\omega}{k} = \left(\frac{1}{2}(v_A^2 + v_s^2) + \frac{1}{2}\sqrt{(v_A^2 + v_s^2)^2 - 4v_A^2 v_s^2 \cos^2\theta}\right)^{1/2}, \tag{1.23}$$

where v_s is the speed of sound in the plasma. For waves propagating parallel to $\vec{B}$, $v_{p,fast} = v_A$ or perpendicular to $\vec{B}$, $v_{p,fast} = \sqrt{v_A^2 + v_s^2}$. Slow waves mostly propagate along $\vec{B}$ and are governed by gas pressure when $\beta \ll 1$. Their phase speed is given by,

$$v_{p,slow} = \frac{\omega}{|k|} = \left(\frac{1}{2}(v_A^2 + v_s^2) - \frac{1}{2}\sqrt{(v_A^2 + v_s^2)^2 - 4v_A^2 v_s^2 \cos^2\theta}\right)^{1/2}. \tag{1.24}$$

Table 1.1 summarises how various MHD wave modes behave within this model. Three wave modes are present in this model, the Alfvén mode, the fast mode and the slow mode.

1.6.2 MHD waves in flux tubes

Magnetic flux tubes are modelled as cylindrical structures. In the context of a magnetic flux (cylindrical) tube, only the fast and slow modes are discussed. The seminal work in this study was undertaken by Edwin & Roberts (1983). The analysis is based on the slender flux tube, where the tube radius is greater or equal to the wavelength of the oscillations, the effects of gravity are ignored there.

It is important to note that in thin flux tubes, there are two other characteristic wave speeds. One is a subsonic, sub-Alfvénic speed, v_T (Equation 1.6.2), and the other is the kink or “mean” Alfvén speed, v_k.

The model is as follows, a cylindrical magnetic flux tube of radius a with its own density (ρ_0), pressure (p_0) and magnetic field ($B_0\hat{\mathbf{z}}$) is embedded in a magnetic environment with a similar profile ($B_e\hat{\mathbf{z}}$, ρ_e and p_e). The density and pressure are

		$\beta \gg 1, v_A \ll v_s$	$\beta \ll 1, v_A \gg v_s$
$\vec{k}\cdot\vec{v}_1 = 0$	$\vec{k}\|\|\vec{B}$	Alfvén wave, $v_{ph}^2 \sim v_A^2$	Alfvén wave, $v_{ph}^2 \sim v_A^2$
	$\vec{k}\perp\vec{B}$	Alfvén wave – does not propagate	Alfvén wave – does not propagate
$\vec{k}\cdot\vec{v}_1 \neq 0$	$\vec{k}\|\|\vec{B}$	Fast wave, $v_{ph}^2 \sim v_s^2$ approximately isotropic magnetic and gas pressure in phase Slow wave, $v_{ph}^2 \sim v_A^2$ magnetic and gas pressure out of phase	Fast wave, $v_{ph}^2 \sim v_A^2$ approximately isotropic magnetic and gas pressure in phase Slow wave, $v_{ph}^2 \sim v_s^2$ magnetic and gas pressure out of phase
	$\vec{k}\perp\vec{B}$	Fast wave, $v_{ph}^2 \sim v_s^2$ approximately isotropic magnetic and gas pressure in phase Slow wave – does not propagate	Fast wave, $v_{ph}^2 \sim v_A^2$ approximately isotropic magnetic and gas pressure in phase Slow wave – does not propagate

Table 1.1 The behaviour of each MHD wave mode in a uniform unbounded magnetised plasma. It summarises the phase speeds, propagation direction and the effect of varying plasma-β on each MHD wave mode. Adapted from Jess et al. (2015).

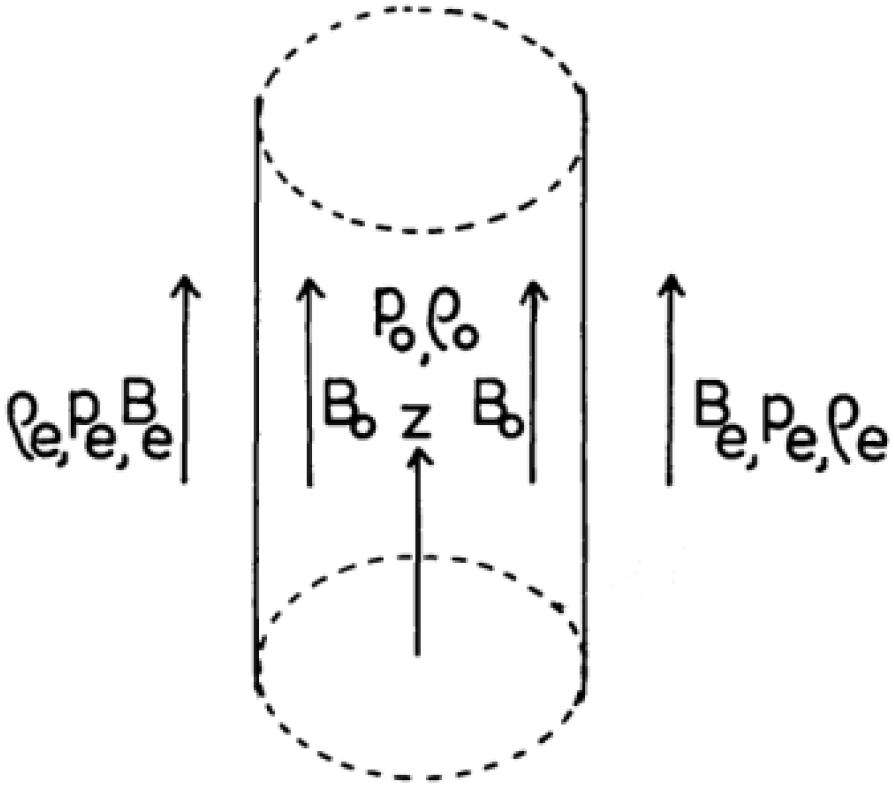

Fig. 1.15 The equilibrium conditions used to model wave behaviour in a magnetic flux tube. Image is a modified version of Figure 1 from Edwin & Roberts (1983).

uniform throughout the external medium. Figure 1.15 is a schematic drawing of this model.

This is the starting point for deriving the dispersion relation for MHD waves in a magnetic flux tube. It is assumed that this system is in equilibrium. Perturbations to the equilibrium conditions then add extra terms to the ideal MHD equations (the equations in Section 1.5.1). By introducing the Fourier decomposition of the perturbations, they show that the amplitude of the waves obeys the Bessel equation. When bound on the axis of the cylinder ($r = 0$), two solutions exist for either the body or surface wave. In the external atmosphere, the assumption of no propagation of energy away from or towards the cylinder allows the solution for the amplitude to be found. Furthermore, the kinetic and magnetic energy density tends to zero as $r \to \infty$. Continuity of perturbations at the boundary ($r = a$) has to be kept (radial velocity component v_r, and the total pressure) which yields the dispersion relations

for surface waves and body waves (Edwin & Roberts, 1983). These are,

$$\rho_0(k^2v_A^2-\omega)m_e\frac{K_n'(m_ea)}{K_n(m_ea)}=\rho_e(k^2v_{Ae}^2-\omega)m_0\frac{I_n'(m_0a)}{I_n(m_0a)}, \text{Surface, } \mathrm{m}_0^2>0 \quad (1.25)$$

$$\rho_0(k^2v_A^2-\omega)m_e\frac{K_n'(m_ea)}{K_n(m_ea)}=\rho_e(k^2v_{Ae}^2-\omega)n_0\frac{I_n'(n_0a)}{I_n(n_0a)}, \text{Body, } \mathrm{m}_0^2=-n_0^2<0 \quad (1.26)$$

where, K_n and I_n are modified Bessel functions of order n, K_n' and I_n' are the derivatives of the modified Bessel functions, m_0 and m_e are the internal and external wavenumber, defined as,

$$\frac{(k^2v_s^2-\omega^2)(k^2v_A^2-\omega^2)}{(v_s^2+v_A^2)(k^2v_T^2-\omega^2)},$$

and v_T is the tube speed,

$$v_T^2=\frac{v_s^2v_A^2}{v_s^2+v_A^2}.$$

Finally, these dispersion relations are solved under coronal conditions (plasma-$\beta << 1$, such that, $v_s \ll v_A < v_{A_e}$) and the solutions are displayed in Figure 1.16.

These dispersion relations are important as they detail the way in which waves propagate through numerous flux tube sizes. It shows the limits of the wave solutions indicating in what regimes they cannot exist.

If one can measure the phase speed of an observed wave and the k_z of the flux tube, one can also likely identify the observed waves. One factor that has been neglected is the azimuthal mode number (n), its value governs the way in which the wave perturbs the flux tube. This gives us the names: sausage ($n=0$), kink ($n=1$) and fluting ($n>1$) (See Figure 1.17). These different wave modes cause characteristic physical effects which can be used to identify each different wave mode, by using the observational resources available.

1.7 Observation of MHD waves

The launch of the Transition Region And Coronal Explorer (TRACE Strong et al. 1994; Handy et al. 1999a) satellite changes the study of waves in plasma forever. The discovery of waves is of interest in its own right, but the topic gained its spotlight because of the role it played in the development of coronal magneto-seismology (Edwin & Roberts, 1983). The notion of local seismology was not explored until the work of (Roberts et al., 1984), which exploited the wave diagrams as shown in Figure 1.16 and explicitly stated that "magneto-acoustic oscillations provide a potentially useful diagnostic tool for determining physical conditions in the inhomogeneous corona". They argued that the combination of theory and observations provides "a valuable diagnostic tool for in situ conditions in the corona",

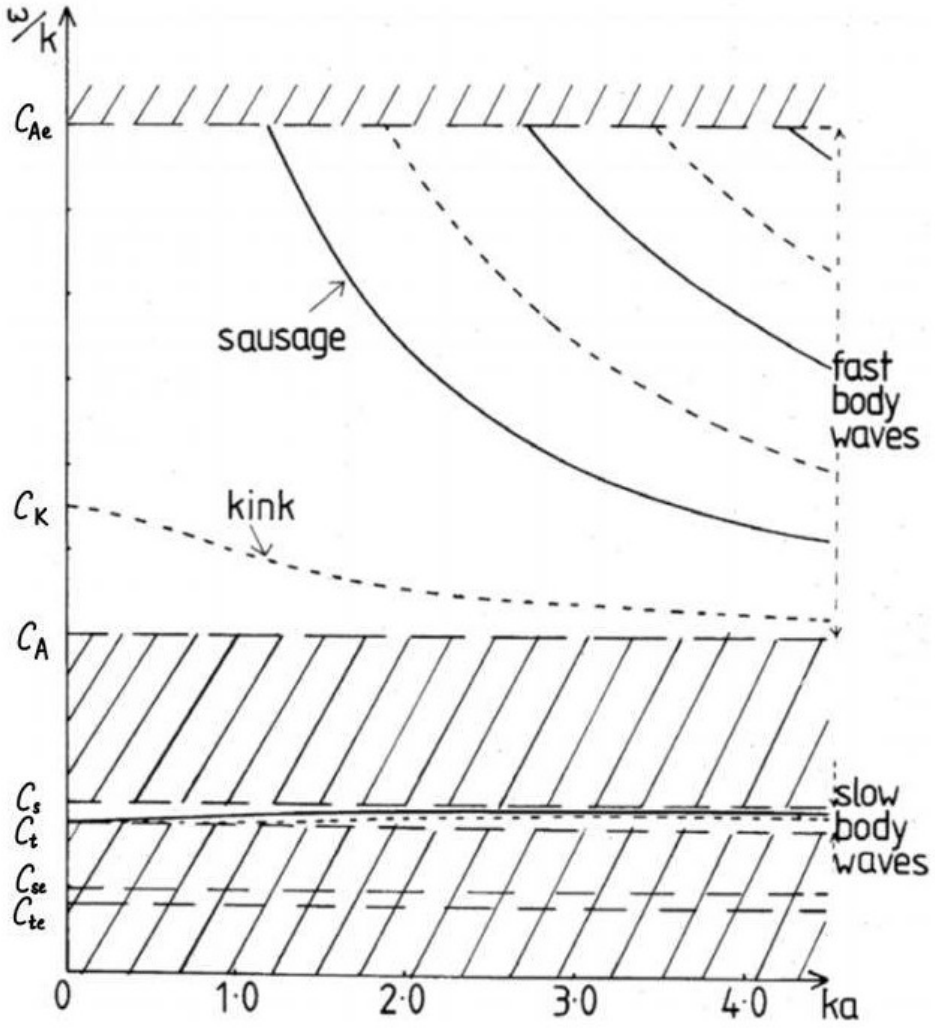

Fig. 1.16 The dispersion diagram derived from the MHD equations under coronal conditions ($v_s \ll v_A < v_{A_e}$). The hatched areas are the excluded values of ω and k_z. The diagram gives the phase speed $c(=\frac{\omega}{k_z})$ as a function of the dimensionless wavenumber k_z a for fast and slow magnetoacoustic body modes in a coronal magnetic flux tube. Solid curves correspond to sausage waves, dashed curves to kink waves. Image is a modified version of Figure 2 from Edwin & Roberts (1983).

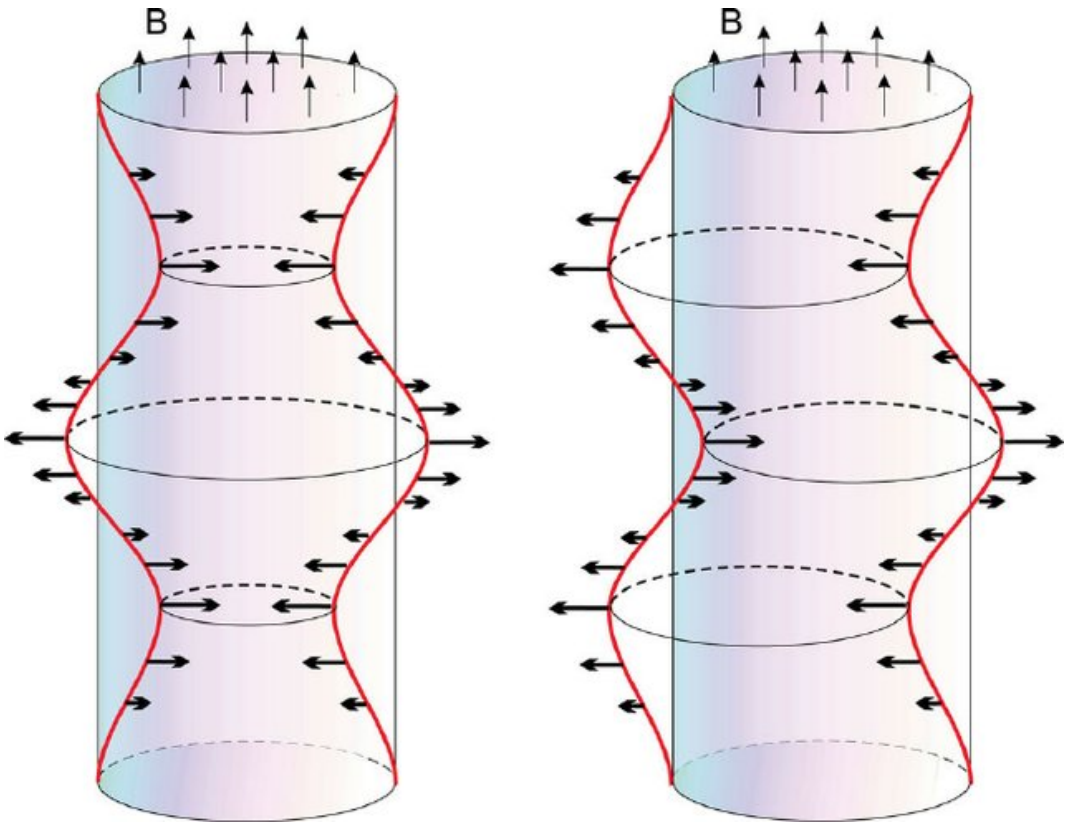

Fig. 1.17 Cartoon illustrating for the MHD waves in a magnetic flux tube. *Left:* Sausage wave with, $m = 0$ is characterized with an axisymmetric contraction and expansion of the tube's cross-section producing periodic compression/rarefaction of both the plasma and magnetic field. *Right:* The kink wave has an azimuthal wavenumber $m = 1$. It is the only value of m that can cause a transverse displacement of the flux tube. In contrast to the sausage wave, the kink wave displacement/velocity field is not axi-symmetric about the flux tube axis. The red lines indicate the perturbed flux tube boundary and thick arrows show the corresponding displacement vectors. The thin arrows labelled B show the direction of the background magnetic field. Image courtesy Morton et al. (2012a).

allowing determination of the local Alfvén speed and spatial dimension of the coronal inhomogeneity that forms a loop. There is, of course, no reason why such concepts cannot be equally applied to other magnetic features of the Sun e.g. sunspots, leading to magneto-seismology.

The dispersion diagram shown in Figure 1.16 is applicable to both propagating modes and standing modes, it can be used to aid the interpretation of observations of coronal waves. Standing waves occur in closed structures such as coronal loops, provided the wave has had time to travel the length of the loop and back again; for shorter times, the wave has not reached the ends of the loop, where it is reflected from the dense lower atmosphere, and thus the wave propagates freely as if the structure were open.

Since since the launch of SoHO and TRACE, a plethora of wave modes have been observed in the solar atmosphere. A non exhaustive list is provided as follows:

- Standing fast kink waves (Aschwanden et al., 1999; Nakariakov et al., 1999; Schrijver et al., 1999; Ofman & Aschwanden, 2002; Verwichte et al., 2005),
- Standing slow magnetoacoustic modes (Wang et al., 2003),
- Fast sausage waves (Williams et al., 2001, 2002; Katsiyannis et al., 2003),
- Propagating slow magnetoacoustic modes (Ofman et al., 1997; DeForest & Gurman, 1998; De Moortel et al., 2000; Marsh et al., 2002),
- Torsional modes (Erdélyi et al., 1998; Jess et al., 2009; Kohutova et al., 2020), and
- Propagating kink waves (Tomczyk et al., 2007; Tomczyk & McIntosh, 2009; Morton et al., 2012b, 2016; Morton et al., 2019).

Coronal magneto-seismology provides us with tools that allow the estimation of the background properties of coronal loops using the observed properties of these waves. For a review of coronal magneto-seismology, measuring magnetic field strength and density please see De Moortel (2005); Nakariakov & Verwichte (2005); Banerjee et al. (2007); Nakariakov (2007); De Moortel et al. (2016); Nakariakov et al. (2016b); Wang (2016); Van Doorsselaere et al. (2020); De Moortel et al. (2020).

1.7.1 Standing kink waves

Transverse waves created a buzz in the solar physics community since their first discovery after the launch of the TRACE (Handy et al., 1999b). These observations were very exciting for solar observations as one could directly measure displacement of coronal loops. These waves were interpreted as the coronal standing fast kink mode waves and were initially modelled in terms of linearized waves in (straight) homogeneous cylindrical flux tubes, but more realistic models include the effects of gravitational stratification, geometric expansion with height, curvature of the guiding magnetic field, non-circular cross-section, geometric loop shape, (helical) magnetic twist, and wave damping have been investigated since (Ruderman & Erdélyi, 2009; Hindman & Jain, 2013). For the observational signatures of transverse MHD modes, including sausage and Alfvén modes see (Hinode Review Team et al., 2019, chapter 6.1).

These observations found the wave speed to be larger than the sound speed suggesting that a fast magnetoacoustic or Alfvén wave was involved. The observations make clear that the loop as a whole (i.e. central axis) is disturbed, in a manner akin to the kink mode rather than an Alfvén wave. Thus, the observations were interpreted to be associated with the kink mode of oscillation. This observation established the presence of standing kink waves and led to several follow up studies.

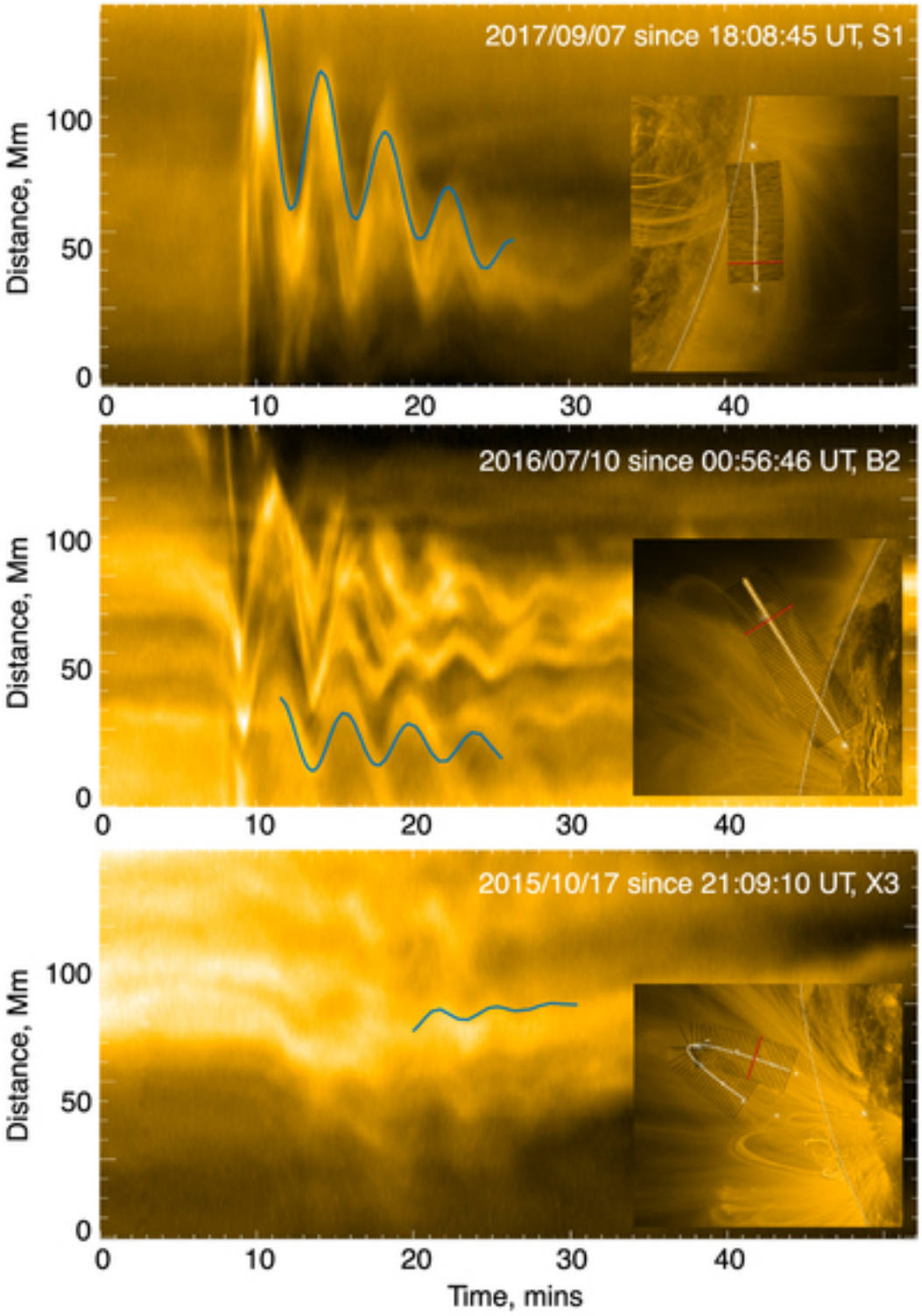

Fig. 1.18 Examples of observations of standing kink oscillations (SDO). The left panels show time-distance diagrams of the kink oscillations. The blue curves show best-fit exponential decay model. The inset images shows the active region with loops, and the red line corresponds to the slit used to generate the time-distance diagram. Image borrowed from Nechaeva et al. (2019)).

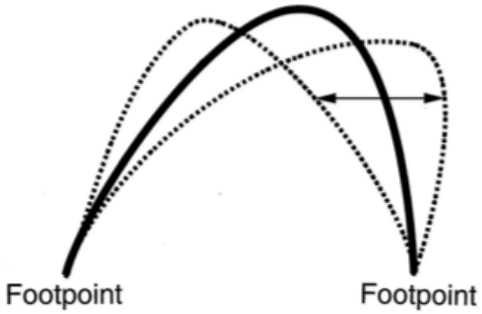

Fig. 1.19 A cartoon diagram of the fundamental of the standing kink oscillations. This simple model represents a vast majority of the standing kink waves in observations (Zimovets & Nakariakov, 2015). Image credits Nakariakov et al. (1999).

The common feature of these observations was the excitation mechanism, all of these standing kink waves were excited sporadically in coronal loops after a nearby flare (e.g. Aschwanden et al., 1999; Nakariakov et al., 1999).

For standing kink mode (for observations see Figure 1.18),

$$v_k = \frac{2L}{NP_k}, \tag{1.27}$$

where v_k is the kink speed, L is the observed loop length, N is the mode of oscillation and P_k is the period of the kink wave, a schematic representation of loop used for modelling is shown in Figure 1.19. The kink speed is determined by,

$$v_k^2 = \frac{\rho_0 v_A^2 + \rho_e v_{Ae}^2}{\rho_0 + \rho e}, \tag{1.28}$$

where the v_A is the Alfvénspeed *within* the slab, v_{Ae} is the Alfvénspeed in the environment, $\rho_0, \rho e$ are the external and internal densities of the loop respectively. Assuming the low β in corona, the outer magnetic field ($|B_0|$) is similar to the inner magnetic field ($|B_e|$) that reduces the the kink speed to,

$$v_k^2 = \frac{2B_0^2}{\mu_0(\rho_0 + \rho e)}. \tag{1.29}$$

Using this equation of kink speed with the Equation 1.27 provides us with an equation to measure the magnetic field,

$$B_0^2 = 2\mu_0\rho_0 \left(1 + \frac{\rho_e}{\rho_0}\right) \left(\frac{L}{NP_k}\right)^2. \tag{1.30}$$

The Equation 1.30 forms the basis of coronal magneto-seismology using standing kink waves.

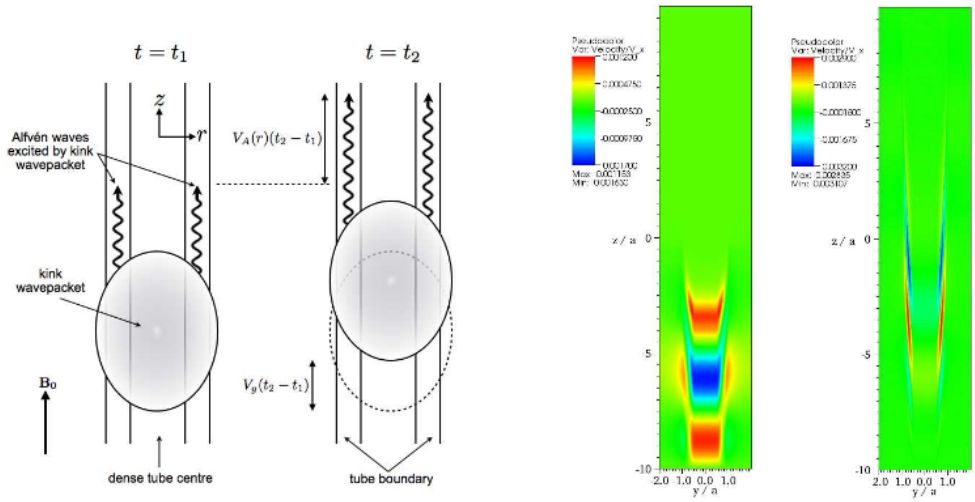

Fig. 1.20 Cartoon illustration of resonant absorption for a propagating transverse footpoint motion. Snapshots of the transverse velocity (taken from (Pascoe et al., 2010)) at two different timesteps in the simulations, for a density contrast and a boundary layer. This shows the accumulation of energy from the axial component to the azimuthal component.

Since the early observations from TRACE, there have been several studies to understand the excitation mechanism, damping mechanism, and the statistics of the standing kink waves. It was immediately recognized that the measurement of the fast kink mode period P, the length of the oscillating loop L, and the electron density (n_e), provides a measurement of the mean magnetic field $|B|$ in an oscillating loop, which became the most prominent tool of the coronal magneto-seismology method (Nakariakov & Ofman, 2001). The rapid damping was attributed to resonant absorption, a phenomenon present in inhomogeneous plasmas converting the energy in transverse motions to azimuthal motion via resonant coupling (e.g. Ruderman & Roberts, 2002; Goossens et al., 2002; Aschwanden et al., 2003; Hindman & Jain, 2018). In the presence of structuring in the direction perpendicular to the magnetic field (i.e. the loop plasma is considered denser than the ambient plasma), transverse motions generate an intrinsic coupling between the kink (transverse) and torsional Alfvén (azimuthal, $n = 1$) modes. The coupling takes place in a dissipative layer at the loop boundary, located at the resonant point where the kink frequency, which lies between the internal and external Alfvén frequencies, matches the local Alfvén wave frequency (e.g. Aschwanden et al., 2003; Goossens et al., 2006; Antolin et al., 2015).

Due to the TRACE, SoHO and SDO instruments there has been a constant coverage of the sun. These observations have provided a large sample of damped kink oscillations. Recently there has been several attempts to understand the excitation mechanism, damping mechanism, and the statistics of the standing kink waves (Stepanov et al., 2012; Goddard et al., 2016). The statistics of the standing waves

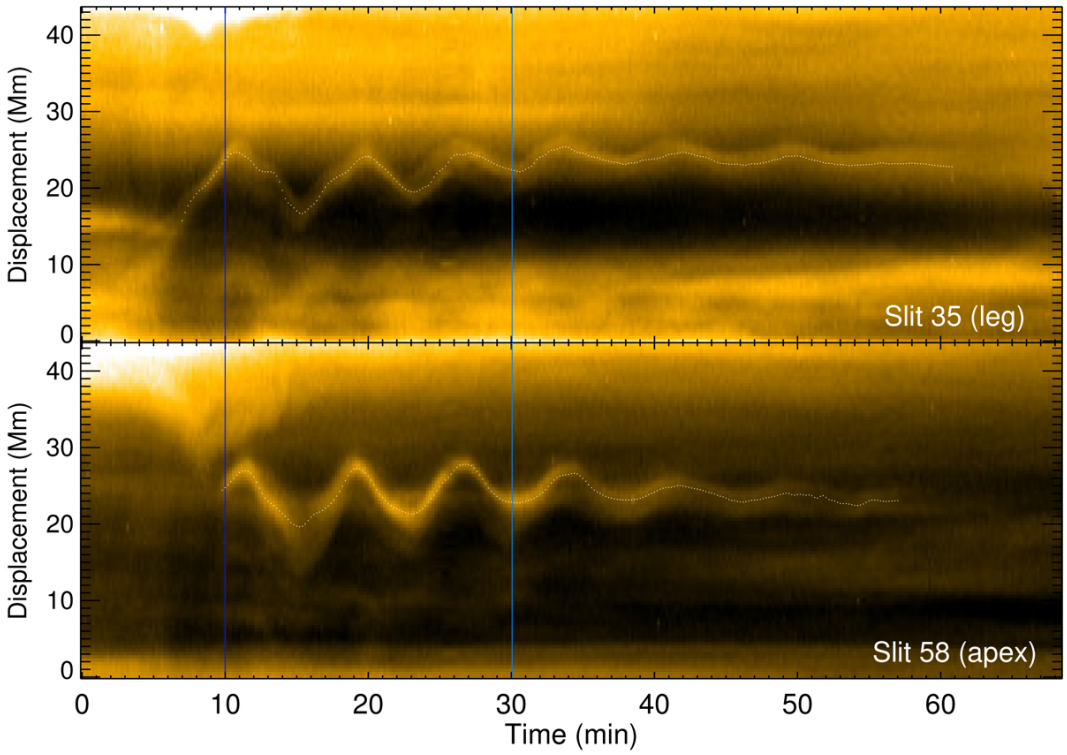

Fig. 1.21 An example of time-distance diagram used to study the damping of standing kink waves. The image is borrowed from (Duckenfield et al., 2018). The top panel represents the time-distance diagram at the loop footpoint and the bottom panel shows the time-distance diagram from the loop apex.

provide important clues about the excitation of these waves. Zimovets & Nakariakov (2015) reported that the kink oscillations were excited by the deviation of loops from their equilibria by a nearby low coronal eruption in 95% of their sample of 58 events under study. It should be noted that these refer to the large amplitude standing kink oscillations.

Recently various harmonics of the kink waves have been observed. The period ratio $P_1/(2P_2)$ in a uniform loop is unity, as it is for waves on a uniform string. However, in a non-uniform loop, the period ratio departs from unity; this provides a potentially useful diagnostic tool for the analysis of the extent of longitudinal structuring in coronal loops where multiple harmonics have been detected (Verwichte et al., 2004; Van Doorsselaere et al., 2007; De Moortel & Brady, 2007; Pascoe et al., 2016a; Duckenfield et al., 2018). The third harmonic of the decaying kink oscillations was detected by studying the distribution of spectral power of the oscillatory transverse displacements throughout the loop. The presence of two harmonics, a fundamental($P_1 \sim$8 min) and the third harmonic($P_3 \sim$2.6 min). The node of the third harmonic was reported to be found at approximately a third of the way along the length of the loop (see Figure 1.21), and cross-correlations between the oscillatory motion on opposing sides of the node showed a change in phase behaviour.

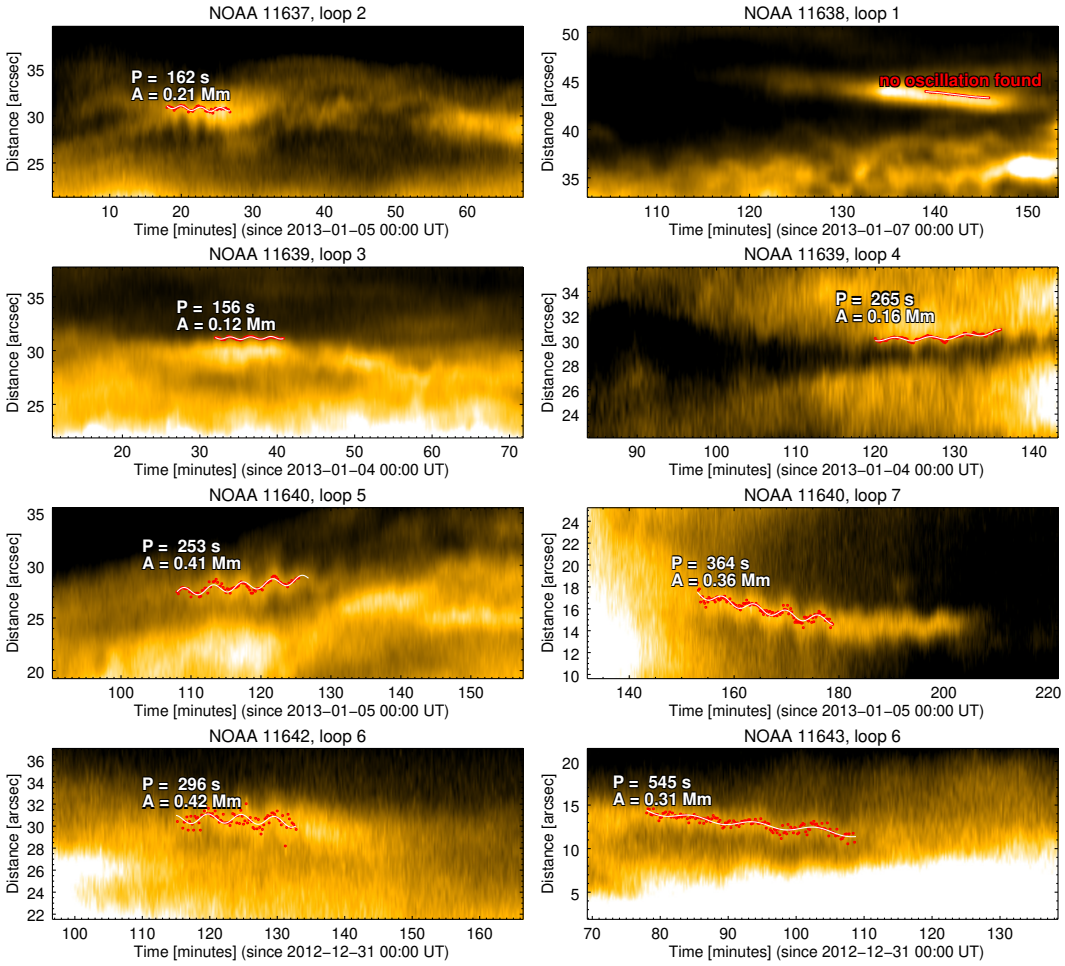

Fig. 1.22 AIA/SDO obervations of decayless standing kink waves. Time-distance maps of the oscillating loops found in the analysed active regions. Image courtesy (Anfinogentov et al., 2015).

1.7.2 Decayless standing kink waves

A new kink wave mode was recently discovered using the AIA/SDO. These wave modes are called the decayless standing kink oscillations. Unlike the damped standing kink oscillations these transverse oscillations are not associated with any external phenomena. These wave modes have significantly lower amplitudes ($<$ 1 Mm) than the decaying oscillations (Anfinogentov et al., 2013; Nisticò et al., 2013). A statistical study of these waves was performed by Anfinogentov et al. (2015), revealing the nature of these waves. There have been some numerical studies to reproduce such decayless oscillations in the form of footpoint driven standing waves in coronal loops. A set of observations from the AIA/SDO images are shown in Figure 1.22.

The interpretation of these waves has changed over years. Some of such interpretations are a.) self-oscillatory process due to the interaction of the loops with quasi-steady flows (Nakariakov et al., 2016a), b.) continuously driven kink waves with a footpoint driver (Afanasyev et al., 2019; Karampelas et al., 2019) or as a

line of sight (LOS) effect from the development of the Kelvin-Helmholtz instability (KHI) in impulsive standing loop oscillations (Antolin et al., 2016).

1.7.3 Propagating kink waves

In contrast to the standing waves, there has been fewer observational studies on propagating kink waves. Nonetheless, there have been some observations which seem to have a natural interpretation in terms of propagating kink waves. These were only identified a decade ago (e.g. Okamoto et al., 2007; Tomczyk et al., 2007; McIntosh et al., 2011a; Thurgood et al., 2014; Morton et al., 2015) and they are found to be ubiquitous throughout the corona (see Figure 1.23). The excitation mechanism(s) of the propagating kink waves are still not evident. It is believed that horizontal motions of magnetic elements in the photosphere are a key driver of relatively high-frequency ($f > 1$ mHz) Alfvénic modes (e.g. Cranmer & Van Ballegooijen, 2005; Van Ballegooijen et al., 2011), although CoMP observations (see Section 2.2.1) (Tomczyk et al., 2007; Morton et al., 2016; Morton et al., 2019) suggest that the observed Alfvénic waves are, at least partially, excited by p-modes (Cally, 2017).

The role of resonant damping of propagating transverse waves is substantiated in 3D, full MHD numerical simulations (e.g. Pascoe et al., 2010, 2012; Magyar & Van Doorsselaere, 2016; Pagano & De Moortel, 2017, 2019). A schematic representation of the phenomenon of resonant absorption in numerical simulations is shown in Figure 1.20. The analytic treatment of damping of propagating kink waves along the magnetic flux tubes is attributed to the work done by Terradas et al. (2010). Several equations from this analytical treatment are used in this thesis, and are detailed below. Tomczyk & McIntosh (2009) noted that the propagating kink modes observed in a quiescent coronal loop were damped, with Terradas et al. (2010) and Verth et al. (2010) suggesting that resonant absorption provides a reasonable description of the observed damping.

The assumptions of the model that is used for this thesis results in an exponentially damped profile for the wave, which is assumed throughout the data analysis. Some studies suggest a role of Gaussian damping, especially during the initial phase (Pascoe et al., 2016b). CoMP observed waves that fall under the long-wavelength regime ($ka << 1$, tube radius is much much smaller than the wavelength), implying the damping length, L_D for these waves is given by

$$L_D = v_{ph} \xi \frac{1}{f}, \tag{1.31}$$

where v_{ph} is the phase speed, f is the frequency, and ξ is the equilibrium parameter (named as it can be calculated precisely for a particular equilibrium model). The ξ

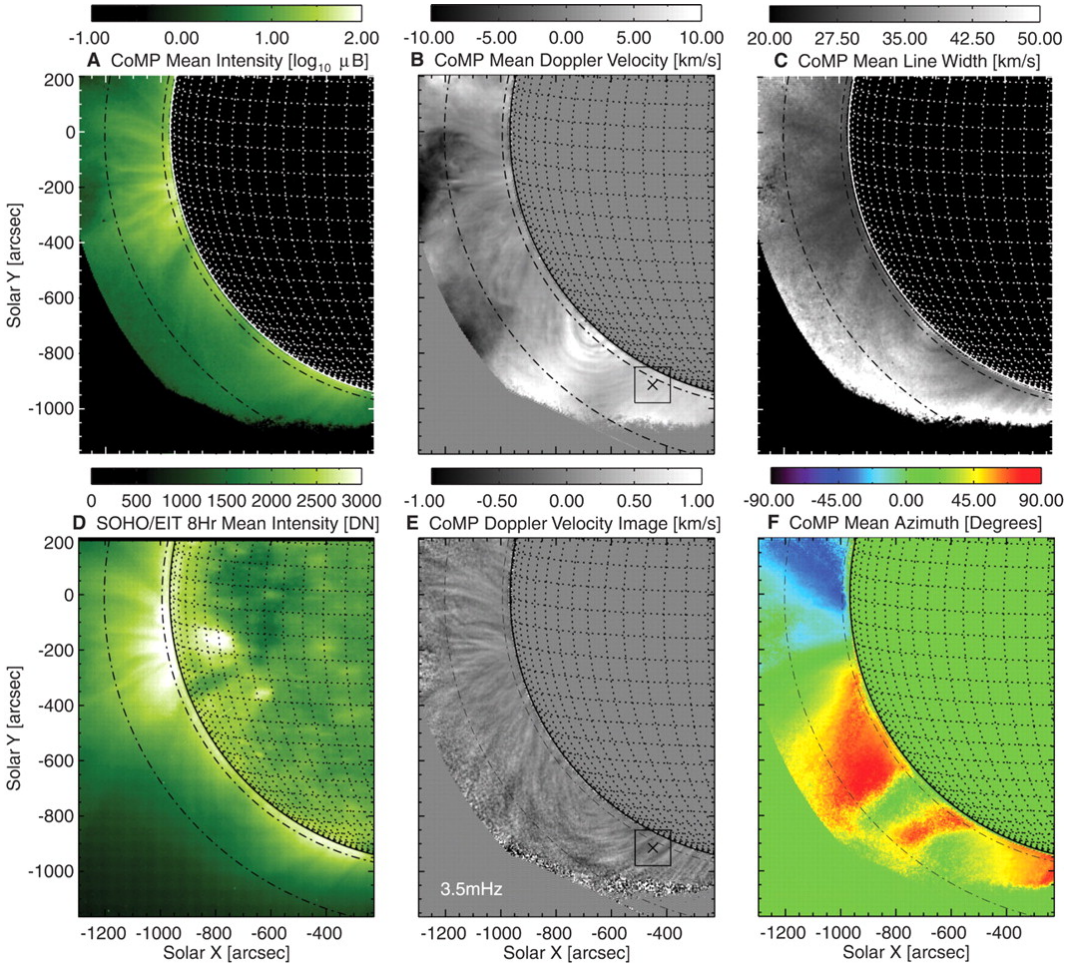

Fig. 1.23 CoMP observations of time-averaged intensity (A), Doppler velocity (B), line width (C), 3.5-mHz filtered Doppler velocity snapshot (E), and POS azimuth (F), The SOHO/EIT 195 Åimage averaged over the same time as CoMP observations (10747 Å). Dot-dashed lines representing distances of 5 and 25% of $R_{\odot}$.

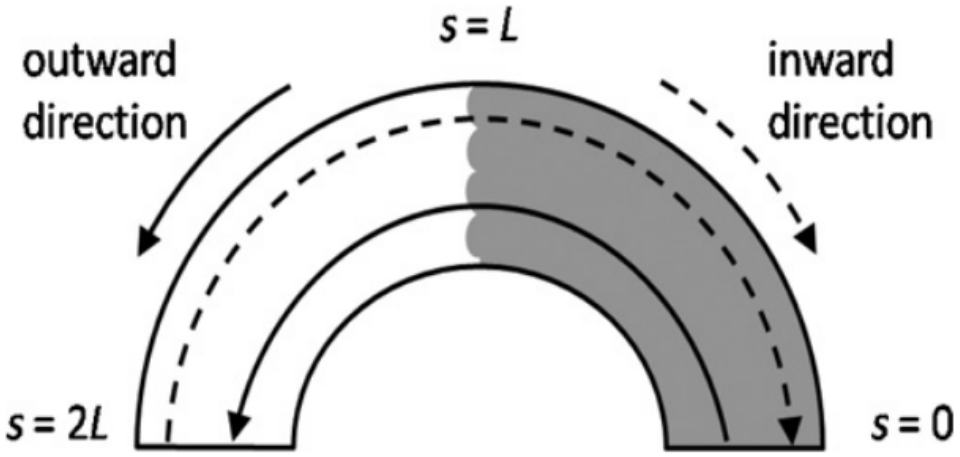

Fig. 1.24 Illustration of the observed semi-circular geometry of the coronal loop system. The integrated wave paths are approximately only half the length along the total loop system. The direction of outward and inward wave propagation is shown by the solid and dashed lines, respectively (Verth et al., 2010).

incorporates the physical conditions of the flux tube and can be written as

$$\xi = \alpha \frac{1}{n} \frac{R}{\ell} \frac{\rho_i + \rho_e}{\rho_i - \rho_e}, \quad m > 0 \tag{1.32}$$

where n is the mode number, R is loop radius, ℓ is the thickness of the density inhomogeneity layer, ρ_i and ρ_e are internal and external densities of the magnetic flux tube, respectively, and α is a constant whose value describes the gradient in density across the resonant layer. The equilibrium parameter is a dimensionless quantity, and can be written in terms of the wavelength λ,

$$\xi = \frac{L_D}{\lambda}, \tag{1.33}$$

hence ξ can also be interpreted as the quality factor of the wave damping. Higher quality factor implies a lower rate of damping. Verth et al. (2010) used the CoMP observations of Tomczyk & McIntosh (2009) to estimate the equilibrium parameter (see Figure 1.25). In Verth et al. (2010), the study was performed on half of a coronal loop and assuming the kink waves at the coronal footpoint of the segment (driven by a non-specific mechanism) have a certain power spectrum, $P_{out}(f)$, where the subscript *out* refers to the fact they are outwardly propagating along this segment. They propagate along the loop and are damped to some degree when they reach the loop apex, at a distance L from the coronal base (considered the half-loop length). Waves are also excited at the other footpoint, likely with a similar power spectrum, $P_{in}(f)$, and are denoted as inwardly propagating. By the time they have reached the apex they have already travelled a distance L, and are damped further as they propagate down towards the first footpoint (see Figure 1.24).

Assuming exponential damping, average power spectra of the outward and inward waves along the half-loop segment of interest can be calculated, and the ratio of the two integrated power spectra is found to be

$$\langle P(f) \rangle_{ratio} = \frac{P_{out}(f)}{P_{in}(f)} \exp\left(\frac{2L}{v_{ph}\xi} f\right). \tag{1.34}$$

The fit of the equation as obtained by Verth et al. (2010) is shown in Figure 1.26.

This expression provides the underlying model for further analysis of propagating kink waves. Utilizing data from CoMP enables us to provide estimates for: the values of the inward and outward power spectra as a function of frequency, the half-loop length and the propagation speed of the waves. This, in combination with Equation (1.34), provides us with a means to measure the quality factor (ξ) if $\langle P(f) \rangle_{ratio}$ is known. Despite their ubiquity, there have been relatively few observational studies of the propagating kink waves. The focus of this thesis is these propagating kink waves and the statistical properties of these waves to advance our understanding

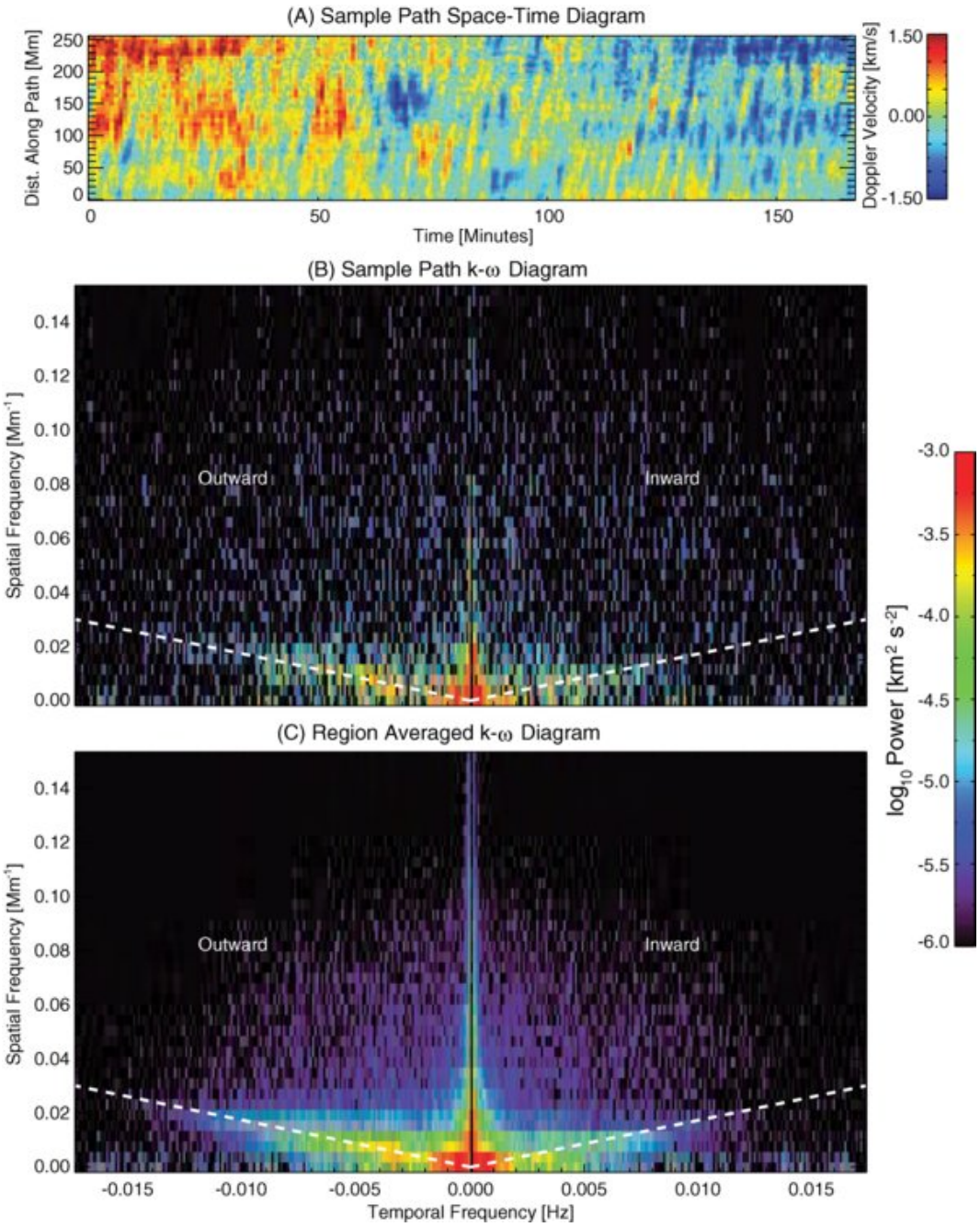

Fig. 1.25 (A) CoMP space-time diagram for a sample wave path, (B) the $k-\omega$ diagram for that space-time diagram, and (C) the averaged $k-\omega$ diagram for the region around the sample wave path.

of these ubiquitous propagating kink waves, utilising the CoMP observations of the Doppler velocity images of the solar corona in the near infrared part of the electromagnetic spectrum. Chapter 3 discusses the role of power ratio in studying the damping of the propagating kink waves. It also demonstrates that the analysis of power spectra and their ratio requires the use of Maximum Likelihood Estimation (MLE) techniques in order to provide accurate parameter estimates and uncertainties. In Chapter 4 a statistical study of coronal loops observed in CoMP is undertaken to examine the typical properties of damped propagating kink waves. The results are

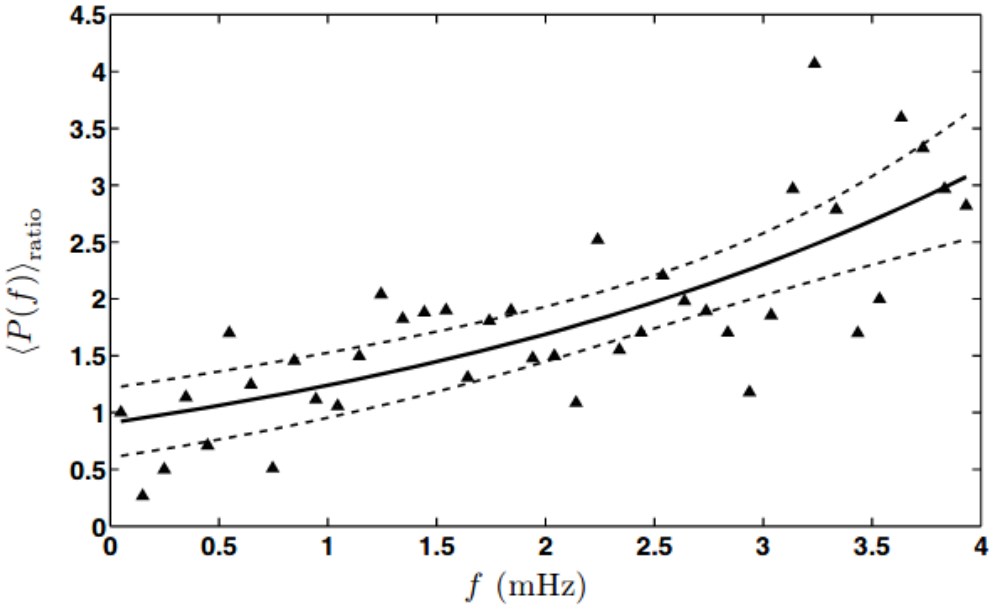

Fig. 1.26 Power ratio against frequency, showing the frequency-dependent damping. Solid line shows the best fit using Equation 1.34 with CoMP data (using lease-squares-estimate). The 95 % confidence intervals for the simultaneous functional bounds are shown by the dashed lines.

then compared to the statistical properties of the damped standing kink waves. For a recent review on the study on the waves in the solar corona, see (Roberts, 2019; Van Doorsselaere et al., 2020). This chapter tried to introduce the Sun and solar physics, for further details on the structure and fundamental features of the Sun, see, Priest (1984); Aschwanden (2004); Priest (2014) (Stix, 2004; Aschwanden, 2019).

1.7.4 Damping mechanisms of MHD waves

To understand the energy content carried by waves it is important to understand the damping mechanism of these waves. Study by Montes-Solís & Arregui (2017) explores the various damping mechanisms and the significance of these mechanisms in the coronal oscillations. The various damping mechanisms that try to explain damping of the MHD waves are:

Resonant absorption in the Alfvén continuum

The mechanism of resonant absorption consists of an energy transfer between the global kink mode of a magnetic flux tube to the Alfvén mode at the tube boundary (Hollweg, 1984). This is the consequence of transverse variation of Alfvén speed within a layer that separates the flux tube and the background plasma. Resonant absorption has been studied extensively (Goossens et al., 2002; Ruderman & Roberts,

2002) and studies have shown that this mechanism is able to explain the time and spatial damping scales in the observations.

The model setup focuses on the fundamental kink mode ($m = 0$) of a cylindrical density tube of length L and radius R with a uniform magnetic field along the axis of the tube and a non-uniform variation of the cross-field density length-scale l. The thin tube ($L \gg R$) and thin boundary ($l/R \ll 1$) assumptions are considered giving rise to the equilibrium parameter as in Equation 1.32.

Equilibrium parameter in the case of resonant absorption is a function of ρ_i/ρ_e and l/R. Goossens et al. (2002) showed that the mechanism is able to explain observed damping timescales for values of l/R in between 0.1 and 0.5, for a a typical density contrast of $\rho_i/\rho_e = 10$. Considering the typical values for density contrast ($\rho_i/\rho_e \in (1, 10]$) and $l/R \in (0, 2]$, the equilibrium parameter predicted by theory lie in a wide range $\tau_d/P \sim (0.5\text{–}10^4)$. This mechanism is assumed with the implicit underlying assumptions for the studies carried out in this thesis.

Phase mixing of Alfvén waves

The fundamental idea of phase mixing is that Alfvén waves propagating along the magnetic field through a medium with a transverse gradient of Alfvén speed become rapidly out of phase producing increasingly shorter spatial scales at the loop/tube boundary (Heyvaerts & Priest, 1983). This mechanism has been explored as a possible candidate to explain the observed rapidly damping of standing kink waves (Roberts, 2000; Ofman & Aschwanden, 2002; Nakariakov & Verwichte, 2005). The analytic expression for the equilibrium parameter in case of phase mixing is found to be,

$$\xi_E = \frac{\tau_d}{P} = \left(\frac{3}{\pi^2 \nu}\right)^{1/3} w^{2/3} P^{-1/3}, \tag{1.35}$$

where $\nu = 4 \times 10^3$ km^2 s^{-1} is the coronal shear viscosity coefficient and w the transverse inhomogeneity length scale. The equilibrium parameter is a function of the period. Considering typical values of the period in the range of $P \in [150, 1250]$s and $w \in [0.5, 20]$ Mm, equilibrium parameters in the range of $\xi_E \sim [0.3\text{–}6]$ are obtained, so this mechanism has the potential to explain the damping timescales observed in case of the damped standing kink waves (Nechaeva et al., 2019).

Wave leakage of the principal leaky mode

The basic idea for this mechanism consists of a radiating wave, which oscillates with the kink mode frequency and looses part of its energy to the background corona

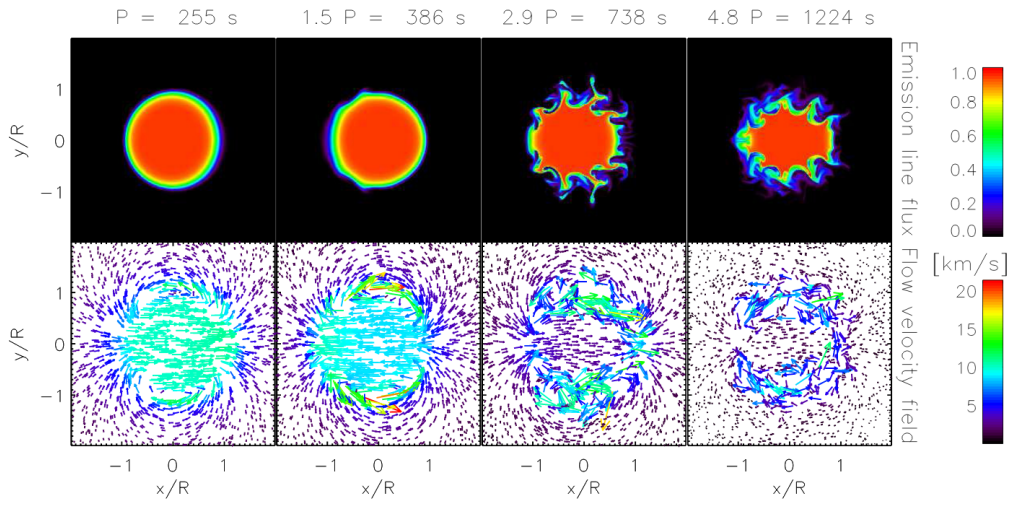

Fig. 1.27 Formation of KHI vortices at the loop boundary. The figures show the cross-section at the center of the loop. The top and bottom rows correspond to the emission line flux (at Fe IX 171.073 Å), and the flow velocity field, respectively. The columns represent snapshots of the simulation at four different times (Antolin et al., 2014).

(Cally, 2003). The analytical solution for the equilibrium parameter is of the form

$$\xi_E = \frac{\tau_d}{P} = \frac{4}{\pi^2}\left(\frac{R}{L}\right)^{-2}. \tag{1.36}$$

In this model also the thin tube approximation is taken into consideration along with the assumptions that $\rho_i \gg \rho_e$. For the typical values of $R/L \in [10^{-4}, 0.3]$, this model predicts equilibrium parameters in the range of $\xi_E \sim (0.5\text{–}10^5)$.

All these theoretical models of damping have some or the other implicit assumptions for simplicity. One of the major concerns for these models is the fact that these models treat all loops as having same physical features (radial density profile, temperature, viscosity, and density contrast) which need not necessarily true.

1.7.5 Dissipation of energy at kinetic scales

Energy budget calculation from damping does not mean that this energy is available for heating. The energy from damping needs to be dissipated. In numerical solutions and some observational studies Klevin-Helmholz Instability (KHI) induced vortices offer a possible way to dissipate the energy at the kinetic scales (Browning & Priest, 1984; Ofman et al., 1994). These KHI vortices have also shown to lead to a redistribution of the loop plasma during kink oscillations (Terradas et al., 2008; Soler et al., 2010; Antolin et al., 2014; Karampelas & Van Doorsselaere, 2018). A simulated loop showing the formation of these fine scale vortices at the loop boundary are shown in Figure 1.27.

Both the models of coronal heating require the dissipation at these kinetic scales making KHI votices one of the most important mechanism for dissipation (Karpen et al., 1993; Ofman et al., 1994; Antolin et al., 2014). This hydrodynamic instability has been directly observed in the large scale magnetic structures of the Sun e.g. coronal mass ejections (Foullon et al., 2011; Ofman & Thompson, 2011).

Chapter 2

Overview of data sources and analysis techniques

2.1 Introduction

The last two decades should be considered as the golden age of solar physics. The launch of several solar missions such as Solar Dynamics Observatory (SDO, launched 2010), Solar Terrestrial Relations Observatory (STEREO-A & B, launched 2006), Hinode (launched 2006), Interface Region Imaging Spectrograph (IRIS, launched 2013), Deep Space Climate Observatory (DSCOVR), Parker Solar Probe (PSP, launched 2019) and Solar Orbiter (SolO, launched 2020) and others, gives us unprecedented temporal, spectral and spatial resolution. PSP and SolO are going to provide us with a unique opportunity to study the Sun as never before. The commissioning of the various ground-based observing facilities such as GREGOR at Teide Observatory, Goode Solar Telescope (GST) at Big Bear Solar Observatory, Swedish 1-m Solar Telescope (SST), Richard B. Dunn Solar Telescope (DST), Daniel K. Inouye Solar Telescope (DKIST), GREGOR Solar Telescope, and other high-resolution solar telescopes including European Solar Telescope (EST), and National Large Solar Telescope (NLST, a proposed 2-metre class solar telescope) provide us with high-resolution images from the ground, with most advanced development in adaptive optics, optics and imaging technologies. Apart from these large and ambitious solar missions, several balloon experiment and rocket missions are providing us with very rich data to analyse and have a much closer look at our nearest star. As an example of how much we have achieved in solar observations, see Figure 2.1. DKIST is currently the largest solar telescope in the world. With a focus on understanding the Sun's explosive behaviour, observations of magnetic fields are at the forefront of this innovative telescope. A combination of an off-axis design, to reduce scattered light, and cutting edge polarimetry produces the first ongoing measurements of the magnetic fields in the Sun's corona. The DKIST's 4-metre mirror provides views of the solar atmosphere as we have never seen before (see Figure 1.5. DKIST has already created a buzz in the scientific community as well as the general public with its first light revealing the solar photosphere and the convective cells with an unimaginable resolution from Galilean times. These are indeed very exciting times for a solar physicist.

Not only the various high-quality observations are taken, but they are also put in the public domain. Several such data sources are used in the analysis presented in successive chapters. The details of the instrumentation and data used within this thesis, as well as discussing the details of some of the methodology employed to analyse the data are presented in this chapter. These analysis techniques will be used in the subsequent chapters.

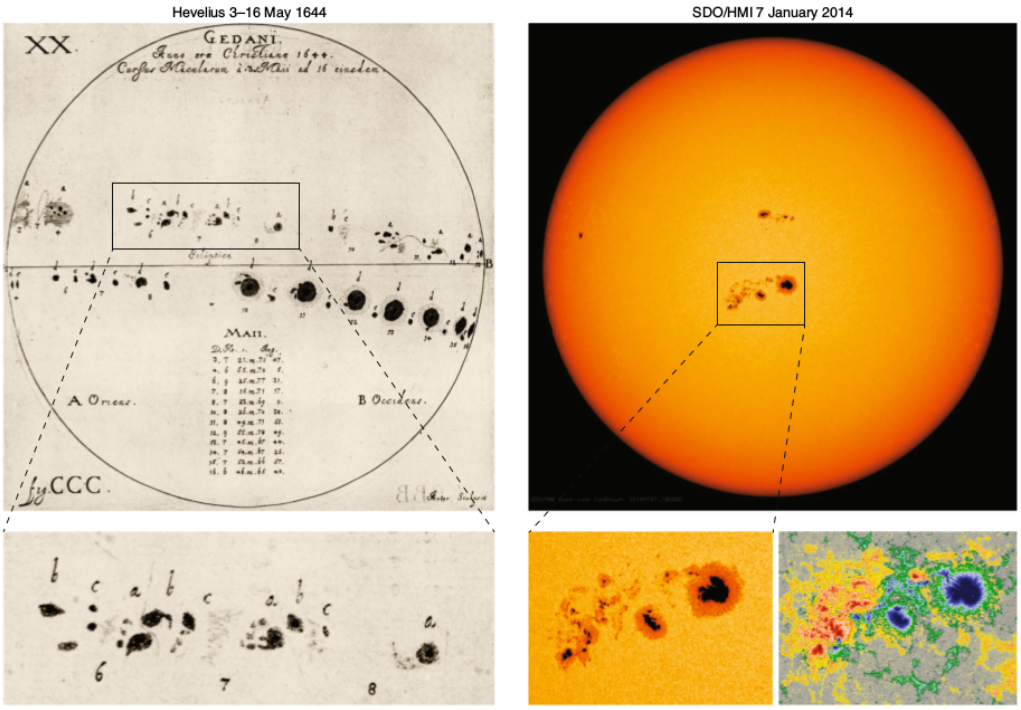

Fig. 2.1 Sunspot observations almost 400 years apart. *Left:* Historical observation of sunspot. Sunspots were tracked using the same solar disk. The closeup panel shows sunspot observations by Hevelius. Credit: Library of the Astronomical Observatory of the Spanish Navy *Right:* Solar observation using SDO launched in 2010. Image borrowed from (Muñoz-Jaramillo & Vaquero, 2019).

2.2 Data sources

2.2.1 COronal Multi-channel Polarimeter (CoMP)

The CoMP instrument (Tomczyk et al., 2008) is a ground-based telescope, situated at Mauna Loa Solar Observatory (MLSO), on the island of Hawaii. This is operated by the High Altitude Observatory (HAO)/ National Center for Atmospheric Research (NCAR). CoMP is a combination tunable filter and polarimeter. It is comprised of a) an occulting disk, to block the light from the solar disk; b) collimator lens for the solar image; c) a filter wheel holding three order-blocking filters corresponding to each of the three observable emission-line regions; d) the package of polarimeter/tunable filter; e) a re-imaging lens to generate the final solar image, and f) 1024 x 1024 pixel HgCdTe infrared detector array. CoMP equips us with the possibility to learn more about the magnetic field, plasma density and motions of the plasma in the solar corona. The measured polarization state is parameterized by a Stokes vector [I, Q, U, V], where I is the intensity, Q and U describe net linear polarization states, and V describes the net circular polarization. CoMP instrument summary:

- 1.3 Å filter bandpass.

- Fe XIII coronal emission line at 10747 Å and 10798 Å and also 1083.0 Å HeI chromospheric line.
- Field-of-view (FOV) 1.03 to 1.5 $R_{\odot}$.
- Platescale of 4.5 $''$ per pixel.
- Temporal resolution 30 sec.

The CoMP polarimeter is formed by a pair of Liquid Crystal Variable Retarders (LCVRs) followed by a linear polarizer that allows the selection of a polarization state parameterized by a Stokes vector [I, Q, U, V], where I is the intensity, Q and U describe net linear polarization states and V describes the net circular polarization. The CoMP polarimeter selects a Stokes state I±S where S is Q, U, or V. The CoMP filter is a four-stage, wide-field calcite birefringent filter with a bandwidth of 0.13 nm. It is tuned in wavelength by four additional LCVRs. The final element of the filter is a Wollaston prism, which splits the beam into the emission line and continuum band-passes. The line and continuum image pair are focused simultaneously onto the detector along the diagonal with a full field of view of 2.8 solar radii ($R_{\odot}$). The exposure time for the images is 250 ms and the image groups have a temporal cadence of 29 seconds. Once the images are taken, it needs to be reduced to be able to use for analysis. To reduce the images, the following steps are performed

- subtract a dark image;
- divide by an image taken with a calibrated diffuser in front of the objective lens to remove pixel-to-pixel detector gain variations;
- normalize the relative transmission of the filter bandpasses and normalize the intensity into units of the solar disk central intensity;
- determine the location of the images on the detector, translate to a common centre, and rotate to orient solar north up;
- subtract the continuum emission from the line emission;
- combine the images to produce Stokes I, Q, U and V images at each wavelength.

These steps result in images of the corona in the four Stokes parameters. The three-point data at, I_1, I_2 and I_3 are measured intensities at known wavelength (spectra positions), in this case the three wavelengths (10745.0 Å- I_1, 10746.2 Å- I_2 and 10747.4 Å- I_3) centered around 10747 Å(the Fe XIII emission line). These wavelengths have a peak formation temperature $\sim$ 1.6 MK. For each pixel in the CoMP FOV in each time frame the central intensity, Doppler shift and Doppler width

of the line profile is calculated using an analytic fit of a Gaussian to the intensity values at each wavelength position (Tian et al., 2013; Morton et al., 2016). The equations for these quantities are as follows:

$$v = \frac{w^2}{4d}(a-b), \tag{2.1}$$

$$w = \sqrt{\frac{-2d^2}{a+b}}, \tag{2.2}$$

$$i = I_2 \exp\frac{v^2}{w^2}, \tag{2.3}$$

where v is the Doppler velocity, w is the Doppler width (Doppler width is defined as $\sqrt{2}\sigma$, with sigma the standard deviation of the Gaussian) and i is the line centre intensity and d is the spectral step size. The a and b are functions of I_1, I_2 and I_3.

$$a = ln\frac{I_3}{I_2}, b = ln\frac{I_1}{I_2} \tag{2.4}$$

Once the line parameters are derived for each intensity profile. The maps for intensity, Doppler shift, and line width are generated for observations, to study the dynamics of the solar corona. The effects of the rotation of the Sun are also visible in the Doppler images. The east limb shows predominantly blue shift and the west limb shows a redshift. To correct for this, the median value of Doppler shift at each solar-x location is calculated to produce the East-West trend. A median filter is then applied to this trend to eliminate possible outliers. Then a fifth-order polynomial fit is applied to the filtered trend. The resulting smooth trend is then subtracted from the map of Doppler shift (Tian et al., 2013).

The data is preprocessed and is available in the public domain at the MLSO. [1] The data obtained from here is processed to the level-2 (suitable for scientific use), a sample of the available data products is shown in Figure 2.2. There are various pre-processing steps as discussed previously in this section, involved in getting the data to this level. All the data used for the analyses use these level-2 data sets. Further processing steps are required to study the waves. The intensity maps obtained from CoMP are then aligned using cross-correlation, because the images are not always centered properly due to the motion of telescope while tracking the Sun. As this study is about the study of waves, the aligning of the intensity image sequence is important, misaligned images can give rise to spurious periodicities in the observations. This was done by manually identifying a sharp contrast and stable feature, after applying an edge enhancing filter (Sobel filter) to the images. This feature serves as the basis for aligning successive images. The same shifts are

[1] https://mlso.hao.ucar.edu/mlso_data_calendar.php?calinst=comp

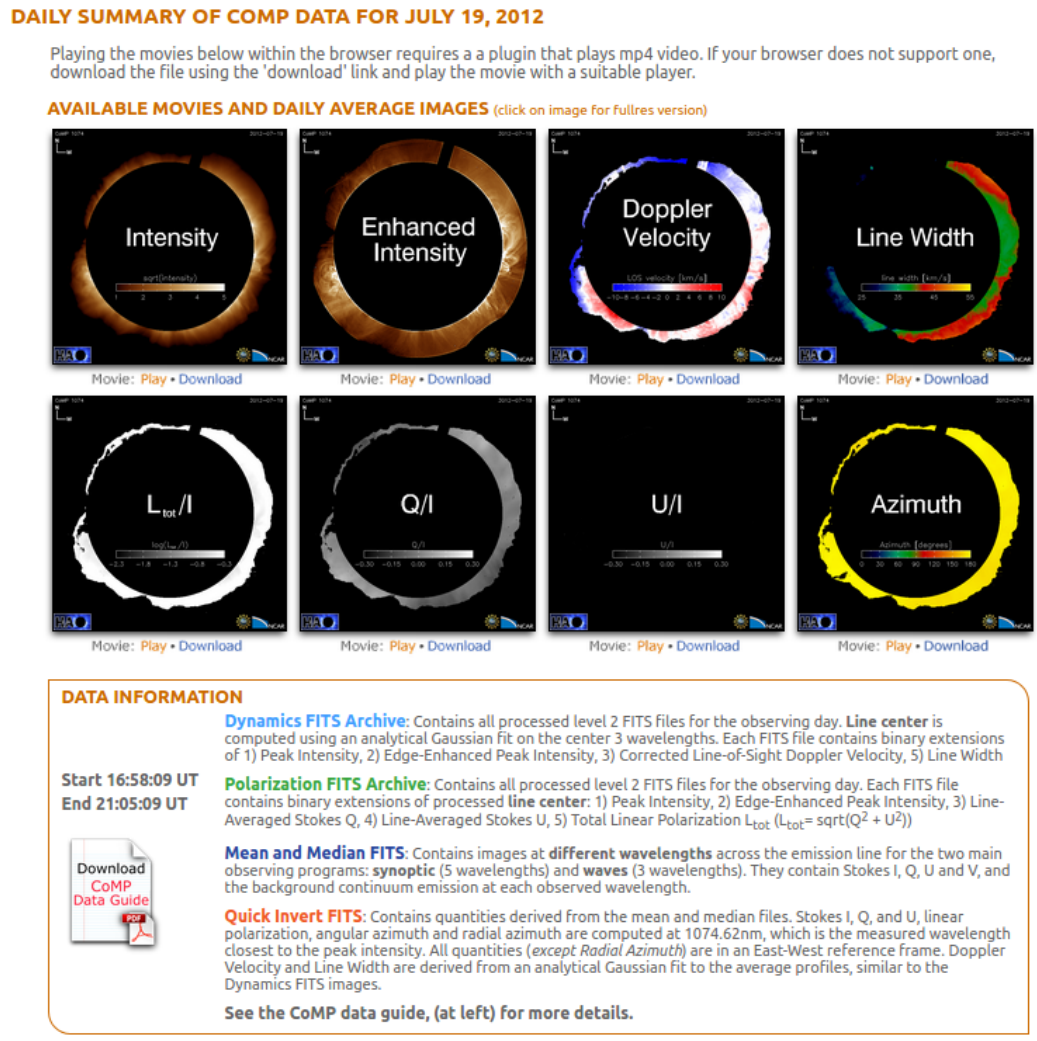

Fig. 2.2 Sample data products available from COMP instrument webpage. Credit: MLSO CoMP website.

applied to the Doppler velocity cubes as well. The results of the cross-correlation are such that the residual motions of the co-aligned cubes are less than 0.1 pixels.

2.2.2 Solar and Heliospheric Observatory

The Solar and Heliospheric Observatory (SOHO) is the only solar mission to have seen the full magnetic cycle of the Sun (22 years). This was launched in December 1995 (Domingo et al., 1995). It continues to provide solar physicists with various data products until today. SOHO has been the centre of several discoveries in its lifetime so far including, but not limited to 1) first images of the convection zone of a star, 2) measuring acceleration of slow and fast solar wind, 3) Identifying sources of the fast solar wind, 3) discovery of coronal waves and solar tornadoes. SOHO has also been particularly outstanding in discovering comets. SOHO comprises of 12 scientific payloads, each with a focus on different aspects of the solar observations. The Ultra-Violet (UV) Imager, Extreme ultraviolet Imaging Telescope (EIT) is used

in the study. EIT is capable of providing full disc images at four different wavelength bands in the extreme ultraviolet range. The wavelengths are 171, 195, 284, and 304 Å, corresponding to emission from highly ionized iron (Fe XI)/(Fe X), (Fe XII), (Fe XV), and helium (He II), respectively. This corresponds to plasmas of temperatures of 80000 K (corresponding to the transition region and the He II line) and 2 million K, in the low corona and transition region. Coronal EUV images from SOHO are used as the background images for the CoMP data during studies where there were no SDO data available.

2.2.3 Solar Dynamics Observatory

Solar Dynamics Observatory (SDO) is a more recent space-based solar observatory, launched by National Aeronautics and Space Administration (NASA Pesnell et al. 2012). It is a replacement for the earlier SOHO mission (2.2.2). It was launched in 2010, with a large volume of data generated by its instruments, it has put us in an abundance of high-resolution data to analyse. The spacecraft comprises of three instruments: the *Extreme Ultraviolet Variability Experiment* (EVE Woods et al. 2012):, the *Helioseismic and Magnetic Imager* (HMI Schou et al. 2012): measuring LOS velocities, LOS and Vector magnetic field of the photosphere, and the *Atmospheric Imaging Assembly* (AIA Lemen et al. 2012; an image of the Sun in multiple wavelengths of AIA is shown in Fig 2.3): which is a multi-wavelength instrument, drawing upon the legacy of SOHO (see Section 2.2.2). It captures the full disk images of the Sun in high resolution across multiple channels with a high temporal cadence of up to 12 sec.

2.3 Analysis techniques

After the crucial process of data acquisition in a scientific usable format, the data can be analysed. The analysis method very much depend on the scientific question being asked. This section focuses on the various well established and regularly used tools in the astronomical and solar physics community such as Fourier analysis, Maximum Likelihood Estimation (MLE) and Potential Field Source Surface (PFSS) extrapolation. These methods are used for specific analysis done in the successive chapters.

2.3.1 Fourier analysis

Fourier Transform

The Fourier transform is one of a class of integral transforms which converts a function from one form to another. The Fourier transform is a reversible, linear

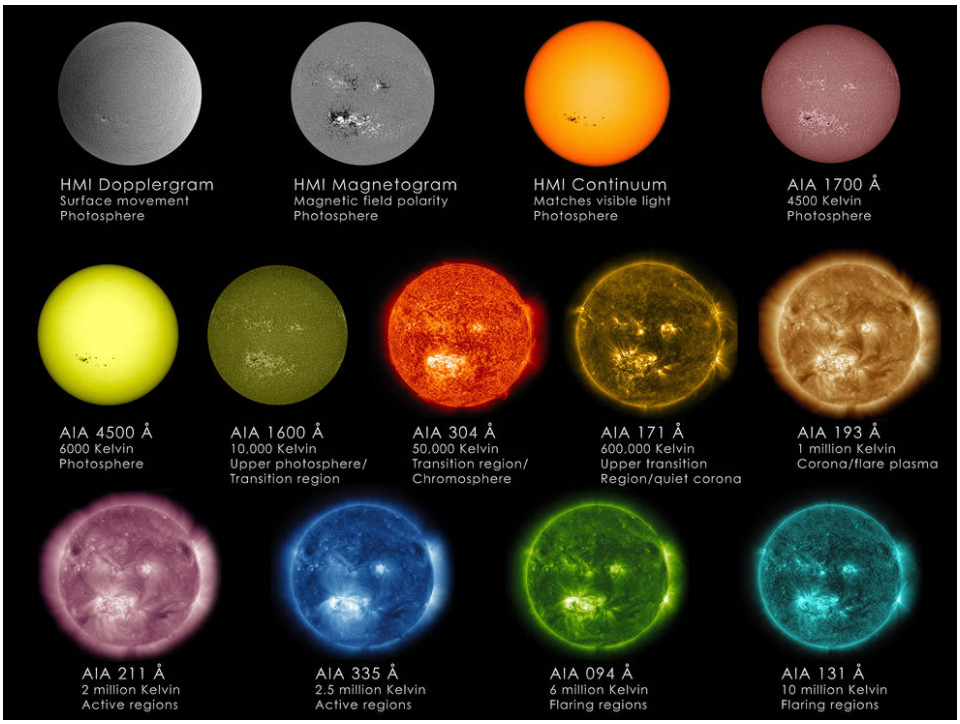

Fig. 2.3 Sun in the different wavelengths of the AIA instrument on board SDO. Image credit: NASA/SDO/GSFC

transform with several key properties, originally developed by Gauss and then later reintroduced by Cooley & Tukey (1965). The Fourier transform of the function $f(x)$ is then defined as $F(k)$,

$$F(k) = \int_{-\infty}^{\infty} f(x) \exp(-ikx) dx,$$

such that the inverse Fourier transformation is given by $f(x)$,

$$f(x) = \int_{-\infty}^{\infty} F(k) \exp(ikx) dk,$$

where $k = \frac{2\pi}{x}$ is called the wavenumber.

The Fourier transform of a function is a complex value function.

Fourier properties

Linearity

$$F(k) = \alpha G(k) + \beta H(k),$$

where

$$f(x) = \alpha g(x) + \beta h(x).$$

Translation

For a real x_0, $h(x) = f(x - x_0)$, the Fourier transform is given by

$$H(k) = exp(-iwx_0)F(k),$$

where, $F(k)$ is the Fourier transform of the function $f(x)$.

Modulation

For a real number k_0,

$$H(k) = F(k - k_0),$$

Scaling

For any real number $a \neq 0$, $h(x) = f(ax)$, the Fourier transform is such that,

$$H(w) = \frac{1}{|a|}F(w/a).$$

Differentiation

For the derivative of a function $h(x) = \frac{d^n}{dx^n}f(x)$, the Fourier transform is

$$H(w) = (iw)^n F(w).$$

Convolution

The convolution of two functions $f(x)$ and $g(x)$ is defined as,

$$f(x) \circledast g(x) \equiv \int_{-\infty}^{\infty} f(x-y)g(y)dy,$$

The Fourier transform of the convolved function $h(x) = f(x) \circledast g(x)$ is given by, $H(k) = F(w)G(w)$, or simply the product of the transformed functions.

Continuous and Discrete transformations

The equations for the Fourier transformations are so far about the continuous functions in time $f(t)$. In real world when dealing with data the time series that is obtained is a discrete time series $f(t_i)$. The integral sign is replaced with a discrete summation to get the Fourier transformation of discrete time series. This is called the Discrete Fourier Transform (DFT).

$$X_k = \sum_{j=0}^{N-1} f(t_j)exp(-i2\pi\nu_k t_j \Delta t),$$

where k identifies the complex discrete Fourier coefficient, X_k, while the index j is the summation over the waveform spaced at a distant Δt. The nature of the Nyquist criterion, limits the information on frequencies up to $\nu_s/2$. The smallest frequency that can be resolved is given by, $\Delta\nu = \nu_s/N$.

Fast Fourier Transform (FFT)

Fast Fourier transform is one of the most widely used algorithms in data analysis of time series. It unites several seemingly different disciplines. Several fields such as mathematics, engineering, and the physical sciences use and rely on the continuous Fourier transform. DFT is calculated by the so-called fast Fourier transform (FFT). The use of FFT to calculate DFT has revolutionized modern science and engineering, as it has become a ubiquitous algorithm in digital electronics and signal processing, thus transforming the society as well. It can decompose a signal (assumed to be periodic) into the constituent frequencies. The FFT is a specific algorithm for computing a DFT which uses certain symmetries in the problem to speed up the execution time to at most $(N \ln N)$.

Nyquist Frequency

The discretisation of the continuous Fourier transform gives rise to the Nyquist frequency. It is always assumed that the sampling is done at a constant rate $\nu_s = \frac{1}{\Delta_t}$. ν_s is called the sampling frequency. The Nyquist-Shannon sampling theorem states that the fastest real signal that can theoretically be reconstructed accurately is given by the Nyquist (or the critical) frequency which is given by $\nu_c = \nu_s/2$. This is the motivation behind the audio CDs being encoded at a bit rate of 44 kHz. To accurately reproduce sounds through the range of human hearing (up to 20 kHz) a Nyquist frequency which is slightly above 20 kHz is needed, which leads to sampling frequency at twice the Nyquist or critical frequency (44 kHz).

Aliasing

One of the interesting (and potentially a pitfall) arises from undersampling of a signal. If a signal is sampled at a frequency which violates the Nyquist condition $\nu_c > \nu_s/2$. An intuitive example of this is sampling a sinusoidal signal at a sampling frequency slightly below the actual signal frequency. If the frequencies were the same, the sampling frequency would always pick a point of constant phase with respect to the signal, and the result would be a constant value every time. If the sampling frequency is slightly less than the signal by an amount $\Delta\nu$, the sample picks a point on the signal waveform with a phase shift $\Delta\phi = 2\pi\Delta\nu\Delta t = 2\pi(\nu_s - \nu)/\nu_s$. The resultant sampled waveform is a slowly varying function as each successive sample picks a point shifted by $\Delta\phi$ which has an apparent frequency $(\nu_s - \nu)$ instead

of actual frequency (ν). In the limit of $\nu \to \nu_s$, the sampled signal does not show any oscillation. This effect is called *aliasing*. It is impossible to distinguish between an accurate measurement of a frequency and an aliased measurement of a higher frequency below the Nyquist frequency, with any discretely sampled data.

Leakage

For a discrete set of time (discretised into N temporal points) the function $f(t_i)$ is defined, but outside that range, no information is available about the function. A finite sampling of a continuous function, then, looks to the FFT operation like a continuous function multiplied by a square rectangle such that outside the sampling window the function is zero. The fact is that all observations of a signal (time series) are always sampled in a finite window. This introduces higher-order harmonics into the observed sample. The observation always has some finite window applied to it and the edges of the window are very sharp and lead to lots of higher-order frequency terms. This general feature is called *frequency leakage*.

Windowing

The total amplitude of a signal remains constant, but because of frequency leakage, this amplitude gets split amongst all of the frequency components. This results in the apparent height of the central "spike" (in the spectrum) vary up and down as the signal frequency moves around. The width of the spike varies similarly, making it difficult to use the FFT to measure either amplitude or width of a signal. This results from the implicit assumption of the DFT, namely, the signal is periodic, i.e. that the time series of length N repeats itself infinitely in a cyclic manner gives rise to an interesting problem when using FFT for analysis of a time-series data. If a stretch of length N is taken out of a time series containing a sinusoidal signal at random and an FFT is performed, the sinusoidal signal which is naively expected to result in a sharp peak in only one frequency bin instead shows as a distribution of various periodicities. If the frequency of the sinusoidal input signal is not an exact multiple of the frequency resolution f_{res}, i.e. does not fall in the exact centre of a frequency bin, this assumption is not true, and the DFT 'sees' a discontinuity between the last sample and the first sample due to the cyclic continuation. That discontinuity spreads power all across the spectrum. One solution is to convolve the time series with a 'windowing function' in the time domain before applying the DFT. This window function starts near or at zero, then increases to a maximum at the centre of the time series and decreases again. Thus the discontinuity is removed. Many window functions have been defined and given names such as Hamming, Hanning, and Gaussian. The selection of a window function involves some compromise between the width of the resulting peak in the frequency domain, the amplitude accuracy and

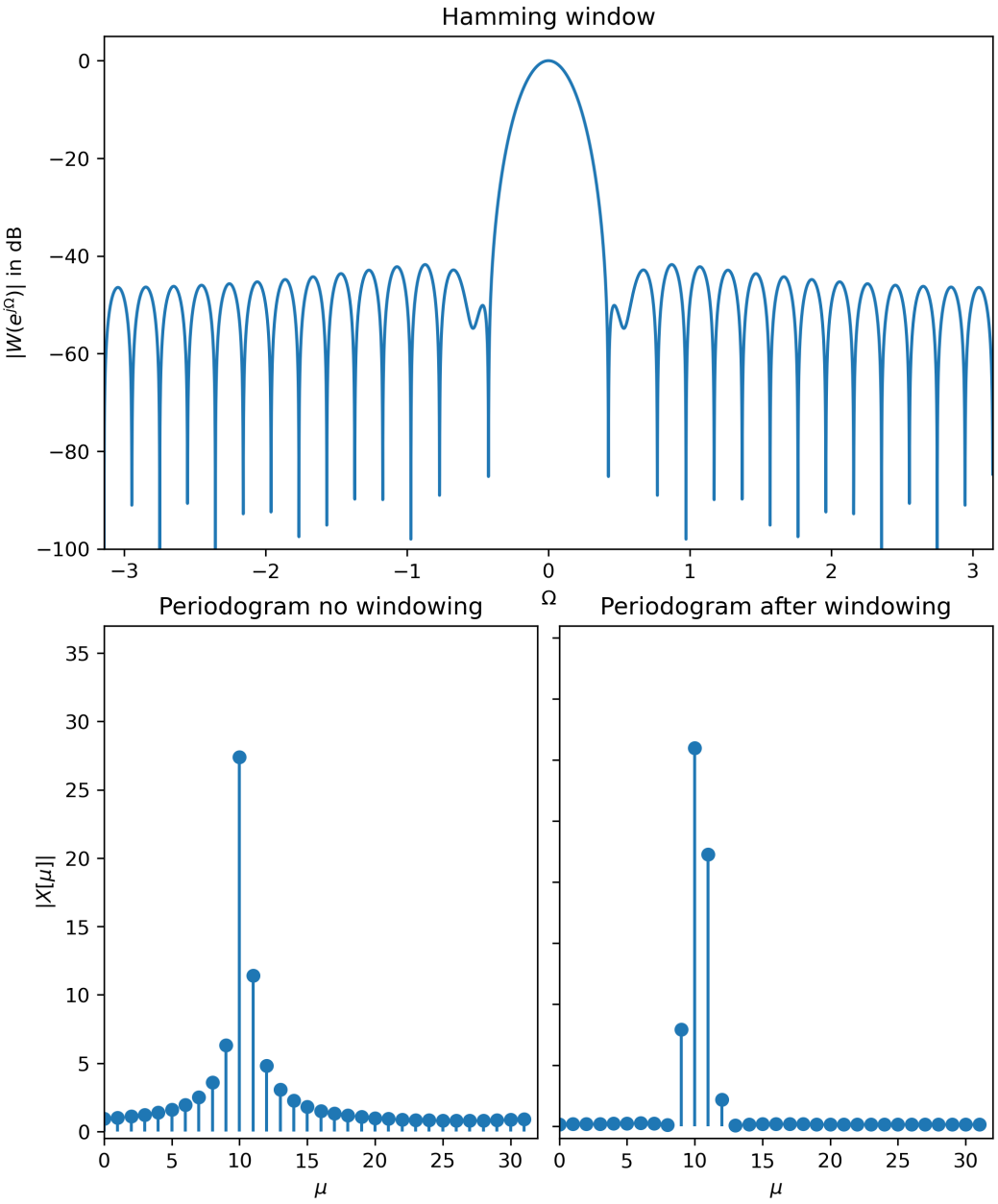

Fig. 2.4 An example of spectral leakage and application of windowing to find periodicities in the signal. *Top:* Hamming window function. *Right:* Absolute value of the DFT after windowing showcasing the advantages of using the Hamming window. *Left:* Absolute value of the DFT without windowing showcasing spectral leakage and difficulty in identifying periods that are close..

the rate of decrease of the spectral leakage into other frequency bins. The Hamming window is probably the best general-purpose window for finding specific frequencies, as it gives a nice sharp spike without too much leakage.

FFT example:

To showcase the effect of spectral leakage a sample signal with the superposition of two exponential signals with different amplitudes and frequencies is considered,

$$x_N[k] = A_1 \cdot e^{j\Omega_1 k} + A_2 \cdot e^{j\Omega_2 k} \tag{2.5}$$

where $A_1, A_2 \in \mathbb{R}$. In 2.4 the left panel shows the the magnitude spectrum of $x_N[k]$ for the signal with close frequencies ($\Omega_1 = 10.3, \Omega_2 = 10.9$) without applying the Hamming window (shown in top panel of 2.4), the right panel shows the magnitude spectrum for the same function with the window applied before takingf the FFT. Form the figures it is evident that the leakage effect limits the spectral resolution of the DFT.

Power spectrum

The power spectrum is a plot of the power of a time series as a function of the frequency. This is given by the absolute value of the Fourier transform ($F(w)$). The power spectrum ($|F(w)|^2$) calculated in this way as the *periodogram*. The periodogram are often averaged, which, introduces changes into the statistics of the periodogram (Appourchaux, 2003; Vaughan, 2005; Barret & Vaughan, 2012). The measured power spectra, $I(f_i)$ at each frequency ordinate, $f_i; i = 0, 1, 2, 3, ..., n$, from the DFT are distributed about the true power value, $P(f_i)$ as

$$I(f_i) = P(f_i)\frac{\chi_2^2}{2}. \tag{2.6}$$

Here χ_2^2 represents a random variable from the chi(χ)-squared distribution with two degrees of freedom, distributed as

$$\chi_2^2 = \frac{1}{2}\exp\left(-\frac{x}{2}\right). \tag{2.7}$$

By averaging M periodograms that average follows a χ_{2M}^2 distribution, this needs to be considered when trying to fit the power spectra.

2.3.2 Maximum likelihood estimation

Parameter estimation is one of the most fundamental tasks in data analysis. The data that is obtained lacks information about the distribution and the parameters of the distribution are also unknown. There are several methods of parameter estimation two of the most commonly used are: least-squares estimation (LSE) and Maximum Likelihood Estimation (MLE). The method of least squares is about estimating parameters by minimizing the squared discrepancies between observed data, on the

one hand, and their expected values on the other. LSE assumes that the data has normally distributed noise, which is not true for all observations. χ^2-minimisation is a measure of the mean squared deviations between the model and the data. It is used as a goodness of fit test. Recently there have been several studies which point towards the large biases that occur in the standard χ^2-minimisation (Mighell, 1999; Bergmann & Riisager, 2002; Fowler, 2014) in case of LSE. LSE is equal to the MLE parameter estimates if the data to be fitted is normally distributed. MLE was developed by R.A.Fisher in the early 1900s. Once there is a model and the data is collected, it is needed to validate the model. The first step is finding the best model parameters, given the data. The second step is evaluating the goodness of fit. To quote Fisher; 'the desired probability distribution is the one that makes the observed data "most likely," which means that one must seek the value of the parameter vector that maximizes the likelihood function $L(w|y)$'. MLE has several useful advantages over LSE in the estimation, namely

- Sufficiency: It provides complete information about the parameter of interest contained in its MLE estimator.
- Consistency: A true parameter value that generated the data is recovered asymptotically, for data of sufficiently large samples.
- Efficiency: The lowest-possible variance of parameter estimates is achieved asymptotically.
- Parameterization invariance: Same MLE solution is obtained irrespective of the parametrization used.

The basic steps of MLE can be described as follows (Myung, 2003):

- Model specification: Obtain the probability density function.
- Find the likelihood function, which represents the likelihood of the parameter given the observed data.
- Solve the likelihood equation to find local maxima.
- The parameters that lie in the local maxima are the MLE fit parameters.

These steps are illustrated using an example where the parameters for a normal distribution are estimated using an MLE approach.

Model Specification

Let us assume there is some data and the problem is to find the mean and standard deviation of the data. The data is believed to be normally distributed about its

true value. Hence, the normal distribution $N(\mu,\sigma)$ is chosen as the model. The probability density function for the normal distribution is given by,

$$Pr(x|\theta) = \frac{1}{\sigma\sqrt{2\pi}} e^{-\frac{(x-\mu)^2}{2\sigma^2}}. \tag{2.8}$$

Here, θ is a vector with two values, the first is the mean (μ) parameter (θ_0). The second is the variance (σ^2) parameter (θ_1). The probability of drawing value x_i from the distribution $f(x|\theta)$ is $f(x_i|\theta)$.

Likelihood function

The N samples are drawn from this distribution which are N independent and identically distributed ($i.i.d$), thus the likelihood function can be written as the product of individual likelihoods. The likelihood function of these N draws $(x_1,x_2,...x_N)$ from a model or distribution $f(x|\theta)$ as $\mathscr{L}$.

$$\mathscr{L}(x_1,x_2,...x_N|\theta) \equiv \prod_{i=1}^{N} f(x_i|\theta), \tag{2.9}$$

which in this case becomes,

$$\mathscr{L}(x_1,x_2,...x_N|\theta) = \prod_{i=1}^{N} \frac{1}{\sqrt{2\pi\theta_1}} \exp -\frac{(x_i-\theta_0)^2}{2\theta_1}. \tag{2.10}$$

Numerically it is sometimes difficult to maximise a product of small numbers, it is recommended to use the log of the likelihood function (log-likelihood function) $\ln(\mathscr{L})$.

$$\ln\Big(\mathscr{L}(x_1,x_2,...x_N|\theta)\Big) \equiv \sum_{i=1}^{N} \ln\Big(f(x_i|\theta)\Big), \tag{2.11}$$

following which the log likelihood for the normal distribution $N(\mu,\sigma)$ becomes,

$$\ln\Big(\mathscr{L}(x_1,x_2,...x_N|\theta)\Big) = \sum_{i=1}^{N} \ln\left(\frac{1}{\sqrt{2\pi\theta_1}} \exp -\frac{(x_i-\theta_0)^2}{2\theta_1}\right) = \sum_{i=1}^{N} \left[-\ln\sqrt{2\pi\theta_1} - \frac{1}{2\theta_1}(x_i-\theta_0)^2\right] \tag{2.12}$$

Likelihood equation to find maxima

The maximum likelihood estimate $\hat{\theta}_{MLE}$ is the following:

$$\hat{\theta}_{MLE} = \theta: \quad \max_{\theta} \ln\mathscr{L} = \max_{\theta} \sum_{i=1}^{N} \ln\Big(f(x_i|\theta)\Big). \tag{2.13}$$

This equation can be solved using partial derivative with respect to parameters θ_0 and θ_1, setting both the equations to 0 and solve for the values of θ.

$$\frac{\partial \ln \mathscr{L}(x|\theta)}{\partial \theta_i} = 0. \tag{2.14}$$

This equation represents a necessary condition for the existence of an MLE estimate. For the existence of maxima another condition needs to be satisfied.

$$\frac{\partial^2 \ln \mathscr{L}(x|\theta)}{\partial^2 \theta_i} < 0, \tag{2.15}$$

in computation this is computed using a *Hessian Matrix* ($\mathscr{H}$).

$$\mathscr{H}(x|\theta) = \frac{\partial^2 \ln \mathscr{L}(x|\theta)}{\partial^2 \theta_i} \tag{2.16}$$

The expected value of *Hessian* ($\mathscr{H}$) defines the *Fisher Information Matrix* ($\mathscr{F}$). The associated confidence intervals on the model parameters can be estimated by using the $\mathscr{F}_{ij}$.

$$\mathscr{F}_{ij} = \left\langle -\frac{\partial^2 \ln \mathscr{L}}{\partial \theta_i \partial \theta_j} \right\rangle, \tag{2.17}$$

where θ represents the model parameters (Pawitan, 2001; Bevington & Robinson, 2003). The *Fisher matrix* is a $N \times N$ matrix for N model parameters. The variance-covariance matrix is calculated using the inverse of the *Fisher Information Matrix*. **Cramer-Rao Theorem**, shows that the variation of any unbiased estimator of a parameter θ must be at least as large as the inverse of the expectation value of the *Hessian Matrix*.

$$var(\theta) \geq -\langle \mathscr{H}(\theta) \rangle^{-1}, \tag{2.18}$$

which means that any unbiased estimator that achieves this lower bound is efficient and no better-unbiased estimator is possible. The variance-covariance matrix by definition meets the criteria of the Cramer-Rao theorem. Thus, proving MLE to be efficient.

The curvature of the likelihood function indicates the level of certainty about the estimates of the parameters. The more curved the likelihood function is the more certain about the estimation of the parameter. The second derivative of the likelihood function is a measure of the curvature. Intuitively this shows that the standard errors are linked to the curvature of the likelihood function. The diagonal elements of the variance-covariance matrix give the standard error squared on each model parameter, σ^2. The off-diagonal matrix elements provide the covariances between parameters. The *Fisher Matrix* only gives reliable uncertainties when the likelihood surface can be approximated by a multi-dimensional Gaussian. When linkelihood function is evaluated for each point in the parameter space, a likelihood surface is obtained. The confidence limits on the MLEs can also be calculated from $\Delta S = S(\theta) - S(\hat{\theta})$ in

the same manner $\Delta\chi^2$ method, where $S \equiv -2\ln\mathscr{L}$ (Bevington & Robinson, 2003). $\Delta S = 1$ corresponds to the 68.3 % confidence limits on one parameter (Vaughan, 2005; Barret & Vaughan, 2012, see discussion). The Fisher matrix method is fast but is reliable only when the likelihood surface is Gaussian; the ΔS method is slower but gives reasonable confidence intervals even for non-Gaussian likelihoods and can even be used to search for local minima. The standard methods of calculating the confidence intervals can be used after the *Fisher matrix* has been calculated, such as; Wilks confidence intervals (Bevington & Robinson, 2003) or point-wise Wald 95% confidence intervals (Bevington & Robinson, 2003) for the model.

Finding parameters

The parameters after the maximising the log-likelihood functions for this example are

$$\hat{\mu} = \frac{1}{N}\sum_{i=1}^{N} x_i,$$

and,

$$\hat{\sigma^2} = \frac{1}{N}\sum_{i=1}^{N}(x_i - \hat{\mu})^2.$$

This is the expected value of mean and variance of a normal distribution. In practice, however, it is usually not possible to obtain an analytic form solution for the MLE estimate, especially when the model has multiple parameters and/or if the PDF is highly nonlinear. In such situations, the MLE estimate must be sought numerically using non-linear optimization algorithms. The basic idea of nonlinear optimization is to quickly find optimal parameters that maximize the log-likelihood. This is achieved by searching much smaller subsets of the multidimensional parameter space rather than exhaustively searching the whole parameter space. Searching the parameter space becomes increasingly computationally expensive as the number of parameters increases. The “intelligent” search proceeds by trial and error over the course of a series of iterative steps. Specifically, on each iteration, by taking into account the results from the previous iteration, a new set of parameter values is obtained by adding small changes to the previous parameters in such a way that the new parameters are likely to lead to improved performance. Different optimization algorithms differ in how this updating routine is conducted. The iterative process continues until the parameters are judged to have converged on the optimal set of parameters or an appropriately predefined criterion. The stopping criterion can be the maximum number of iterations allowed or the minimum amount of change in parameter values between two successive iterations.

2.3.3 PFSS modelling

Solar observations pose a unique set of remote sensing problems as gathering the data in-situ is not possible. The magnetic properties of coronal loops is studied by extrapolating the magnetic field from photospheric magnetic field (magnetograms) observations and comparing the result to loop observations. The static solution can be obtained by balancing the forces in the coronal loops, gas pressure, gravity and magnetic forces

$$\sum \vec{F} = -\nabla P + \vec{j} \times \vec{B} + \rho \vec{g} = 0 \tag{2.19}$$

Additionally, the “force-free" approximation is used, where each force is assumed to be negligible. In case of coronal loops the gravitational force and the pressure gradient are negligible, the Lorentz force dominates over the other forces,

$$0 \quad = \quad \vec{j} \times \vec{B} \tag{2.20}$$

Only two solutions to this equation are either $\vec{j} = 0$ or $\vec{j}$ is parallel to the $\vec{B}$. In the case of, $\vec{j} = 0$,

$$\nabla \times \vec{B} = 0\,, \tag{2.21}$$

is obtained. This is the called the current-free solution and results in “potential fields". The curl and divergence of which are zero. In the case of latter the currents are aligned with the magnetic field,

$$\nabla \times \vec{B} \quad = \quad \mu_0 j \hat{\mathbf{B}} = \alpha B \hat{\mathbf{B}}\,, \tag{2.22}$$

$$\nabla \times \vec{B} \quad = \quad \alpha \vec{B}\,, \tag{2.23}$$

where α is a scalar derived from Equation 2.22,

$$\alpha = \frac{j\mu_0}{B} \tag{2.24}$$

These fields can be “non-potential" and result in a twist in the field.

If α equal to zero is called the ‘potential’ case,

$$\nabla \times \vec{B} = 0\,, \tag{2.25}$$

and using vector algebra, $\vec{B}$ can be written as the gradient of some scalar potential field,

$$\vec{B} = \nabla \Psi \tag{2.26}$$

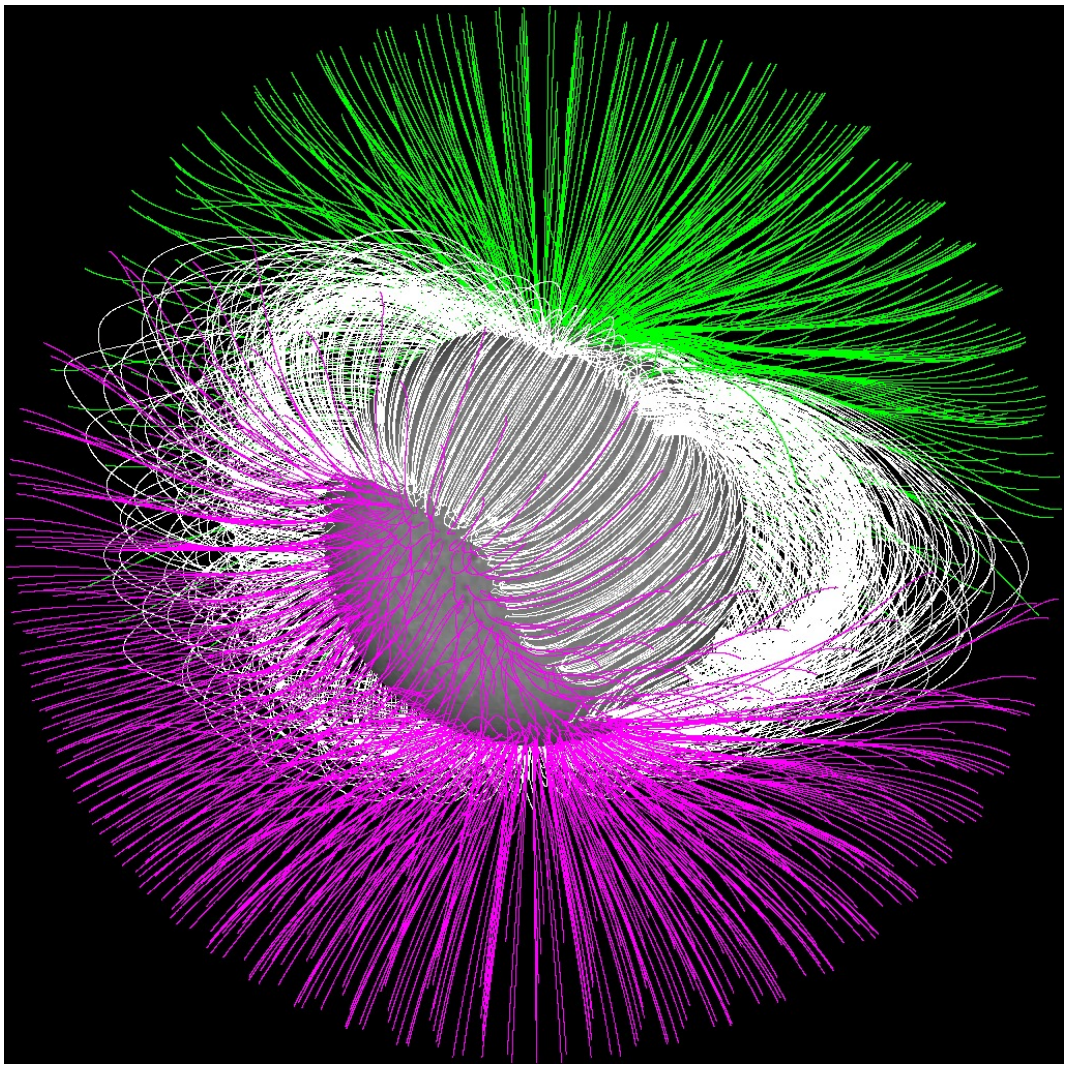

Fig. 2.5 An example of a 'Hairy Sun' image is shown. An example of a spherical PFSS extrapolation using MDI line-of-sight magnetogram as boundary layer (using PFSS pack in SSWIDL). Closed field lines are shown in black, positive and open in green and negative and open in magenta Image source.

One can also verify that the scalar field Ψ satisfies Laplace's equation (take divergence of both sides of Equation 2.26),

$$\nabla^2\Psi \;=\; 0 \tag{2.27}$$

A solution to Equation 2.27 in spherical coordinates is superposition of spherical harmonic series (Riesebieter & Neubauer, 1979; Rudenko, 2001),

$$\Psi(r,\theta,\phi) = \sum_{\ell,m}\left(A_\ell^m r^\ell + B_\ell^m r^{-(\ell+1)}\right) Y_\ell^m(\theta,\phi)\,, \tag{2.28}$$

where r is the radius from solar center, A_ℓ^m and B_ℓ^m are coefficients determining the significance of each harmonics, and $Y_\ell^m(\theta,\phi)$ are the pure harmonic modes. The subscripts m and ℓ define the number of sectors in the longitude ($n_\phi = m+1$) and

latitude ($n_\theta = \ell + 1$) direction, respectively. The spherical harmonics are given by,

$$Y_\ell^m(\theta,\phi) = \mathscr{C}_m^\ell P_m^\ell(\cos\theta) e^{im\phi}\,, \tag{2.29}$$

where $P_m^\ell(\cos\theta)$ are the Legendre polynomials and,

$$\mathscr{C}_m^\ell = (-1)^m \left[\frac{2\ell+1}{4\pi}\frac{(\ell-m)!}{\ell+m)!}\right]^{1/2} \tag{2.30}$$

The boundary conditions are specified such that at $r = R_\odot$, the magnetic field is determined by LOS magnetic field observations (HMI magnetograms) and an upper boundary is determined by an arbitrary "source surface" where the field becomes radial. Conventionally, this is usually $2.5R_\odot$. These conditions form a unique solution for the field with these initial conditions. The coefficients can be solved by substituting Equation 2.28 into Equation 2.26 and applying the boundary conditions; this is called Potential Field Source SUrface (PFSS) extrapolation. An example of a PFSS extrapolation for the whole Sun, using the SSWIDL package,[2] is shown in Figure 2.5.

2.3.4 Wave propagation angle determination

The CoMP Doppler velocity image sequences show coherent fluctuations propagating through the corona, which are interpreted as propagating kink waves after much debate in the community (for a discussion on interpretation see Van Doorsselaere et al., 2008). The initial step in the investigation is to determine the direction of the propagation of the observed waves. The coherence between the velocity time-series of each pixel and its neighbouring pixels is calculated using a Fast Fourier Transform (FFT, discussed in Section 2.3.1)-based method (McIntosh et al., 2008; Tomczyk & McIntosh, 2009) and correlation maps are derived. Selecting pixels in the neighbourhood where the coherence value is greater than 0.5 defines a coherence island, as shown in Figure 3.3. This coherence island has a distinct direction following the apparent trajectory of the propagating waves. The direction of wave propagation is then taken to be aligned with the island, determined by fitting a line that minimizes the sum of perpendicular distances from the points to the line. This is performed for each pixel in the field-of-view enabling us to create a wave-angle map, an example of which is displayed in the right panel of Figure 3.1. The shown angle gives the direction of propagation measured counterclockwise from a due East direction. Given that the kink mode propagates along the magnetic field, this angle should also represent the magnetic field orientation in the plane-of-sky (POS), and this method does indeed show excellent agreement with polarimetric

[2] From http://www.lmsal.com/~derosa/pfsspack/#usersguide.

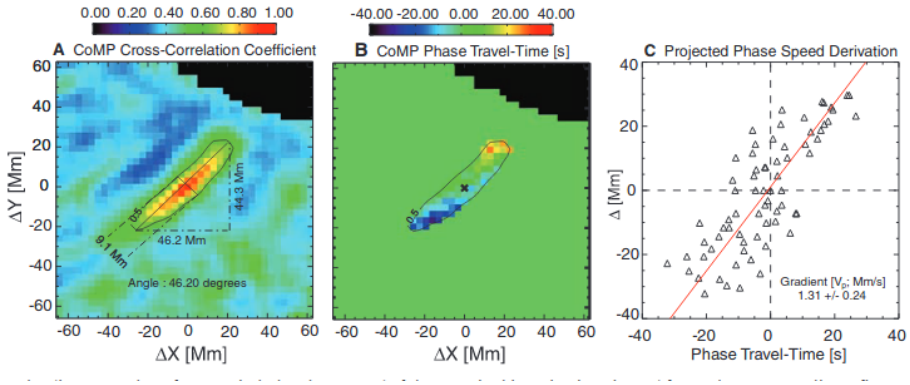

Fig. 2.6 (A) Coherence-island (B) Phase travel time calculation (C) Relationship between phase travel time and the distance to the reference pixel; the phase speed of the wave in this region is estimated from a least-squares linear fit. Image credit: (Tomczyk et al., 2007).

measurements of the POS orientation of the magnetic field (Tomczyk & McIntosh, 2009).

Chapter 3

Damping of Propagating Kink Waves in the Solar Corona[1]

[1]This chapter is based on Tiwari, A. K., Morton, R. J., Régnier, S., & McLaughlin, J. A. 2019, The Astrophysical Journal, 876, 106.

3.1 Introduction

Ubiquity of Magnetohydrodynamic (MHD) waves is already established in the solar corona. MHD waves are discussed in Section 1.6.There have been numerous observations of the different wave modes as the available instrumentation has become significantly sophisticated over the years as discussed in Chapter 2, offering higher spatial, spectral and temporal resolutions. To consolidate our understanding of these waves in the Sun, several reviews are available, for exhaustive information, (e.g. Nakariakov, 2003; Aschwanden, 2004; Nakariakov & Verwichte, 2005; Banerjee et al., 2007; Nakariakov et al., 2016b; Wang, 2016; Roberts, 2019; Van Doorsselaere et al., 2020).

Of all the different MHD wave modes proposed and observed, Alfvénic waves are considered one of the most elusive and important ones. They are also one of the promising candidates for explaining the solar coronal heating and solar wind acceleration. The term 'Alfvénic waves' should not be confused with 'Alfvén waves'. The former refers to MHD wave modes that share properties similar to the idealized Alfvén wave in a homogeneous plasma (the latter), namely *a.)* they are transverse,*b.)* highly incompressible, and *c.)* dominant restoring force is the magnetic tension (Goossens et al., 2009). The standing kink (transverse) waves were the first to be observed by the Transition Region And Coronal Explorer (TRACE Strong et al. 1994; Handy et al. 1999a). This observation was very exciting for solar observations as one could see the coronal loops, establishing the presence of standing kink waves and leading to the development of the field of coronal magneto-seismology. Since the TRACE observations there has been a constant coverage of the solar disc and corona and a number of similar events have been reported using the AIA/SDO. One of the prominent excitation mechanisms of these waves is understood to be low coronal eruptions (Zimovets & Nakariakov, 2015). The standing kink waves are rapidly damped, with periods of ≈ 4 minutes and damping times of ≈ 14 minutes (e.g. Aschwanden et al., 2002; Verwichte et al., 2013b; Goddard et al., 2016). There is an increasing body of evidence suggesting the damping mechanism of these waves to be mode coupling via resonant absorption. Resonant absorption is present in inhomogeneous plasmas, converting the energy in transverse motions to azimuthal motion via resonant coupling (e.g. Ruderman & Roberts, 2002; Goossens et al., 2002; Aschwanden et al., 2003). The propagating kink waves are fairly recent observations with not enough studies to understand the nature of these waves. The observations so far have already established the prevalence of these waves in the corona. The excitation mechanism(s) of the propagating kink waves are still not resolved with some studies suggesting the role of horizontal motions of magnetic elements in the photosphere (e.g. Cranmer & Van Ballegooijen, 2005; Van Ballegooijen et al., 2011; Pascoe et al., 2015; Jafarzadeh et al., 2017; Matsumoto & Shibata, 2010),

and others suggesting the role of p-modes (Tomczyk et al., 2007; Morton et al., 2016; Cally, 2017; Morton et al., 2019). Moreover, the origin of the low-frequency velocity fluctuations is still unclear. It was suggested by (Cranmer, 2018) that reconnection resulting from the evolution of the magnetic carpet may excite waves at such frequencies.

Tomczyk et al. (2007); McIntosh et al. (2011a); Tomczyk & McIntosh (2009); Thurgood et al. (2014); Morton et al. (2015) noted that the propagating kink modes observed in a quiet-sun coronal loop were damped, with Terradas et al. (2010) and Verth et al. (2010) suggesting that resonant absorption provides a reasonable description of the observed damping. The role of resonant damping of propagating transverse waves is substantiated in 3D, full MHD numerical simulations (e.g. Pascoe et al., 2010, 2012; Magyar & Van Doorsselaere, 2016; Pagano & De Moortel, 2017, 2019). The analytical framework of the resonant absorption is provided by (Terradas et al., 2010), which was used in the study by Verth et al. (2010).

The expression in Equation 1.34 provides the underlying model for further analysis of propagating kink waves. Utilizing data from CoMP enables us to provide estimates for: the values of the inward and outward power spectra as a function of frequency, the half-loop length and the propagation speed of the waves. This, in combination with Equation (1.34), provides us with a means to measure the quality factor (ξ) if $\langle P(f)\rangle_{ratio}$ is known.

To accurately measure the quality factor, the model in Equation (1.34) is fitted to the power ratio as a function of frequency, as undertaken in Verth et al. (2010). Verth et al. (2010) used the least-squares method to achieve this, which assumes that the individual ordinates of the power spectra ratio are normally distributed about their true value, which is shown to not be the case in Section 3.3.4. The statistics of the power spectrum obtained via the discrete Fourier transform (DFT) is well-studied (e.g. Jenkins & Watts, 1969; Groth, 1975; Geweke & Porter-Hudak, 1983; Appourchaux, 2003; Vaughan, 2005); where the ordinates are known to be distributed about the true values as χ^2 with ν degrees of freedom (ν depends on the number of power spectra averaged). Hence, it should not be expected that ordinates from the ratio of two power spectra are normally distributed. In this study the appropriate distribution for the ratio of two χ^2_ν distributed power spectra is derived, demonstrating that the assumption of normality, and therefore the utilization of the least-squares method, is inappropriate.

The chapter is structured as follows: Section 3.2 discusses details of the data used. The method of analysis is described in Section 3.3, where a discussion on the statistics of a power spectrum obtained from DFT and derive the applicable likelihood function required for the maximum likelihood estimation of model parameters

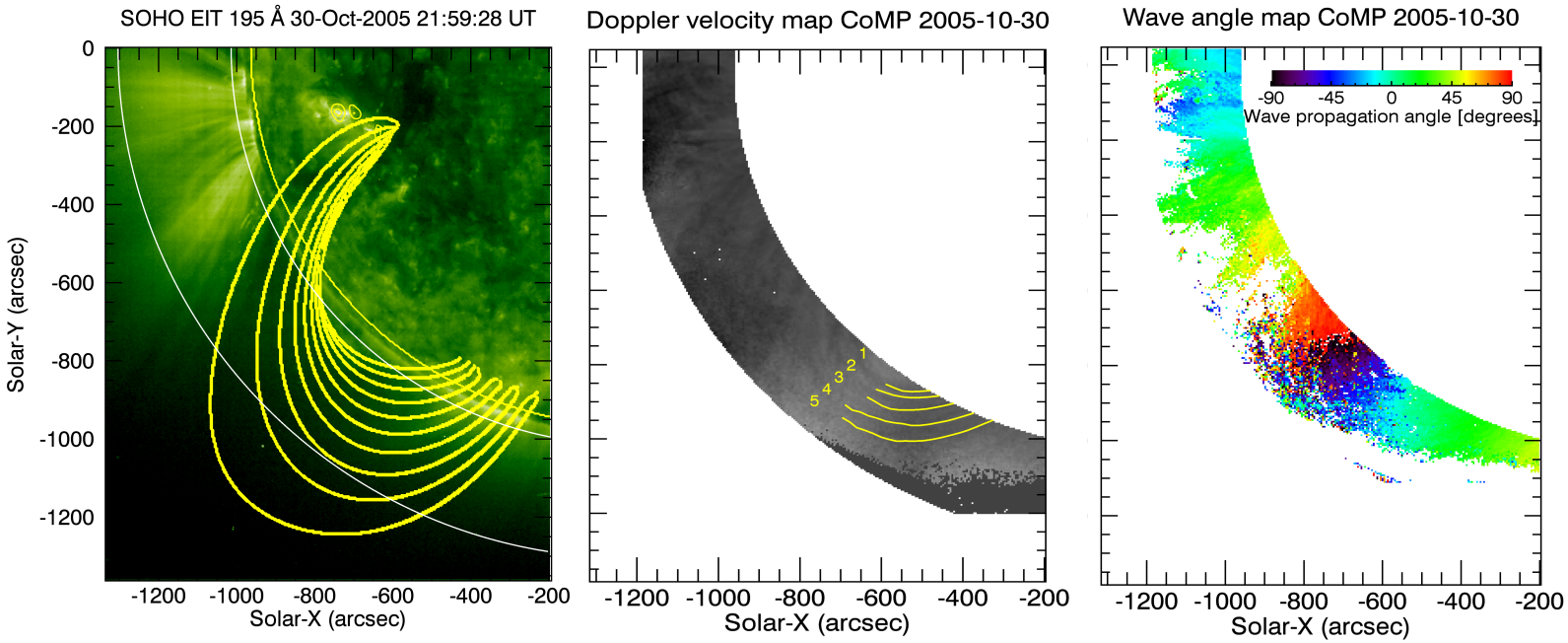

Fig. 3.1 *Left:* The PFSS extrapolated magnetic field lines. The field lines were then plotted over the corresponding SOHO/EIT 195 Å image. The curves in white corresponds to the field of view for CoMP for comparison. *Center:* A sample Doppler velocity image is displayed with the over-plotted wave propagation tracks selected for analysis (yellow). *Right:* The wave-angle map obtained from the coherence wave tracking method described in Section 3.3.2.

from the measured power ratio of damped propagating kink waves is provided. In Section 3.4, a discussion of the main findings are presented and a conclusion is given in Section 3.5. A modified model for future analysis of damping is also derived in Section 3.6.

3.2 Observation

The data were obtained using the Coronal Multi-channel Polarimeter (CoMP, discussed in Subsection 2.2.1) (Tomczyk et al., 2007, 2008). CoMP is a combination polarimeter and narrow-band tunable filter that can measure the complete polarization state in the vicinity of the 10747 Å and 10798 Å Fe XIII coronal emission lines. The data were taken on 30 October 2005, with a temporal cadence of 29s, and a pixel size of 4.5 arcsec/pixel. The spectroscopic data from the 10747 Å Fe XIII line, is chosen for this study. The same dataset has been previously used by Tomczyk et al. (2007) and Verth et al. (2010). The data set consists of Doppler velocity images of the corona between 1.05 $R_{\odot}$ and 1.35 $R_{\odot}$. An example image is shown in the centre panel of Figure 3.1. The study focuses on the same region studied previously in Tomczyk & McIntosh (2009) and Verth et al. (2010). These are quiescent off-limb coronal loops. To provide context images and magnetic field measurements, data from the Solar and Heliospheric Observatory (SOHO) (St. Cyr et al., 1995) is also utilized. Data from the Extreme Imaging Telescope (EIT) (Delaboudinière et al., 1995) provides a context to the loops observed using CoMP. The background image in the left panel of Figure 3.1 is obtained from EIT 195 Å passband. Line-of-sight (LOS) magnetograms from the Michelson Doppler Imager (MDI) instrument (Scherrer et al., 1995) provide information on the photospheric magnetic field for potential field extrapolations.

3.3 Analysis

3.3.1 Extrapolation of the loops

The extrapolation of loops were performed using the PFSS extrapolation method, as discussed in Subsection 2.3.3. It is important to understand the orientation of the loops before further analysis. To provide some insight, the potential field source surface (PFSS - Schrijver & DeRosa, 2003) extrapolation package available in SolarSoft (Freeland & Handy, 1998) is used to indicate the local magnetic field structure in the corona (Figure 3.1: left). To determine the validity of the obtained field extrapolations, several attempts to generate extrapolations in the neighbourhood

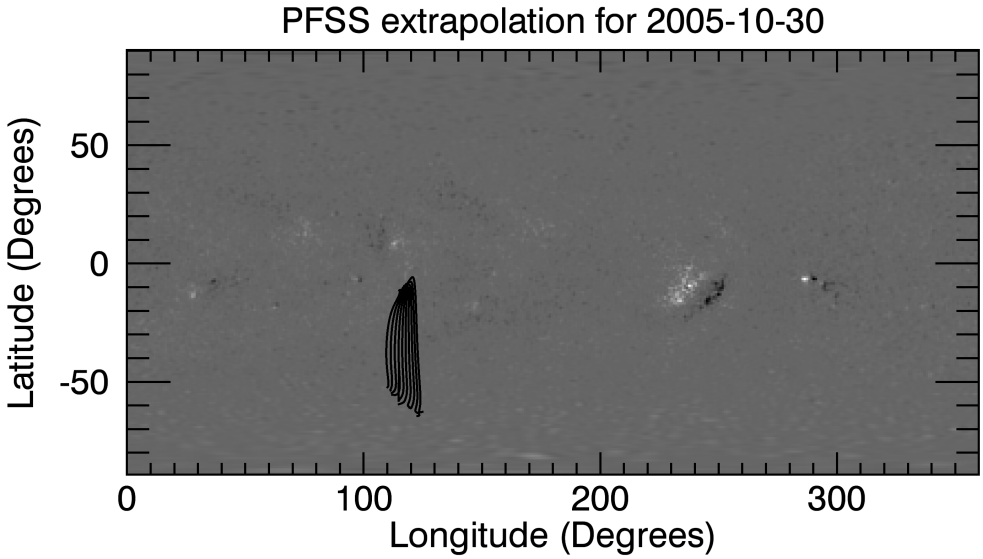

Fig. 3.2 PFSS extrapolated magnetic field lines following the coronal loops under investigation, tracked later using wave angles. The field lines are projected on the photospheric magnetogram (edge-on view).

of the footpoints are undertaken. The footpoints are chosen manually based on the location of the coronal loop bundles as seen in the Doppler velocity images obtained from CoMP. Repeating this process of tracing loops in the region of interest for the loops we are satisfied that these are the the best extrapolated loops. It is found that the given PFSS loops are indeed unique solutions for the extrapolations. Further extrapolations were undertaken to examine the solution for constant latitudinal points to ascertain that the loops obtained from the initial extrapolations are the most suitable representation for the observed CoMP loops. The extrapolated field lines obtained after these initial checks are shown (Figure 3.1: left) and visually represent the coronal structures well. There is also close agreement with the direction of wave propagation determined from CoMP, which is believed to follow the magnetic field lines (Figure 3.1 centre and right panels, see Section 3.3.2 for further details). The projection of the field lines onto the photospheric magnetogram is shown in Figure 3.2.

3.3.2 Wave propagation angle determination

The CoMP Doppler velocity image sequences show coherent fluctuations propagating through the corona, which are interpreted as propagating kink waves after much debate in the community (Van Doorsselaere et al., 2008, for a discussion on interpretation.). The initial step in the investigation is to determine the direction of the propagation of the observed waves. The coherence between the velocity time-series of each pixel and its neighbouring pixels is calculated using a Fast Fourier

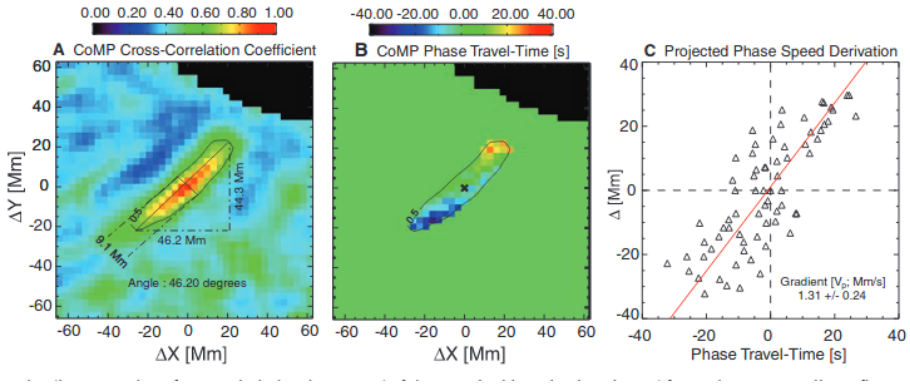

Fig. 3.3 (A) Coherence-island (B) Phase travel time calculation (C) Relationship between phase travel time and the distance to the reference pixel; the phase speed of the wave in this region is estimated from a least-squares linear fit. Image credit: (Tomczyk et al., 2007).

Transform (FFT, discussed in Section 2.3.1)-based method (McIntosh et al., 2008; Tomczyk & McIntosh, 2009) and correlation maps are derived. Selecting pixels in the neighbourhood where the coherence value is greater than 0.5 defines a coherence island, as shown in Figure 3.3. This coherence island has a distinct direction following the apparent trajectory of the propagating waves. The direction of wave propagation is then taken to be aligned with the island, determined by fitting a line that minimizes the sum of perpendicular distances from the points to the line. This is performed for each pixel in the field-of-view enabling us to create a wave-angle map, an example of which is displayed in the right panel of Figure 3.1. The shown angle gives the direction of propagation measured counterclockwise from a due East direction. Given that the kink mode propagates along the magnetic field, this angle should also represent the magnetic field orientation in the plane-of-sky (POS), and this method does indeed show excellent agreement with polarimetric measurements of the POS orientation of the magnetic field (Tomczyk & McIntosh, 2009).

3.3.3 Determining Wave Power

Calculating wave angle propagation at each pixel in the method described in Section 3.3.2. The image thus generated is called a wave-angle map. The wave-angle map is then used to determine the path of the wave propagation through the corona, enabling the kink wave packets to be followed and to determine how they evolve as they propagate. Five different wave paths with increasing lengths (centre panel of Figure 3.1) were identified for the study. The selected paths are assumed to follow the quiescent coronal loops and, to satisfy the restrictions of Eq. 1.34 assumed to represent half the total loop length (this assumption is discussed further in Section 3.4). The velocity signal along the wave paths is extracted to create time-distance maps, where cubic interpolation is used to map the velocities from the selected wave paths

onto (x,t) space[2] For each wave path is shown in Figure 3.1, five wave paths on either side of the original wave path are also extracted. Each additional path is calculated using the normal vector to the original, and are separated by one pixel in the perpendicular direction.

These velocity time-distance maps are composed of both the inward and outward propagating kink waves. Taking a Fourier transform of the velocity time-distance maps enables us to produce the $k-\omega$ spectra for velocity power, shown in Figure 3.4. The wave power is separated for the inward and outward components of the wave propagation, and it is evident from all $k-\omega$ spectra that the outward wave power dominates over the inward wave power. By taking the inverse Fourier transform of the inward and outward halves of the $k-\omega$ spectra separately (Tomczyk et al., 2007; Tomczyk & McIntosh, 2009; Morton et al., 2015), filtered time-distance diagrams are created. The filtered time-series are used to obtain the wave propagation speed along the wave path for both outward and inward propagating waves. The time-series at the centre of the wave path are cross-correlated to the neighbouring time-series along the path. The lag of the cross-correlation is determined by fitting a parabola to the peak of the correlation function. The propagation speed is then calculated by fitting the slope of the observed lags as a function of the position along the wave path.

Finally, the wave power as a function of frequency for the inward and outward components is calculated by summing the spectra in the k-direction. For each loop, the inward and outward spectra are averaged over the neighbouring wave paths to suppress the variability (see Section 3.3.4). From this one dimensional averaged wave power, the ratio of the outward and inward power, $\langle P(f)\rangle_{ratio}$, is determined. For each of the coronal loops studied, the ratio of power spectra displays an increase in magnitude as frequency increases (Figure 3.4). It is this signature that demonstrates the frequency dependence of the change in outward and inward power, indicating that a frequency-dependent process is in action to attenuate the waves, e.g., resonant absorption. These observations indicate low-frequency waves are more damped.

As discussed in the introduction, to estimate the quality factor from the obtained power ratio, the model power ratio given by Eq. (1.34) should be fit to the data in a robust manner. At this point the statistics of the power ratio must be discussed.

3.3.4 The Statistics of the Power Ratio

In Verth et al. (2010) the ratio of the outward and inward spectra was fitted with the model given by Equation (1.34) using a least-squares minimization. The assump-

[2]IT should be noted that due to the relatively coarse spatial resolution of CoMP, and because of the optical thin nature of coronal plasma, each wave path likely represents the integration over multiple individual loop structures (De Moortel & Pascoe, 2012; McIntosh & De Pontieu, 2012).

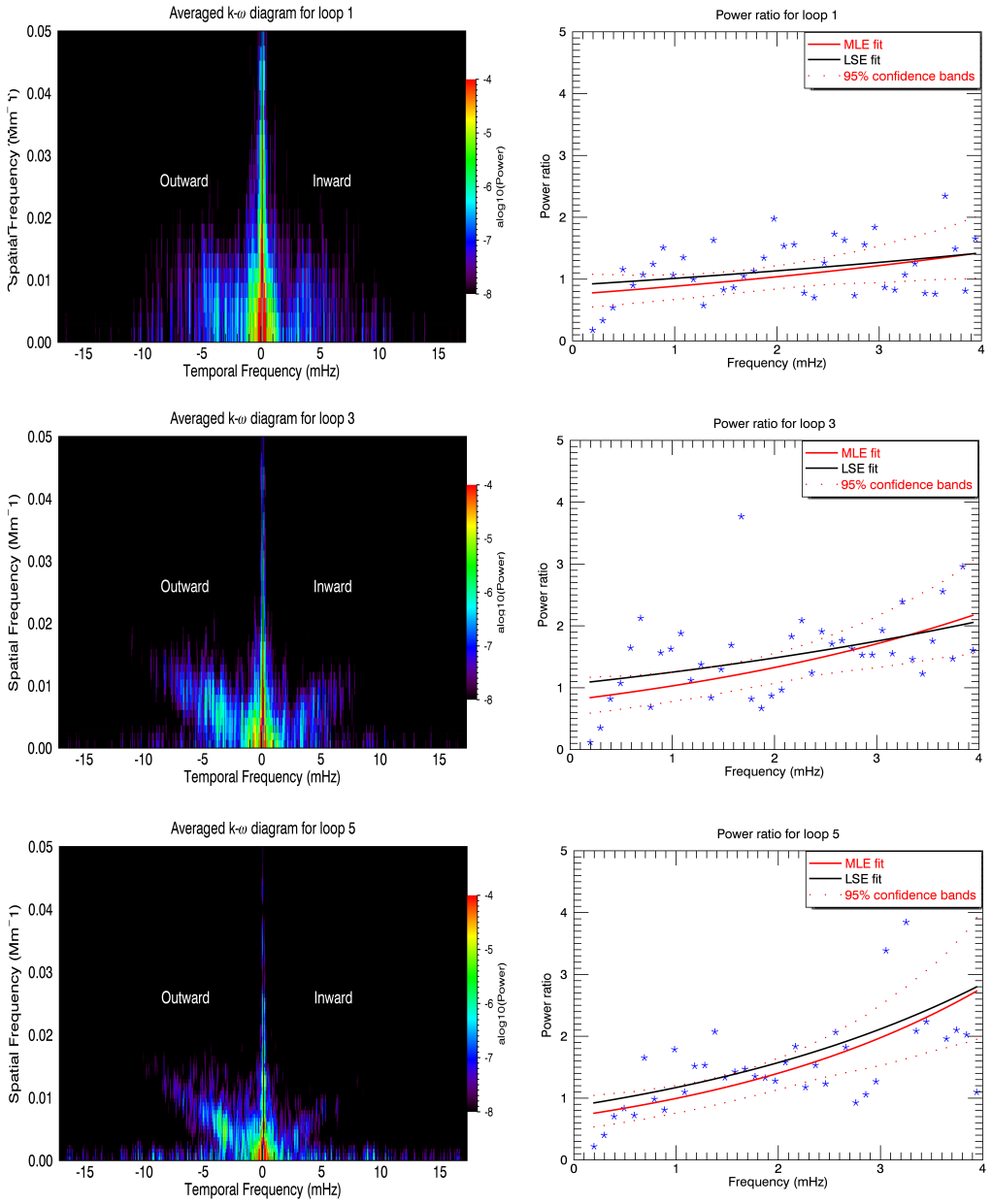

Fig. 3.4 Averaged $k-\omega$ diagrams for three selected tracks as shown in Figure 3.1(center). *Top* is 100 Mm; *Middle* is 326 Mm; *Bottom* is 552.6 Mm. The *left* column shows the averaged $k-\omega$ diagrams. The *right* column show the fitted power ratio. The measured power ratio for three coronal loops is shown here by the blue stars, for loops with increasing length. The results from the MLE fitting of the resonant absorption model are over-plotted (red solid), with point-wise Wald confidence bands shown at 95% (red dotted). As a comparison, the results of the model fit using least-squares (black) is also shown (solid black).

tion that the power ratio values at each frequency ordinate are normally distributed (implicit in least-squares) is not appropriate and leads to a poor estimate of model parameters and their uncertainties. This study presents a new method for the maximum likelihood estimation of model parameters from the ratio of two power spectra obtained via a discrete Fourier transform (DFT).

The power spectra, $I(f_i)$ at each frequency ordinate, $f_i; i = 0,1,2,3,...,n$, from the DFT are distributed about the true power value, $P(f_i)$ as

$$I(f_i) = P(f_i)\frac{\chi_2^2}{2}. \tag{3.1}$$

Here χ_2^2 represents a random variable from the chi(χ)-squared distribution with two degrees of freedom, distributed as

$$\chi_2^2 = \frac{1}{2}\exp\left(-\frac{x}{2}\right) \tag{3.2}$$

(see e.g., Vaughan, 2005). If the ratio of the values x and y, drawn from two independent χ_2^2 distributions X and Y is taken, the associated probability distribution function (PDF) is $Z = X/Y$ and the distribution of Z is then given by

$$\psi_z = \int_0^\infty y\psi_{xy}(zy,y)dy. \tag{3.3}$$

Given that x and y are independent, ψ_{xy} is given by

$$\psi_{xy} = \frac{1}{4}\exp\left(-\frac{x+y}{2}\right). \tag{3.4}$$

Hence,

$$\psi_z = \frac{1}{(1+z)^2}, \tag{3.5}$$

and the distribution of the ratio of any two given power spectra, z (i.e. ratio of χ_2^2 distributions) is given by the log-logistic distribution (Eq. 3.5). For a non-normalized random variable, r, one can obtain the probability distribution by change of variable, introducing

$$z = \frac{r}{s} \tag{3.6}$$

where s is the appropriate normalizing factor. The resulting PDF is given by

$$g(r) = \psi\left(\frac{r}{s}\right)\frac{dz}{dr}. \tag{3.7}$$

Hence,

$$g(r) = \frac{1}{s}\frac{1}{\left(\frac{r}{s}+1\right)^2}. \tag{3.8}$$

For the power spectra ordinates, it is known that $2I/P$ is χ_2^2. Hence, if $x = 2I_1/P_1$ and $y = 2I_2/P_2$ then, $z = I_1P_2/I_2P_1$, and $r = I_1/I_2$, $s = P_1/P_2$. Thus, the PDF of the ratio of the power spectra ordinates is calculated to be

$$g(R_i) = \frac{1}{S_i}\frac{1}{\left(\frac{R_i}{S_i}+1\right)^2}, \tag{3.9}$$

where $R_i = I_{1i}/I_{2i}$, is the power spectra ratio and $S_i = P_{1i}/P_{2i}$ is the true ratio of the spectral power.

In this study, several power spectra are summed, which changes the distribution by altering the number of degrees of freedom. The ratio of two χ^2_ν distributed variables can be shown to be distributed following the F-distribution, given by

$$F(z;\nu,\varphi) = \frac{1}{\beta(\frac{\nu}{2},\frac{\varphi}{2})}\left(\frac{\nu}{\varphi}\right)^{\frac{\nu}{2}} z^{\frac{\nu}{2}-1}\left(1+z\frac{\nu}{\varphi}\right)^{-\frac{\nu+\varphi}{2}}. \tag{3.10}$$

where ν and φ are the degrees of freedom (number of parameters), and β is the beta function. The log-logistic distribution is recovered for $\nu = \varphi = 2$. For $\nu = \varphi$, the F-distribution simplifies to

$$F(z;\nu,\nu) = \frac{1}{\beta(\frac{\nu}{2},\frac{\nu}{2})} z^{\frac{\nu}{2}-1}(1+z)^{-\nu}. \tag{3.11}$$

The F-distribution is an asymmetric distribution with a minimum value 0 and no maximum value. In Figure 3.5 the nature of the distribution for various values of the degrees of freedom ν and φ is shown. There is a different F-distribution for each combination of these two degrees of freedom. The distribution is heavily right-skewed for smaller values of ν and φ, which means there are a long tail and an increased chance of more extreme large values. As the degrees of freedom increase, the F-distribution is more localized.

As before, substituting in the normalized variables gives

$$g_{\nu,\nu}\left(\frac{R_i}{S_i}\right) = \frac{1}{S_i}\frac{1}{\beta(\frac{\nu}{2},\frac{\nu}{2})}\left(\frac{R_i}{S_i}\right)^{\frac{\nu}{2}-1}\left(1+\frac{R_i}{S_i}\right)^{-\nu}. \tag{3.12}$$

Assuming a model $S(\theta)$ for the true power ratio, with unknown parameters θ, the joint probability density of observing N periodogram ratio points R_i is given by the likelihood function, $\mathscr{L}$, where

$$\mathscr{L} = \prod_{i=1}^{n} p(R_i|S_i) = \prod_{i=1}^{n} \frac{1}{S_i} F\left(\frac{R_i}{S_i};\nu,\nu\right). \tag{3.13}$$

Maximizing the likelihood is equivalent to minimizing the negative of the log of the likelihood function, namely

$$\begin{aligned} -2\ln\mathscr{L} &= 2\sum_{i=1}^{n}\left[\ln S_i + \ln\beta\left(\frac{\nu}{2},\frac{\nu}{2}\right)\right. \\ &+ \left.\left(1-\frac{\nu}{2}\right)\ln\left(\frac{R_i}{S_i}\right) + \nu\ln\left(1+\frac{R_i}{S_i}\right)\right]. \end{aligned} \tag{3.14}$$

Loop No.	Half Loop Length (Mm)	Power ratio (MLE fit)	ξ (MLE fit)	Power ratio (least-squares fit)	ξ (least-squares fit)	Propagation speed (km s^{-1})
1	100 ± 7	0.75±0.17	1.83±0.76	0.90	2.57	687±17
2	197 ± 9	0.67±0.15	2.65±0.55	0.91	4.46	679±14
3	327 ± 12	0.80±0.18	3.86±0.47	1.05	5.81	666±14
4	488±17	0.63±0.14	4.82±0.43	0.78	6.17	658±38
5	553±18	0.71±0.16	4.76±0.37	0.87	5.52	676±15

Table 3.1 Measured loop parameters and wave parameters obtained from MLE. The uncertainties shown correspond to the standard deviation of the mean for MLE parameters and standard deviations for loop parameters. The error in loop length corresponds to the pixel uncertainty of the instrument, the PFSS extrapolation provides us with another uncertainty namely a projection of up to 20° (0.94 Mm). The least-squares estimates do not have an associated error the error estimates for the associated parameters with least-squares fitting weren't available.

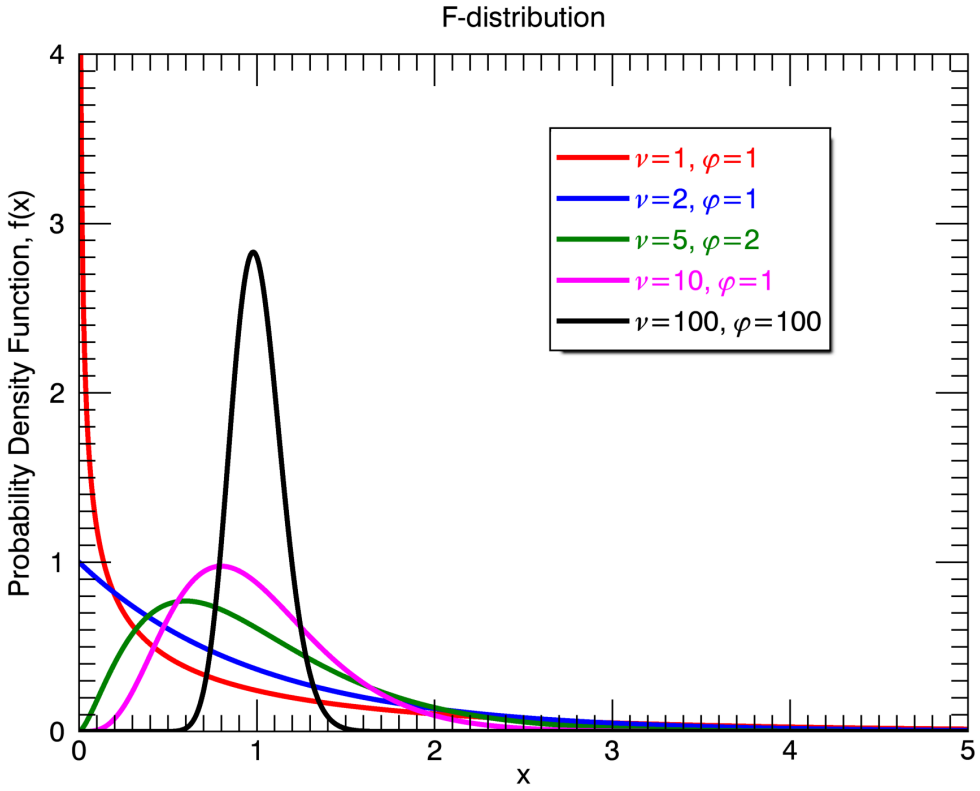

Fig. 3.5 Probability density function for F-distribution with different degrees of freedom for a random variable, x. In the case of $\nu = \varphi = 100$, the density function is log-normally distributed.

3.3.5 Maximum Likelihood Estimation

The observed power ratios shown in Figure 3.4 are then used to estimate the model parameters for the power ratio, i.e. the power ratio scaling factor, P_{out}/P_{in} and the factor in the exponential, $2L/v_{ph}\xi$ given in Eq. (1.34). The minimisation is done using the Powell minimisation method using the IDL *POWELL* function (e.g., Barret & Vaughan, 2012).

The associated confidence intervals on the model parameters can be estimated by utilizing the *Fisher Matrix* $(\mathscr{F})$. The components of $\mathscr{F}_{ij}$ are defined as the expected value of the *Hessian* $(\mathscr{H})$

$$F_{ij} = \left\langle -\frac{\partial^2 \ln \mathscr{L}}{\partial\theta_i \partial\theta_j} \right\rangle, \tag{3.15}$$

where θ represents the model parameters (Pawitan, 2001; Bevington & Robinson, 2003). The *Fisher matrix* is a $N \times N$ matrix for N model parameters. The inverse of the *Fisher Matrix* (Equation 2.17)gives the covariance matrix, the diagonal elements of which give the standard error squared on each model parameter, σ^2. The off-diagonal matrix elements provide the covariances between parameters. The *Fisher*

Matrix only gives reliable uncertainties when the likelihood surface can be approximated by a multi-dimensional Gaussian. The values obtained from the covariance matrix as the estimated parameter uncertainties are given, and have been checked that they are in close agreement with more involved methods of calculating confidence levels, e.g., Wilks confidence intervals (Bevington & Robinson, 2003). At best, the given uncertainties and confidence intervals should be taken as a lower limit.

The standard errors are used to calculate the point-wise Wald 95% confidence intervals (Bevington & Robinson, 2003) for the model. The likelihood surface and covariance matrix suggest covariance between the model parameters and this is included in the confidence interval calculation. For the measured power ratios given in Figure 3.4, the likelihood surfaces are close to a bivariate Gaussian, thus the corresponding confidence bands calculated are reliable. It is noted that in the case of the ratio of two single (i.e., non-averaged) power spectra ($\nu = 2$), the likelihood function is irregular and the *Fisher Matrix* will likely provide a poor coverage of the confidence intervals.

3.4 Results and Discussion

3.4.1 Potential Field Extrapolation

Potential field extrapolations are undertaken with PFSS to determine the geometry for the quiescent coronal loop system shown in Figure 3.1. In particular, the focus is on whether the wave paths determined from following the Alfvénic fluctuations are situated in the LOS, which has been the implicit assumption in previous analyses (Tomczyk & McIntosh, 2009; Verth et al., 2010). This assumption has an impact on the measured propagation speeds and lengths of loops, both of which are important quantities for determining the equilibrium parameter ξ from the data (see Equation 1.34). The plotted magnetic field lines in Figures 3.1 and 3.2 are not supposed to represent the specific coronal loops along which the waves propagate. However, it is expected that the extrapolated field represents the general behaviour of the magnetic field in the region, and as such, describe the oscillating loops. Moreover, as mentioned earlier, the spatial resolution of CoMP essentially precludes identifying individual coronal structures. The extrapolated field demonstrates that the loops are approximately situated in the POS, with a maximum angle between the loops and POS found to be 20° (see Figure 3.2).

The loops in EIT images are identified and using the corresponding location of these loops in the CoMP observations the loops are extrapolated. Furthermore, it can be inferred from the extrapolated field lines plotted in the left panel of Figure 3.1 that the geometry of the coronal loops is not symmetric about the apexes. Given that the model used for fitting the wave damping is derived under the assumption that both

the outward and inward waves have propagated along half of the loop (Eq. 1.34), this will likely affect the estimates for ξ (discussed further in Section 3.4.3). In Section 3.6, a more general model is provided for the exponential damping that can be fit to the data when measuring over a segment of the loop, although knowledge of total loop length and the segment length is required, and for this data set there are no stereoscopic data available that would help us achieve this. Moreover, it would be risky to determine any one-to-one correspondence between the extrapolated field lines and the wave angle guided tracks. Given that the main purpose of this work is to present a more appropriate method for fitting the observed power ratio and demonstrate that the least-squares method gives incorrect model parameters, such a limitation does not invalidate this aim.

3.4.2 Wave Power Analysis

Using two-dimensional Discrete Fourier transforms, the inward and outward components of the wave power corresponding to the Alfvénic waves propagating along five wave paths of increasing length (wave paths are shown in Figure 3.1 centre panel) are identified. The $k-\omega$ diagrams for three of the wave paths are displayed in Figure 3.4 (left column) and indicate the relative strength of the outward and inward propagating Alfvénic waves in the segment of the loop under consideration. The $k-\omega$ diagrams have the distinct ridges reported in previous observations, corresponding to the near dispersion-less kink mode, where the negative frequencies correspond to outward waves and positive are inward waves. Given that the spatial frequency-resolution is lower for the shorter loops (Figure 3.4 top left) compared to the longer loops (Figure 3.4 bottom left), the $k-\omega$ diagrams are less well resolved for the shorter loops. Despite this, it can be noticed that as the length of the loop increases, the relative power in the outward propagating Alfvénic waves to the inward propagating waves increases. Assuming that the Alfvénic waves entering the corona at both footpoints of the loops have the same power spectra, then this potentially has a trivial explanation: For longer loops, the inward propagating waves will have travelled further distances and they should be expected to have been damped to a greater degree, as suggested by Eq. (1.34). Upon collapsing the spectra in the wavenumber direction and taking the ratio of the outward to inward spectra, the plots in the right columns of Figure 3.4 are obtained. The power ratio shows an apparent upward trend as a function of frequency indicating wave damping, with the relative magnitudes of the power ratio supporting the visual impression from the $k-\omega$ diagrams and indicates greater wave damping for the longer loops. The ratio of power spectra up to 4 mHz is shown following Verth et al. (2010). This is largely since the signal drops below the noise level for the inward propagating waves beyond this frequency and leads to a turnover in the power spectra.

3.4.3 Maximum Likelihood Analysis

Using the derived likelihood function (Eq. 3.14) the power ratio model (Eq. 3.1) is fitted to the data points shown in Figure 3.4. The maximum likelihood model parameters are used to define the model power ratio curve (red solid line right column of Figure 3.4), with the values in the covariance matrix enabling us to generate the point-wise Wald confidence bands at 95% via bootstrapping. The confidence bands demonstrate that in each case, there is a clear trend in the power ratio as a function of frequency and supports the idea that frequency-dependent wave damping is in action along each wave path (Verth et al., 2010).

Given that previous work has employed the least-squares method for fitting the power ratio model, the differences between the parameter estimates from least-squares and MLE methods are also demonstrated. In Figure 3.4 (right column) the model curves obtained from the least-squares (black solid line) are over-plotted and demonstrate that they underestimate the amount of damping present, i.e., corresponding to flatter curves, when compared to the MLE method.

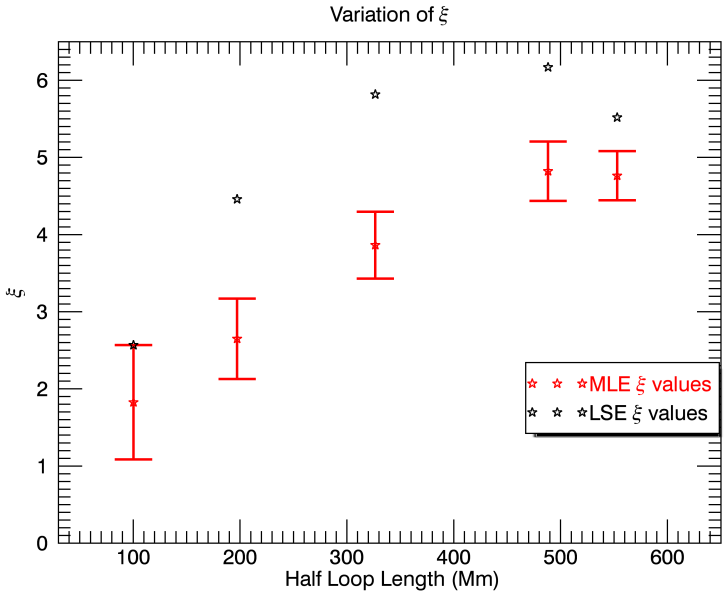

Fig. 3.6 Variation of equilibrium parameter ξ with loop length, with associated error bars. The longer loops have higher value of ξ.

To estimate the equilibrium parameters (quality factor), ξ, for each selected wave path, the length of the wave path used is also required which is taken to be the half-loop length (L), and the propagation speed of the Alfvénic waves (υ_{ph}). The values are summarized in Table 3.1. The measured propagation speeds of $\approx$680 km s^{-1} are consistent with the values obtained in previous studies (Tomczyk & McIntosh, 2009; Morton et al., 2015). This value is averaged over the outward and inward wave propagation speeds, as the potential influence on damping from flows along

the loop is not considered in this study. The presence of flows leads to modification of the TGV relation (Soler et al., 2011).[3] Furthermore, studies of the interaction between the flows (namely the solar wind) and Alfvén waves suggest wave action conservation is important, which can result in dissipation-less waves undergoing apparent damping (Jacques, 1977; Heinemann & Olbert, 1980; McKenzie, 1994; Li & Li, 2007; Cranmer et al., 2007; Chandran et al., 2015). In the case of coronal loops estimating flows is not a trivial endeavour; although the corona is likely to be in a state of thermal non-equilibrium and flows are expected to be present throughout. Several studies have tried to quantify the flow speeds, largely in active region loops, which are typically of the order of 10-50 km s^{-1} (Reale, 2010). Moreover, speeds of 74-123 km s^{-1} have also been found in a single event (Ofman & Wang, 2008). These studies suggest the axial flow speed is potentially small compared to the local Alfvén speed, and thus this should have little effect on this result. However, further examination of flows in coronal loops is required to assess their impact.

The increase in loop length between the wave paths corresponds to loops reaching higher altitudes in the corona. In Figure 3.6, the measured values of ξ as a function of loop length are demonstrated, and the observations suggest that for the longer loops that reach higher up in the corona, the quality factors increases and, hence, the damping length increases, suggesting the Alfvénic waves are subject to a reduced rate of damping. This is in contrast to the $k-\omega$ diagrams and power ratios, which show a greater difference between the outward and inward wave power. This is naturally explained by the fact that the inward waves have propagated further along the longer loops and have been damped to a greater degree than those in the shorter loops, despite the apparent reduced rate of damping in the longer loops. This result is present in both the MLE and least-squares fitting, however, the least-squares approach tends to overestimate the fitted values of power ratio and equilibrium parameter.

Given the aforementioned problems with this data set, related to identifying whether the selected wave paths are truly half the loop length, it is important to be cautious in the interpretation of this variation in quality factor with loop length. A physical explanation for the decrease in damping rate can be made in terms of the density ratio between the internal and external plasmas. If it is assumed that the coronal loops are subject to similar rates of heating, and the rate of chromospheric evaporation is similar, then the average density of the longer loops is likely to be less than those of shorter loops. Hence, compared to the ambient plasma the density ratio (ρ_i/ρ_e) for longer loops is, on average, less than for the shorter loops. Eq. (1.32)

[3] It should be noted that any density stratification along the loop will not impact upon the measured power ratio, has any effect on the average amplitude will be the same for both outward and inward waves.

then implies the equilibrium parameter will increase as the density ratio decreases and matches the observed behaviour.

Moreover, the fact that potentially the wave path along half a loop is not measured will change the model that should be fit to the power ratio (Eq. 3.18) and alter the measured values of the parameters. Considering the magnetic field extrapolation, there is the possibility that a loop segment measured is less than half the loop length. In such a scenario, the average power over this shorter segment, compared to a half loop segment, will be greater for outward waves (as the wave amplitudes averaged over have been damped less over this distance) and less for the inward waves (as the wave amplitudes averaged over will have been subject to greater damping). Hence, the power ratio will be artificially enhanced, giving the appearance of greater damping. This would lead to an underestimation of ξ compared to its true value. Hence, the observed effect of increasing ξ with height would be more pronounced.

Finally, it is also worth commenting on the measured value of the factor P_{out}/P_{in}, which represents the power of the waves input into the corona at each footpoint of the loop, called the 'footpoint power ratio'. The input power ratio at footpoint, obtained is almost equal to unity in the case of least-squares estimation, consistent to the previous study of Verth et al. (2010) and was interpreted as the wave power being generated was the same at both the footpoints. In the case of MLE estimation, it is obtained that the footpoint power ratio is less than unity, implying that the wave power generated at the footpoint associated with inward waves is larger than the other. The current level of uncertainties associated with the measurements does not permit us to rule out that the input power is equal at both footpoints. However, it would not be surprising if the magnitude of the wave power is different at both footpoints, given the physical conditions at the wave source region are likely to be dissimilar.

3.5 Conclusion

In this study, the methodology for investigating the damping of propagating Alfvénic waves from spectroscopic data is advanced further. The main goal was to provide an improved and more robust method for fitting the ratio of two power spectra, taking into account the statistical properties of the expected distributions of the power ratio for each frequency ordinate. Upon application to a previously studied CoMP data set, the previous conclusions are confirmed, namely, that the Alfvénic waves are subject to damping, with resonant absorption suspected as the main damping mechanism. However, it is also found that the previously used methodology for fitting the power ratio, i.e., least-squares, has the potential to provide bias estimates of the model parameters, namely the quality factors, ξ, and footpoint power ratio

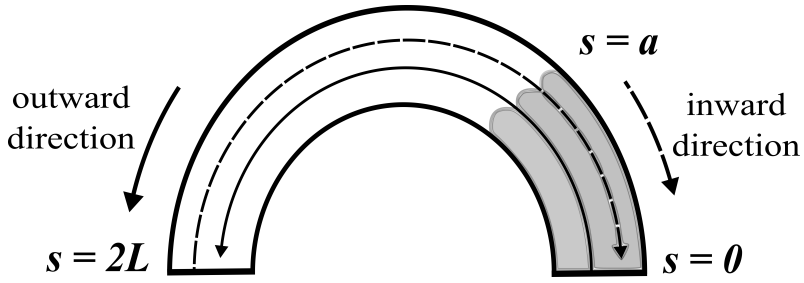

Fig. 3.7 Simple illustration of the observed semi-circular geometry of the coronal loop system. The direction of outward and inward wave propagation is shown by the arrows.

P_{out}/P_{in}. Importantly, the least-squares fit likely overestimates ξ, leading to an underestimation of the strength of the wave damping. An accurate estimate of the quality factor is key in quantifying the rate of energy transfer and the amount of wave energy that might be contributing to plasma heating.

Despite issues with determining the true geometry of loops in this study, by looking at different wave paths in the data this study can find the first potential piece of evidence that the damping length increases as the loop length of loops that reach higher up in the corona increases. The result appears consistent with the result obtained in the case of damped, standing kink waves, where the damping time increases as the loop length increases (Verwichte et al., 2013b). While it is unclear what may be the underlying cause of this, it could potentially be explained by a decreasing average density ratio between the loop and ambient plasma as loop length increases.

Given the ubiquity of propagating kink waves in the corona has been established, there is a clear need to accurately estimate the damping of propagating kink waves to understand the transfer of energy and the contribution of Alfvénic wave energy towards plasma heating. The results presented here highlight the need to further investigate the damping of coronal kink waves and provide a robust methodology to achieve this. Future studies should aim to overcome some of the shortfalls associated with the current work.

3.6 A Modified Model

A modified model for the power ratio is presented taking into account the fact that it might not always be possible to observe full loops that are oriented in the plane-of-sky. A schematic of physical situation is shown in Figure 3.7, where one is only able to measure wave behavior in the shaded section of the loop, from the footpoint, $s = 0$, to $s = a$. The average power over the segment associated with the outward

propagating waves is given by

$$\langle P(f)\rangle_{out} = \frac{1}{a}\int_0^a P_{out}(f)\exp\left(-\frac{2f}{v_{ph}\xi_E}s\right)ds. \tag{3.16}$$

Similarly the average power associated with the inward propagating waves is given by,

$$\langle P(f)\rangle_{in} = \frac{1}{a}\int_{2L-a}^{2L} P_{in}(f)\exp\left(-\frac{2f}{v_{ph}\xi_E}s\right)ds. \tag{3.17}$$

The ratio for the power ratio $\frac{\langle P(f)\rangle_{out}}{\langle P(f)\rangle_{in}}$ is obtained as

$$\langle P(f)\rangle_{ratio} = \frac{P_{out}}{P_{in}}\frac{\exp\left(\frac{-2fa}{v_{ph}\xi}\right)-1}{\exp\left(\frac{-4Lf}{v_{ph}\xi}\right)-\exp\left(\frac{-2f(2L-a)}{v_{ph}\xi}\right)}. \tag{3.18}$$

This equation can then be used as the model for MLE to obtain an estimate of damping length when examining only a segment of the loop, only if a reasonable estimate for a is known.

Chapter 4

Statistical properties of damping of kink waves

4.1 Introduction

The presence of MHD waves in the solar atmosphere is well established by now. The previous chapters provided a broad introduction to various MHD modes. The advancement in instrumentation has brought us closer and closer to discovering new wave modes in the atmosphere. However, the transverse waves have been observed and study for less than three decades. There have been several attempts to consolidate the understanding of the damped standing kink waves, an exhaustive numerical study is performed in Pascoe et al. (2019), to use these observations in coronal magneto-seismology to estimate the physical properties of the plasma in which these loops reside in. More recently, it was demonstrated that there are persistent and ubiquitous fluctuations in the Doppler velocities of coronal emission lines, which propagate at Alfvénic speeds and follow magnetic field lines (Tomczyk et al., 2007; Morton et al., 2019).

Finally, there has been the more recent discovery of 'decayless' standing kink wave modes (Anfinogentov et al., 2013; Nisticò et al., 2013; Anfinogentov et al., 2015) in the solar active region loops. These low-amplitude ($<$ 1 Mm) oscillations do not appear to damp in time and are seen for a number of cycles. In some cases, the amplitude are shown to gradually grow Wang et al. (2012). The connection between the standing 'decay-less' kink waves and the propagating waves is not understood yet. There is a clear lack of statistical study of these propagating kink waves, observed in the quiescent coronal loops. This paper attempts to fill that gap of knowledge and provides with a catalogue of suitable quiescent coronal loops for which we can study the propagating kinks waves. It has been done for the damped standing mode (Nechaeva et al., 2019), decayless standing mode (Anfinogentov et al., 2015) , so we now do it for propagating. We also provide an overview of some of the basic wave properties. This study also serves as a natural extention to the study by Tiwari et al. (2019).

Currently, the best way to study the propagating waves is through the analysis of CoMP data, as it is one of the few instruments that takes observations of the LOS Doppler velocity. This makes the analysis of damping of propagating waves possible through the power ratio. In Chapter 3 the analysis of power spectra and their ratio required the use of MLE techniques in order to provide accurate parameter estimates and uncertainties, is demonstrated. Here the initial study is advanced and a large-scale study of coronal loops observed in CoMP is undertaken to examine the typical properties of damped propagating kink waves. A comparison of these results to the existing results from the analysis of standing kink modes is also presented.

The chapter is structured as follows: in Section 4.2 the details of the data used are given. The next Section 4.2 describes the analysis methods used. In Section 4.3,

a discussion of the main findings of the study are presented and the chapter is concluded with a section on conclusions presented in Section 4.4.

4.2 Data and analysis

4.2.1 Data: CoMP

The data used in this chapter were obtained from multiple sources. The primary data is from the Coronal Multi-channel Polarimeter (CoMP Tomczyk et al., 2007, 2008), the details of which are discussed in Chapter 2.2.1. The three-point measurements of the 10747 Å Fe XIII coronal emission lines are used for this study (for details see Subsection 2.2.1). The data were selected from CoMP observations between 2012-2016. The dates on which there were more than 135 (near)-contiguous frames were identified by a manual inspection on the CoMP data webpage and are given in Table 4.1. The Doppler velocity image sequence of the corona between 1.05 $R_\odot$ and 1.35 $R_\odot$ for each selected date has a temporal cadence of 30 seconds, and spatial sampling of 4 $''$.5. The details of data acquisition and the data reduction steps are discussed in Subsection 2.2.1.

4.2.2 Data: SDO

As well as examining the propagating kink waves, we want to provide a comparison with the measured properties of the standing modes. To this end, the standing kink waves catalogue generated by Nechaeva et al. (2019, Table 01) is utilised. This catalogue was compiled by identifying the oscillation events found via the Heliophysics Events Knowledgebase (Hurlburt et al., 2012) using the AIA instrument on board SDO. These were checked for the period from 2014 May 20 to 2018 December 26. Besides, the time interval from 2017 August 1 to October 31, including the period of high solar activity at the beginning of 2017 September, was looked through manually using JHelioviewer (Müller et al., 2017). This compiled catalogue covers almost the entire 24th solar cycle. A table of the most relevant properties is reproduced in Table A.2. The kink wave speed is calculated assuming the fundamental mode of oscillation. The wave properties here are not calculated using the MLE method, described for the propagating wave case.

The difference between the FOV of these two instrument changes what one means by looplength. AIA observations are full-Sun images, it is possible to see the footpoints of coronal loops in the corona and thus it is easier to observe a complete coronal loop. However in the case of CoMP observations the looplength of the coronal loop refers to the partial looplegth as seen by the CoMP FOV. CoMP loops

footpoints are identified as the observations at the starting point of the coronal loops as seen in the CoMP FOV.

4.2.3 Selection of loops for study

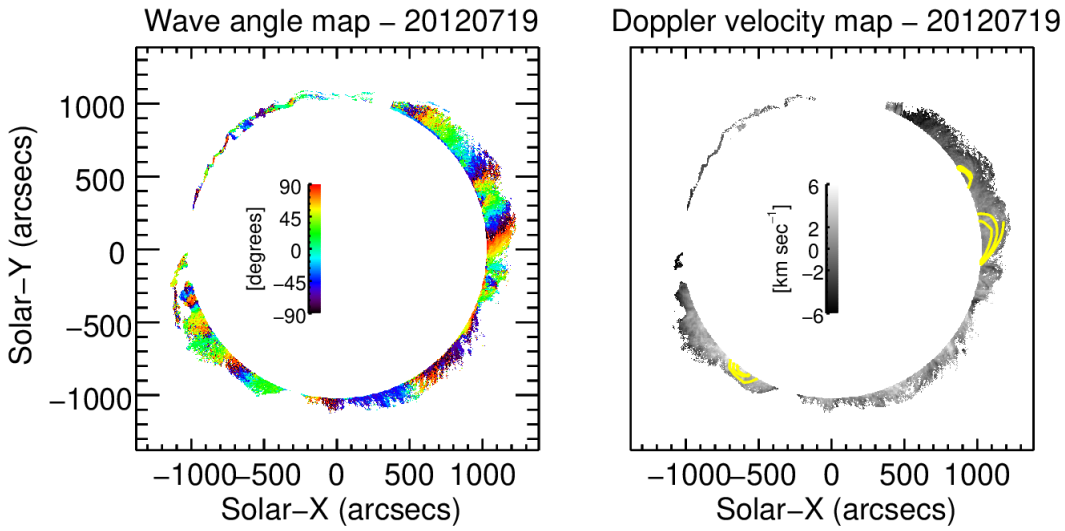

Fig. 4.1 A sample observation for the loops observed on 19-July-2012. The *Left panel* shows the calculated wave angle at each pixel position, determined using a coherence based method (see Section 3.3.2) on each pixel of the Doppler velocity image. This wave angle serves as the guide for the tracks shown in yellow in the Right panel.

The looplength incase of CoMP observations referes to the half looplength as seen in the comp FOV. The selection of the loops from the CoMP data is a key step in the analysis of the waves. For each of the datasets, we identified suitable systems of coronal loops that were at least longer than 50 Mm. This is done to preserve a high signal to noise level as the smaller loops suffer from a greater impact of noise due to being closer to the occulting disk, and the imposition of a minimum loop length also provides a reasonable sampling in the k-direction in Fourier space. A few such selected loops are shown in the *Right panel* of Figure 4.1. The loops are chosen by manually identifying closed-loop structures in the wave angle map. A point is selected on the wave angle map and the wave angles are followed until the wave path reaches the occulting disk present in the CoMP data. The second criteria for loop selection were that the loops should be orientated such that they are close to being positioned in the plane-of-sky. The PFSS extrapolations do not provide one-one correspondence with the observerd loop structures as it is difficult to observe the the CoMP resolution. The geometry and orientation of the loops are identified by performing magnetic field extrapolations. The extrapolations provide us with a schematic geometry and orientation of the loops in the plane-of-sky. The extrapolations were performed using the Potential Field Source Surface (PFSS -

Schrijver & DeRosa 2003). The extrapolated field lines visibly agree with the loop structures visible in the coronal EUV images obtained by AIA/SDO. Furthermore, the loops are selected to avoid loops within the cores of active regions (i.e. rooted in or near sunspots), as we are interested in the loops that are rooted in-quiet Sun. Some of the trans-equatorial loops identified were located in the extended plage region of ARs on the visible solar disk. The loops observed are assumed to be rooted in network regions and are not part of active region loop systems. Figure 4.2 represents the comprehensive list of loop apex positions of all the loops analysed for the analysis presented here.

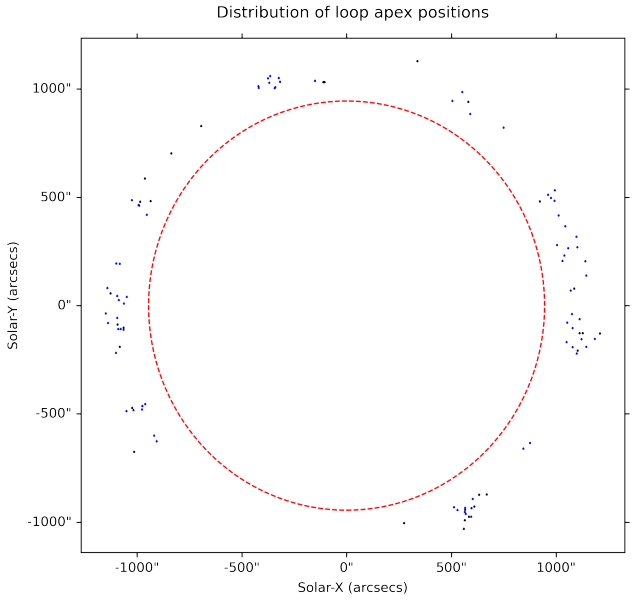

Fig. 4.2 Position of all loops analysed. The black dots denote the location of the loop apex for the loops with $\xi < 0$ and the blue dots correspond to the loop apex for the loops with $\xi > 0$. The solar disk is represented by the red dashed lines.

4.2.4 Parameter Estimation

The identification of the wave propagation direction is an important step in the analysis. A coherence based approach described by McIntosh et al. (2008) and further used by (Tomczyk & McIntosh, 2009; Morton et al., 2015, 2016; Morton et al., 2019; Tiwari et al., 2019) forms the basis of the wave angle calculation (see Section 3.3.2 in the thesis). The strategy is to use the coherence between the Doppler velocity time-series of each pixel and its neighbouring pixels to obtain islands of coherence above a threshold value. The direction of wave propagation is calculated by a straight line fit, which minimises the sum of perpendicular distances from the points to the line. Doing this for each pixel of the Doppler-velocity time series images gives the wave angle map. A sample wave angle map is shown in the *Left*

panel of Figure 4.1. The wave angle maps obtained are further used to determine the path of the wave propagation through the corona as discussed in Section 3.3.2.

As discussed above, for each of the chosen dates the various wave paths are assumed to follow the quiescent coronal loops. The loops are difficult to trace automatically as the loop length changes for a coronal loop system with altitude. A median filter of box size having a width two pixels was applied to the wave angle map to try and suppress some of the noise in the wave angle maps. This led to the improved tracing of wave-paths. For each loop, the half loop length, is defined, which is obtained by finding the point of inflexion for the traced trajectory of the wave path. The longer loop lengths cause additional issues in tracing them because the wave angle suffers from larger uncertainties closer to the apex of larger loops. This arises due to wave angle being poorly estimated and sometimes due to poor data quality. In such cases where the whole loop was difficult to trace, only the wave path for half a loop is obtained.

The Doppler velocity signal along the wave paths is extracted and time-distance maps are created. A cubic interpolation maps the velocities from the selected wave paths onto (x,t) space. For each wave path, the neighbouring five wave paths on either side of the original wave path are also extracted. An FFT of these Doppler velocity time-distance map produces the $k-\omega$ spectra which are used to separate the inward and outward components of the wave propagation as shown in left panels of Figure 4.3. The propagation speed for the waves is calculated in a manner similar to (Tomczyk et al., 2007; Tomczyk & McIntosh, 2009; Morton et al., 2015; Morton et al., 2019; Tiwari et al., 2019), using the lag of the cross-correlation of the time-series at the centre of the wave path to the neighbouring time-series along the path. This is determined by fitting a parabola to the peak of the correlation function. The fit of the slope of the observed lags as a function of the position along the wave path gives the propagation speed of the wave. The median of this propagation speed is calculated for each wave path which is then added to the table.

The wave power for the inward and outward component of the waves are obtained by summing the spectra in the k-direction. For each loop, the inward and outward spectra are averaged over the neighbouring wave paths to suppress the variability in the power spectra (see Section 3.3.4). From this one dimensional averaged wave power, the ratio of the outward and inward power, $\langle P(f)\rangle_{ratio}$, is determined.

The quality factor (equilibrium parameter ξ) is obtained by fitting the model power ratio given by Equation (1.34) to the data, using a maximum likelihood approach (Equation 3.14). For a detailed discussion on statistics of power ratio and maximum likelihood, fitting see Section 3.3.4 of the thesis. The log likelihood

function that is minimised is given by,

$$-2\ln\mathscr{L} = 2\sum_{i=1}^{n}\left[\ln S_i + \ln\beta\left(\frac{\nu}{2},\frac{\nu}{2}\right) + \left(1-\frac{\nu}{2}\right)\ln\left(\frac{R_i}{S_i}\right) + \nu\ln\left(1+\frac{R_i}{S_i}\right)\right]. \quad (4.1)$$

The associated confidence intervals on the model parameters were estimated by utilizing the *Fisher Matrix* ($\mathscr{F}$).

The equilibrium parameter is then calculated for each of the selected wave-tracks. The equilibrium parameter is found for 108 individual loops observed with CoMP. The various parameters that were obtained are shown in the corresponding Table 4.1.

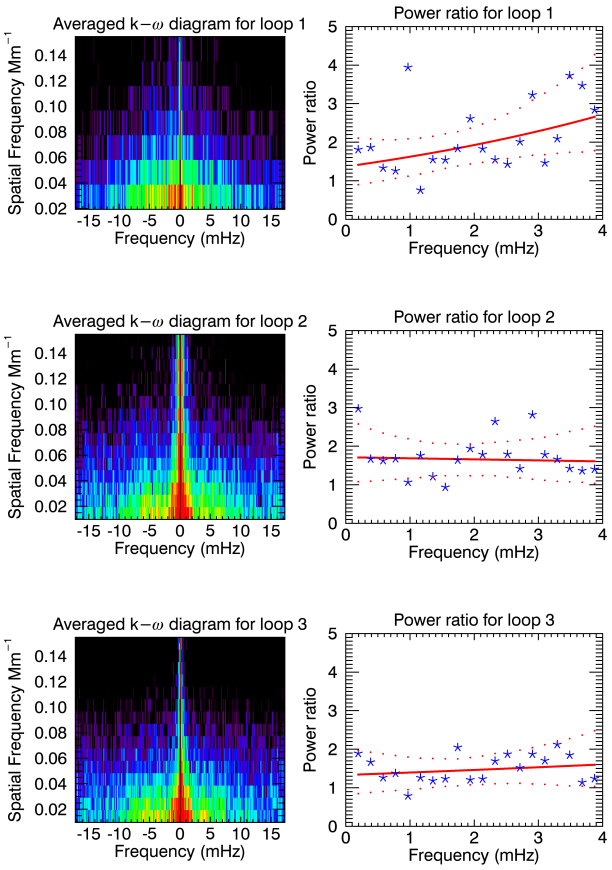

Fig. 4.3 Averaged $k-\omega$ diagrams for few selected tracks for the observations of 19-July-2012 as shown in Figure 4.1 (right). The *left* column displays the averaged $k-\omega$ diagrams. The *right* column shows the fitted power ratio. The measured power ratio for the coronal loops is shown here by the blue stars, for loops with increasing length. The results from the MLE fitting of the resonant absorption model are over-plotted (red solid), with point-wise Wald confidence bands shown at 95% (red dotted).

As an example of some of the typical results obtained, the power spectra corresponding to three different loops identified on 19^{th} July 2012, is shown in Figure 4.3.

The loop 1, 2, 3 corresponds to the half loop lengths of 61.44 Mm, 103.47 Mm, and 336.28 Mm, respectively. Loop 1 shows faster damping with a small equilibrium parameter of 0.89 ± 1.12, a phase speed of 402 ± 4.62 km s^{-1} and a footpoint power ratio of 1.37 ± 0.58. Loop 3 which is about 3 times the length of loop 1 however shows a weaker damping with ξ =28.29 ± 6.51, phase speed of 428 ± 6.64 km s^{-1} and footpoint power ratio of 1.08 ± 0.45. The loop 2 however exhibits a negative equilibrium parameter (-13.89 ± 11.01), this is discussed later in Section 4.3.5. As an example, these 3 values are different from the value of the equilibrium parameter found in Chapter 3, representing large positive and small negative values of ξ. However, as will be seen in the following section, these loops are representative of the wide variety of wave properties that are found in the CoMP loops (see Figure 4.3).

4.3 Results and Discussion

The observed equilibrium parameters along with other details of the oscillations were recorded and are listed in Table 4.1. In the following, a summary of the main properties of the propagating kink waves is provided.

Date	**Half loop length (in Mm)**	**Equilibrium parameter (ξ)**	**ξ error**	**Footpoint Power Ratio**	**Footpoint Power Ratio Error**	**Phase speed km s^{-1}**	**Phase speed error kms^{-1}**
20120423	42.04	-1.53	1.27	2.1	0.61	291.31	1.94
20120626	45.27	-0.95	2.07	2.51	1.07	561.24	11.36
20120410	54.97	2.49	3.23	1.47	0.63	372.71	4.37
20120810	61.44	32.12	30.81	1.38	0.56	343.34	6.24
20120719	61.44	0.89	1.12	1.37	0.58	401.91	4.62
20120410	77.6	24.06	29.71	1.81	0.78	511.77	7.51
20120626	80.84	1.74	1.61	1.43	0.61	388.59	8.46
20120410	84.07	-0.9	1.08	2.01	0.87	566.49	9.8
20120410	84.07	-3.74	2.96	1.64	0.71	365.0	3.61
20120423	87.3	2.65	1.21	1.38	0.4	299.56	7.35
20120810	90.54	-8.96	5.19	1.5	0.61	307.87	3.58
20120120	97.0	4.36	2.35	1.36	0.57	285.47	5.28
20120719	97.0	-13.89	11.01	1.71	0.72	427.45	5.83
20130717	97.0	-2.0	2.37	2.04	0.88	630.42	36.31
20130717	100.24	13.13	13.96	1.49	0.65	557.26	8.54
20120121	103.47	1.55	1.3	1.19	0.44	536.67	8.31
20120719	103.47	-4.14	2.58	1.7	0.72	361.25	6.7
20120410	109.94	7.49	4.02	1.22	0.52	314.72	4.07
20120120	109.94	-5.19	4.18	1.88	0.79	506.88	16.85

Table 4.1 continued from previous page

Date	Half loop length (in Mm)	Equilibrium parameter (ξ)	ξ error	Footpoint Power Ratio	Footpoint Power Ratio Error	Phase speed km s^{-1}	Phase speed error km s^{-1}
20130717	113.17	-3.03	2.44	2.38	1.03	488.96	8.61
20120626	116.41	-5.9	3.53	1.34	0.56	383.53	4.62
20120410	119.64	22.03	15.14	1.67	0.72	439.37	6.85
20120810	122.87	-3.87	2.74	1.79	0.74	512.05	10.54
20120719	126.11	6.64	3.88	1.33	0.56	404.47	4.67
20120410	126.11	4.13	4.17	1.33	0.57	675.47	14.67
20120410	126.11	1.5	1.54	0.94	0.4	676.75	14.57
20120423	129.34	9.54	4.12	1.42	0.41	440.01	8.24
20120121	129.34	-2.32	1.22	1.61	0.6	444.87	5.45
20120121	129.34	-7.48	5.8	1.88	0.69	643.48	11.03
20120410	129.34	-5.57	3.28	1.35	0.58	414.64	6.26
20130717	129.34	26.71	18.19	1.71	0.75	461.09	11.0
20120423	132.57	2.91	1.46	1.1	0.32	514.91	9.27
20120120	135.81	-29.54	14.93	1.39	0.58	387.7	12.51
20120120	142.27	-3.49	1.7	1.65	0.69	403.03	11.18
20120121	142.27	1.02	0.55	0.58	0.22	444.82	6.48
20120810	142.27	3.11	1.55	1.25	0.51	402.07	9.15
20120810	142.27	1.4	1.02	0.97	0.4	577.09	12.32
20130717	145.51	-1.62	0.84	2.09	0.91	417.53	9.02
20120120	148.74	1.76	1.63	1.17	0.5	737.83	16.8
20120121	151.98	19.48	4.99	1.59	0.59	245.92	2.75
20120410	155.21	30.14	14.85	1.36	0.59	409.04	6.3
20140102	158.44	-12.38	6.96	1.43	0.6	498.78	19.78
20120121	158.44	7.01	4.22	1.51	0.56	597.7	9.4
20120120	161.68	-3.62	2.15	1.78	0.76	549.74	16.21
20120810	168.14	-3.1	2.23	1.62	0.66	716.36	22.22
20120121	168.14	6.3	2.6	1.38	0.51	433.09	9.52
20120120	171.38	-3.13	2.49	1.67	0.7	799.42	70.73
20120121	171.38	5.04	2.05	0.95	0.35	441.44	5.5
20120423	171.38	1.73	0.69	0.78	0.23	507.04	7.17
20120810	174.61	13.36	8.16	1.22	0.49	618.95	11.35
20120719	174.61	12.01	4.59	1.7	0.73	362.22	5.79
20120410	174.61	-18.74	7.81	1.45	0.62	393.82	6.32
20120719	181.08	69.39	49.75	1.73	0.73	716.81	18.28
20120410	184.31	-54.5	22.13	1.36	0.58	404.54	7.39
20120423	184.31	-99.76	32.84	1.18	0.34	484.64	6.86

Table 4.1 continued from previous page

Date	Half loop length (in Mm)	Equilibrium parameter (ξ)	ξ error	Footpoint Power Ratio	Footpoint Power Ratio Error	Phase speed km s^{-1}	Phase speed error km s^{-1}
20120423	197.24	23.79	7.75	1.17	0.33	510.59	7.66
20130717	200.48	12.85	5.53	1.46	0.62	461.13	12.44
20120410	203.71	10.04	3.7	1.19	0.51	399.93	6.66
20120120	203.71	32.08	13.29	1.31	0.55	475.1	10.65
20120410	210.18	5.07	1.67	1.01	0.43	365.25	5.14
20120719	216.64	12.92	4.46	1.16	0.48	413.5	4.55
20120120	216.64	12.48	5.93	1.35	0.57	580.08	10.39
20120423	223.11	-14.75	3.96	1.32	0.38	483.38	7.87
20120120	226.34	20.93	7.69	1.31	0.55	463.74	14.44
20120121	229.58	5.03	1.83	0.97	0.36	528.73	8.27
20120423	232.81	-162.2	45.2	1.27	0.36	517.81	11.11
20120121	236.05	42.89	14.95	1.15	0.42	530.61	7.57
20120719	245.75	5.29	2.77	1.26	0.53	699.38	16.72
20120423	245.75	37.74	9.51	1.12	0.32	492.48	9.21
20120719	248.98	-15.86	6.6	1.53	0.64	575.31	15.9
20120121	252.21	3.81	1.6	0.96	0.35	663.14	12.34
20120120	252.21	-45.93	13.29	1.32	0.55	412.36	17.01
20120120	258.68	-58.42	19.08	1.4	0.59	478.06	8.67
20130717	265.15	4.7	1.82	1.12	0.49	528.11	10.3
20120410	268.38	147.31	44.37	1.22	0.52	436.26	7.06
20120121	271.61	4.5	1.41	1.04	0.39	521.58	15.2
20120410	274.85	9.81	2.78	0.99	0.42	416.89	5.33
20120810	278.08	15.81	3.79	0.99	0.4	387.52	4.26
20120120	281.32	9.08	2.96	0.94	0.4	509.44	14.44
20120423	297.48	9.52	1.96	0.96	0.27	482.33	7.03
20130410	316.88	7.43	2.33	1.18	0.5	532.45	15.77
20120120	323.35	10.56	2.95	0.94	0.4	503.41	9.48
20120120	323.35	-16.11	4.3	1.45	0.61	491.09	8.54
20140102	323.35	34.65	6.62	1.0	0.42	338.2	33.32
20120121	333.05	3.01	0.87	0.77	0.28	593.49	11.78
20120719	336.28	28.29	6.51	1.08	0.45	428.4	6.64
20120719	349.22	10.71	3.55	1.21	0.51	631.58	17.06
20120719	362.15	11.2	2.42	0.96	0.4	429.38	6.3
20120121	384.79	3.7	0.59	0.61	0.22	381.05	3.92
20120121	407.42	22.89	4.62	1.07	0.39	529.96	9.26
20120121	413.89	12.22	0.98	0.63	0.24	201.86	5.24

Table 4.1 continued from previous page

Date	Half loop length (in Mm)	Equilibrium parameter (ξ)	ξ error	Footpoint Power Ratio	Footpoint Power Ratio Error	Phase speed km s^{-1}	Phase speed error km s^{-1}
20130717	430.06	8.41	1.95	0.97	0.41	525.23	11.23
20120121	430.06	2.64	0.48	0.45	0.17	475.31	8.01
20120120	449.46	4.18	1.08	1.04	0.48	582.28	15.13
20120120	472.09	147.4	31.01	1.09	0.45	559.62	59.81
20120120	472.09	4.29	1.19	1.04	0.48	595.97	75.93
20120121	472.09	12.4	2.22	0.74	0.28	522.93	15.05
20120719	475.32	58.08	8.96	1.05	0.44	407.08	7.16
20120526	475.32	5.49	0.99	1.7	0.5	595.96	19.96
20120423	478.56	11.75	1.81	0.74	0.22	566.52	10.21
20140102	485.02	4.17	1.23	1.03	0.47	704.22	26.74
20120121	507.66	4.54	0.56	0.53	0.2	376.37	5.92
20120120	523.83	3.2	0.64	0.92	0.41	522.49	15.31
20120121	523.83	51.98	10.25	0.89	0.33	640.8	12.51
20120120	523.83	147.33	30.93	1.09	0.45	621.22	16.87
20120121	527.06	5.32	0.95	0.64	0.24	588.94	9.35
20120121	569.1	35.24	2.95	1.0	0.37	296.59	5.98
20120121	601.43	5.45	0.75	0.61	0.22	517.46	8.6

Table 4.1 Measured loop parameters and wave parameters obtained from MLE. The uncertainties shown correspond to the standard deviation of the mean for MLE parameters and standard deviations for loop parameters. The error in loop length corresponds to the pixel uncertainty of the instrument, the PFSS extrapolation provides us with another uncertainty namely a projection between 5-25° (In the error estimation for looplength the maximum value of the angle of deviation is taken into account as the PFSS extrapolation and the observed loops do not have a one-one correspondence).

4.3.1 Distribution of oscillation parameters

The loop lengths for the traced coronal loops are in the range of 50-600 Mm. In Figure 4.4 the histogram distribution of all the loop lengths observed is shown. The distribution peaks at around 150-200 Mm, and most of the loops observed are between 50-250 Mm. The distribution after this tapers out, as it becomes increasingly difficult to trace the longer loops due to the limited FOV of the CoMP instrument.

The measured propagation speeds for the waves, are distributed between 200-800 km s^{-1}. The distribution is shown in Figure 4.5, which peaks around 400-600 km s^{-1}. This is consistent with the various propagation speeds reported in the literature around 500-600 km s^{-1} (Tomczyk et al., 2007; Tomczyk & McIntosh,

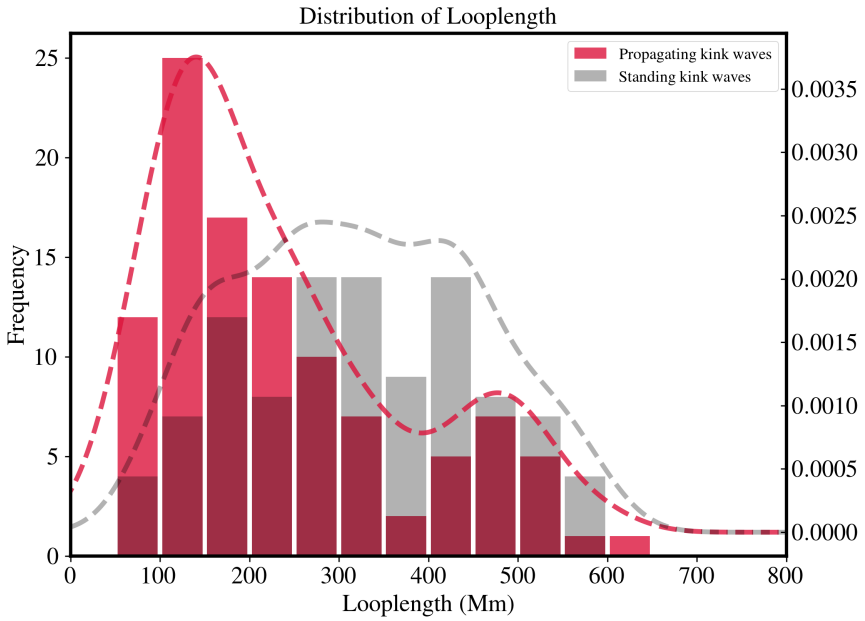

Fig. 4.4 Distribution of measured loop lengths of the traced loops for standing and propagating kink waves. The red bars and line represent the distribution and Kernel Density Estimate (KDE) of loop length for the propagating kink waves respectively. The grey bars and line represent the distribution and Kernel Density Estimate (KDE) of loop length for the standing kink waves respectively.

2009; Verth et al., 2010; Liu et al., 2014; Morton et al., 2015; Tiwari et al., 2019). The propagation speed values obtained are averaged over the outward and inward wave propagation speeds. There is some evidence that the inward and outward velocities are different (Tomczyk et al., 2007), which can be explained by the presence of flows along the coronal loops. However, the methodology for the measurement of the wave propagation speed is currently not sensitive enough to confirm this apart from in extreme cases, (e.g. in coronal holes Morton et al., 2015). The presence of flows leads to modification of the TGV relation described by Soler et al. (2011), which changes the model for power ratio that is used for the study. However, the influence of flows has been neglected in this study.

The power ratio, is obtained from fitting the ratio of outward and inward power, to the model equation of power ratio as provided in Equation (1.34). The distribution of the calculated input footpoint power ratio is shown in Figure 4.6. The footpoint power ratio does not provide any information about the driving mechanism, however, it can be used as a proxy for measuring the energy input at each footpoint of the loop. The driving mechanism of these waves is thought to be global, due to the ubiquitous nature of these waves. It is expected that the energy entering the corona through each footpoint will be approximately equal. The mean value of footpoint power ratio of 1 supports this hypothesis and strengthens the previous claims (Verth et al., 2010; Tiwari et al., 2019). The scatter around the value of 1 could indicate that in some

regions of the atmosphere the driver is weaker/stronger than in others, or due to the asymmetries in the loop particularly in the presence of flows.

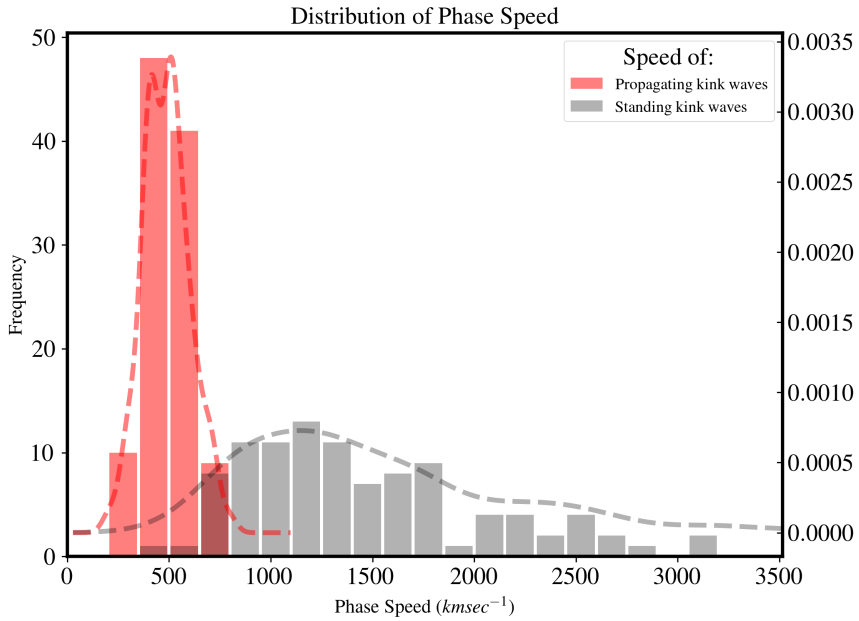

Fig. 4.5 Distribution of phase velocities for the observed waves. Right Y-tick-marks represent the normalised probability density and the left Y-tick-marks represent the normalised frequency

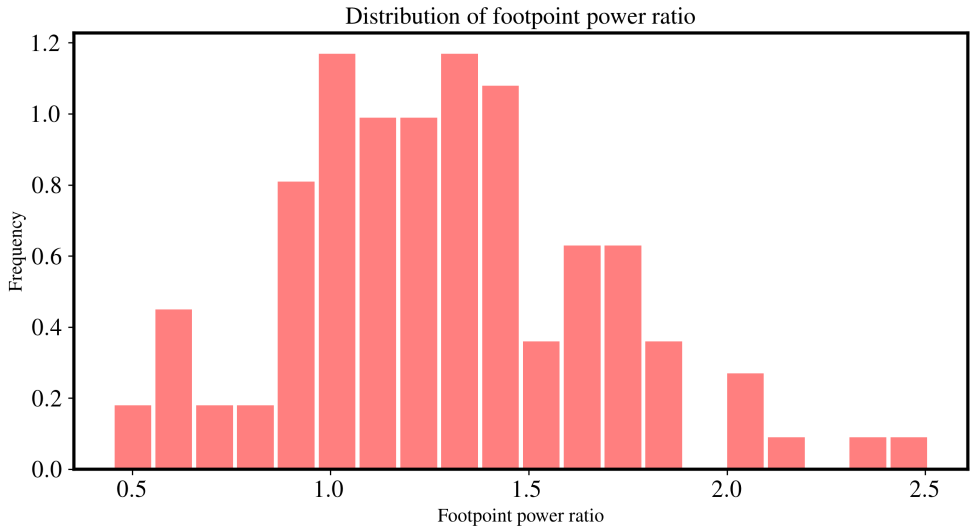

Fig. 4.6 Distribution of measured footpoint power ratios, after performing fitting for the observed waves

The most interesting parameter from the study is the equilibrium parameter or quality factor (ξ), which quantifies the damping rate in the model that is used (Ruderman & Roberts, 2002), it is distributed as presented in Figure 4.7. The ξ values for propagating kink waves are distributed in between the values of -162.2 and 147.4. The histogram shows only the positive values, and the negative values,

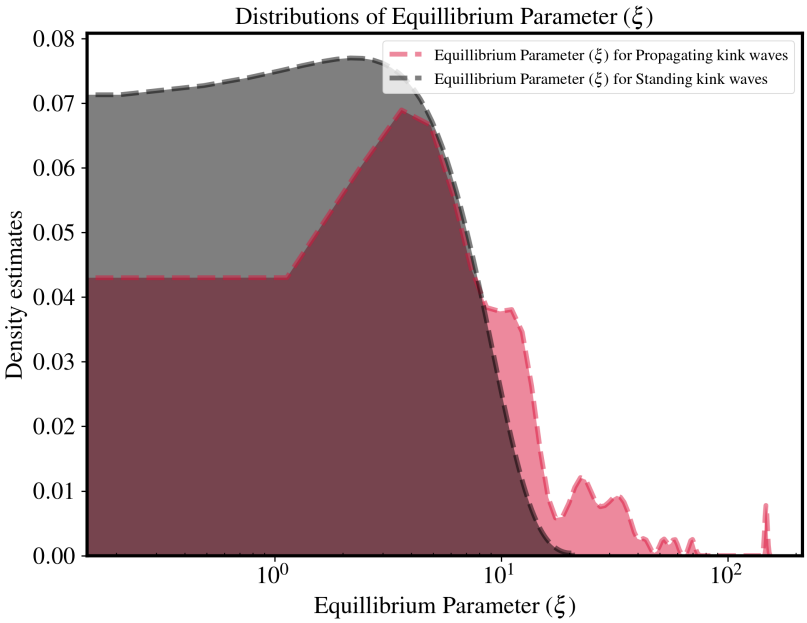

Fig. 4.7 KDE of distribution of derived equilibrium parameter ξ, after performing fitting for the observed waves. The *red* coloured bars represent the distribution of ξ for the damped propagating kink waves and the *grey* bars corresponding to the distribution of ξ for standing kink waves.

mentioned before, will be discussed separately (see Subsection 4.3.5). It can be seen that the equilibrium parameters occupy a wide range of values. The distribution illustrates that 85 % of the positive ξ observations fall in the range of (0.89,30). Hence, the propagating kink waves can be strongly damped or very weakly damped. The equilibrium parameter for the standing kink wave is calculated by taking the ratio of period and the damping time (Nechaeva et al., 2019). The median value is 9.08 and a mean value of 18.4, which is greater than that found for the standing kink modes (see discussion in Subsection 4.3.6). The implications of this result will be discussed in the Subsection 4.3.6. There are also some negative values of ξ measured, these are discussed in a later section (see Subsection 4.3.5).

The following sections deal with the relations between various parameters observed. These highlights some important properties of the waves.

4.3.2 Variation of equilibrium parameter with loop length

One of the results from the previous study (in Chapter 3) suggested a dependence between the equillibrium parameter (ξ) and the loop length. The statistical study of this chapter provides the opportunity to test this dependence. The chosen loop lengths correspond to loops being visible in the POS. This implies that the longer loops reach higher altitudes in the corona. The equilibrium parameter ξ shows a distinct behaviour with increasing loop length. It is shown in Figure 4.8. The scatter plot shows that a range equilibrium parameters are possible for all loop lengths.

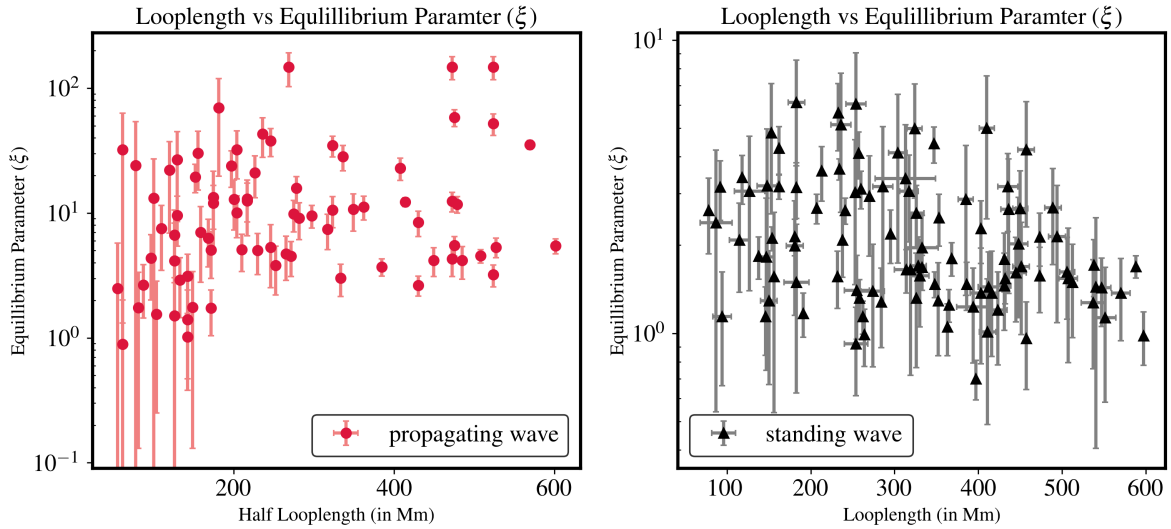

Fig. 4.8 Variation of equilibrium parameter ξ with loop length, with associated error bars. *Left:* Propagating kink waves and *Right:* Standing kink waves

However, it is possible to see a trend in the smallest possible value of ξ in the loops. It would appear that as loop length increases, their is an increase in the smallest value of ξ allowed. Smallest possible values of ξ for the loops show some increasing trend up to 200 Mm. After that, as loop length increases, the smallest value of ξ reaches a plateau region. This behaviour of the quality factor with loop length has been reported previously by Tiwari et al. (2019). However, there were only seven loops analysed in the previous study (see Chapter 3, Tiwari et al. 2019), motivating us to create a statistical study for the damping of propagating kink waves. The measured values of ξ suggest that for the longer loops that reach higher up in the corona, the quality factors increases, suggesting the propagating kink waves are subject to a reduced rate of damping, potentially due to resonant absorption. A physical explanation for the apparent decrease in damping rates can be made in terms of the changes in the plasma environment the loop is situated. Reiterating from Chapter 3, the key factor could be the density ratio between the internal and external plasmas. If the coronal loops are subjected to similar rates of heating, and the rate of chromospheric evaporation is similar, then the average density of the longer loops is likely to be less than those of shorter loops. This will lead to the density ratio (ρ_i/ρ_e) for longer loops is, on average, less than for the shorter loops, compared to the ambient plasma.

As previously discussed in Chapter 3 with relation to the observed loop length of the CoMP loops, there is the possibility that the measured loop length does not represents the true half of the loop length. In that case, the average power measured for such a short segment, the outward power will be greater than the power measured for inward propagating waves. Thus the power ratio can be artificially enhanced, giving rise to apparent greater damping. This would lead to an underestimate of ξ

compared to its true value. Hence, the observed effect of increasing ξ with height is expected to be more pronounced. The modified power ratio equation can be only applied if it is known what segment of the coronal loop is observed, based on the observation tools available to us it is almost impossible to determine the segment of loop observed.

The observed values of the damping parameters, assuming that the mechanism for damping is resonant absorption, shed some light into the dissipation of the waves into smaller scales as well. After the kink mode is converted to torsional Alfvén modes via resonant absorption, then the dissipation can occur via phase mixing, as a natural consequence of imhomogeniety of the plasma. Phase mixing leads to small-scale gradients which are formed in the resonant layer (e.g. Heyvaerts & Priest, 1983; Soler et al., 2011; Soler & Terradas, 2015; Soler & Luna, 2015; Cargill et al., 2016). The small scale KHI vortices at the boundary offer another way for the energy to dissipate (Howson et al., 2017). The larger values of damping rate implies a weaker resonant absorption. If the mode conversion via resonant absorption is happening at a lower rate then the heating due to phase mixing will also be reduced. The damping length is obtained by taking the typical values of period (P) of waves observed by CoMP (100-1000 s), and the measured phase speed (see Table 4.1). For the results in this study, the damping length (L_d) of the waves is calculated as $L_d = \xi \lambda_{prop}$, where $\lambda_{prop} = v_{ph} P$. Figure 4.9 shows the variation of damping lengths with period for three increasing values of v_{ph}. The values of damping length reported in (Hahn & Savin, 2014) would appear at the shorter end of the values we measure. Although the assumed values of propagation speed (i.e. the Alfvén speed) are not reported in the Hahn & Savin (2014) study, the energy flux equation can be inverted using the given values of energy flux (4.5×10^5 ergs cm^{-2} s^{-1}), non-thermal widths (30 km s^{-1}) and electron density (5×10^8 cm^{-3}) to find v_{ph} = 450 km s^{-1}. Hence $\xi * P$ = 220 - 400 s. The Hinode/EIS data used in their study is integrated over 60 s. Assuming that only waves with periods less than that of 60 s contribute to the line broadening in their observations (which is a very conservative assumption), then ξ = 3.7 -7.4. These values are overestimates for their study, but are broadly in agreement with the range of values presented in Table 4.1.

4.3.3 Variation of footpoint power ratio with loop length

The power ratio is fitted following the power ratio model (Verth et al., 2010; Terradas et al., 2010) using MLE. The obtained values of footpoint power ratio exhibit a decreasing trend with loop length, as shown in Figure 4.10. The shorter loop lengths exhibit higher values of footpoint power ratio (>1). This could be explained by taking into consideration the wave power injected at each footpoint might be different, possibly due to different excitation mechanism or due to difference in the

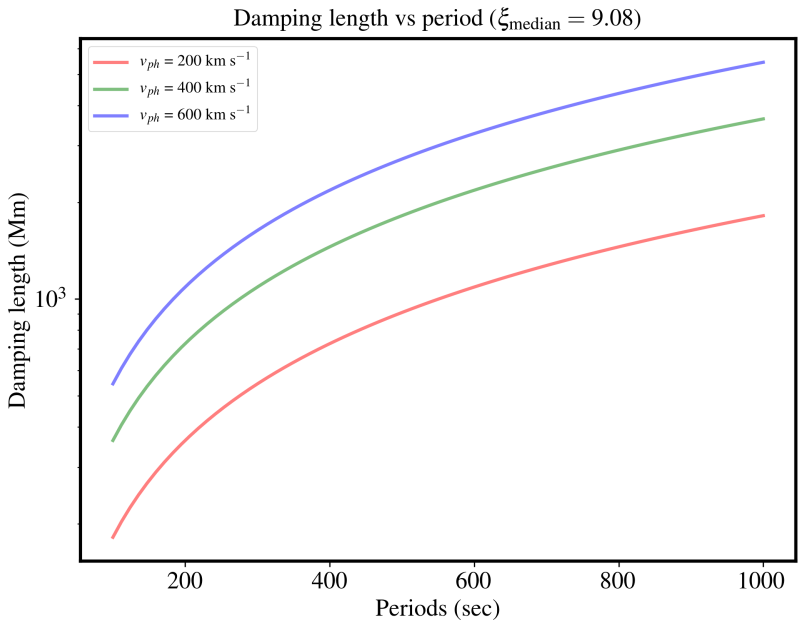

Fig. 4.9 Vdamping lengths with period for three increasing values of phase velocity(v_{ph}).

resonance between the driver and the loop footpoint motion. The trend, however, settles very quickly near the footpoint power ratio of 1, it also implies that for a majority of these loops the wave power injected at one footpoint is similar to the wave power injected at the other footpoint (Verth et al., 2010; Tiwari et al., 2019). There is a possibility that this could be an artifact of the analysis method. If the spatial wavelength of the oscillation is on the order of or greater than the length of the time-distance diagram, then there can be a leakage of power into negative/positive values of k. The wavelength of the kink modes is $v_{ph} \times P$, where v_{ph} is the phase velocity and P is the period, so for example if a wave with a period of 300s (and phase speeds of 200-600 km s^{-1}) the wave length is 60,000 - 180,00 km. Hence, the wavelengths are comparable to the loop lengths that are typically studied here. This might explain the observed deviation from 1. This deviation needs to be studied further using numerical simulations.

4.3.4 Variation of different parameters

Variation of propagation speed with loop length

The measurement of phase speed of kink waves is very important to perform coronal magneto-seismology (Edwin & Roberts, 1983). The kink speed is given by

$$v_k^2 = \frac{B_i^2 + B_e^2}{\mu_0(\rho_i + \rho_e)}, \tag{4.2}$$

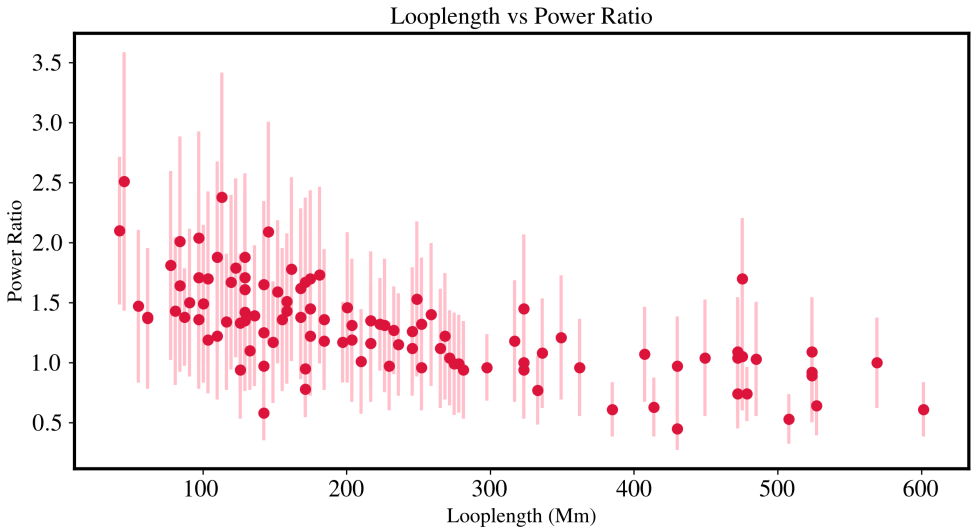

Fig. 4.10 Variation of footpoint power ratio at the loop footpoint with respect to the loop length. The red circles represent the footpoint power ratio and the corresponding errorbars are shown in pink.

Assuming the internal B_i and external B_e as the same and taking an average of the density, a lower estimate of the magnetic field can be obtained (Long, D. M. et al., 2017). From the observations, there appears to be weak dependence of the phase speed on the loop length (with a Pearson cross-correlation coefficient of 0.2) for the propagating kink waves (see Figure 4.11) and not so much for the standing kinkw aves (with a Pearson cross-correlation coefficient of 0.08). However the narrow distribution of the phase speed distribution, observed in the case of the propagating kink waves is a matter of investigation for now. One of the possible reasons is the averaging effect of the reduced spatial resolution of the CoMP instrument. The CoMP FOV averages over multiple loops visible in SDO, thus the speed that is calculated is an averaged phase speed over multiple structures in the corona.

Dependence of footpoint power ratio on phase speed

The footpoint power ratio for the propagating waves does not seem to show any dependence on the phase speed, evident from Figure 4.12. This indicates that the phase speed of the waves is independent of the wave power injected at the loop footpoints, which is expected.

Dependence of equilibrium parameter on phase speed

The equilibrium parameter and the phase speed do not show any relation as shown in Figure 4.13. This implies that the phase speed of the propagating kink wave does not affect the damping of the observed waves.

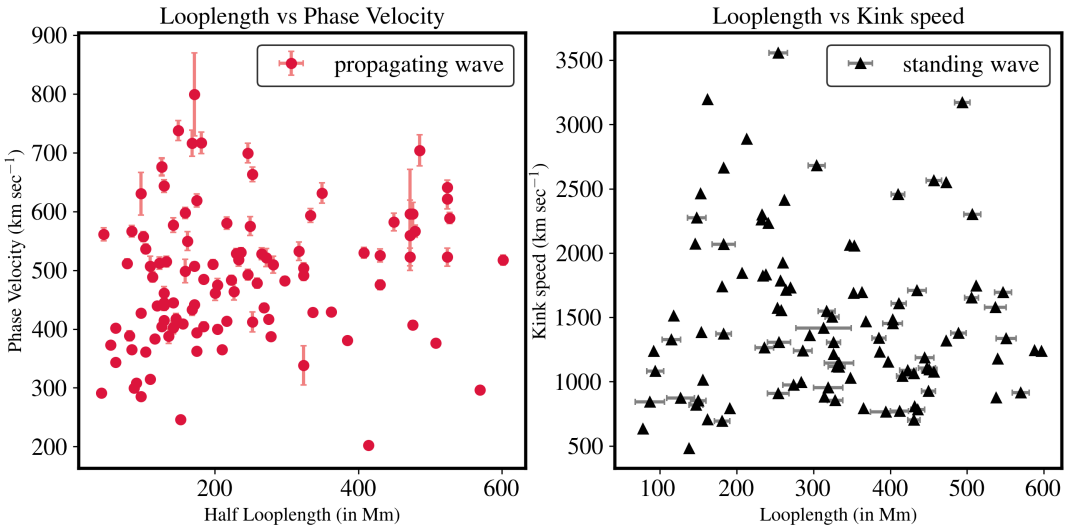

Fig. 4.11 Variation of phase speed with the loop length. The red dots correspond to the observations of the propagating kink waves. The black triangle corresponds to the observations of the standing kink waves. The error bars are shown in a lighter shade of red and black respectively for propagating and standing kink waves.

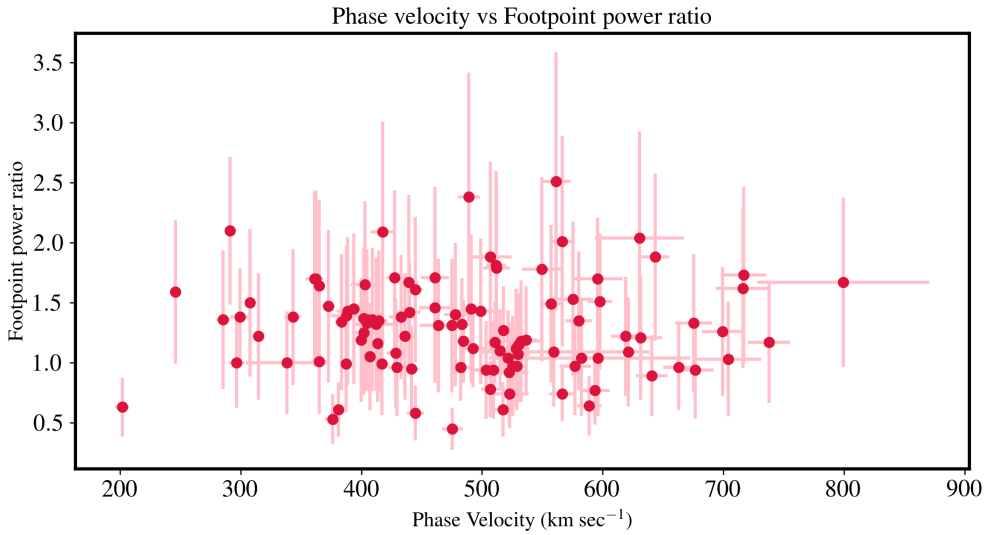

Fig. 4.12 Variation of footpoint power ratio with phase speed (red circles), with associated error bars (pink).

Dependence of equilibrium parameter on footpoint power ratio

The equilibrium parameter does not show any evidence of dependence on the footpoint power ratio, as evidenced in Figure 4.14. The rate of damping seems to be independent of the wave energy input at the loop footpoints.

4.3.5 Amplification of waves

Of the 108 loops identified and studied, 31 of them show signs of power amplification (see Figure 4.15), with a negative value of ξ. These are observed only for small

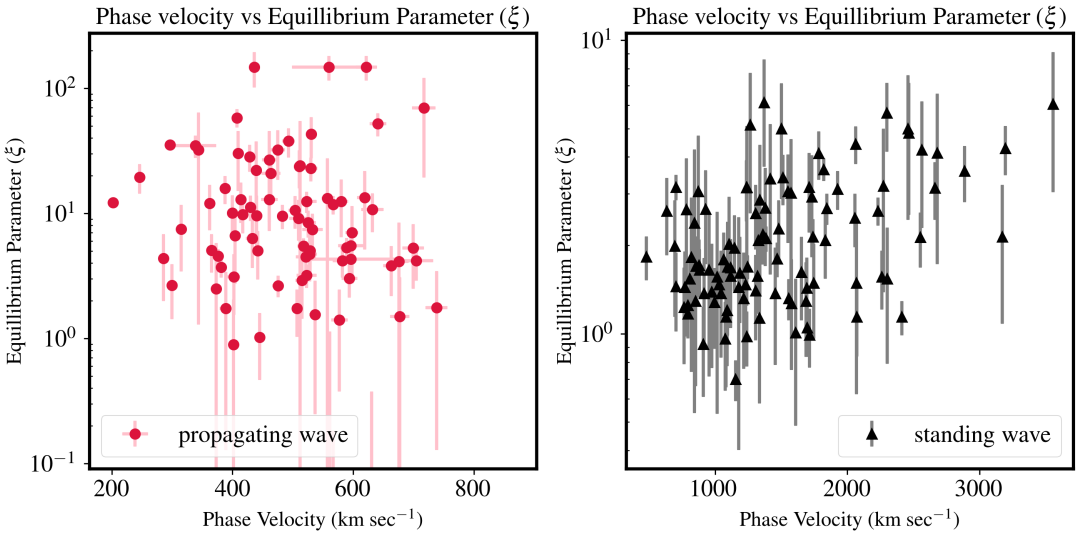

Fig. 4.13 Variation of equilibrium parameter ξ with phase speed, (associated error bars are shown in a lighter shade). *Left:* the red circle corresponds to the propagating waves. *Right:* the black triangles correspond to the standing waves.

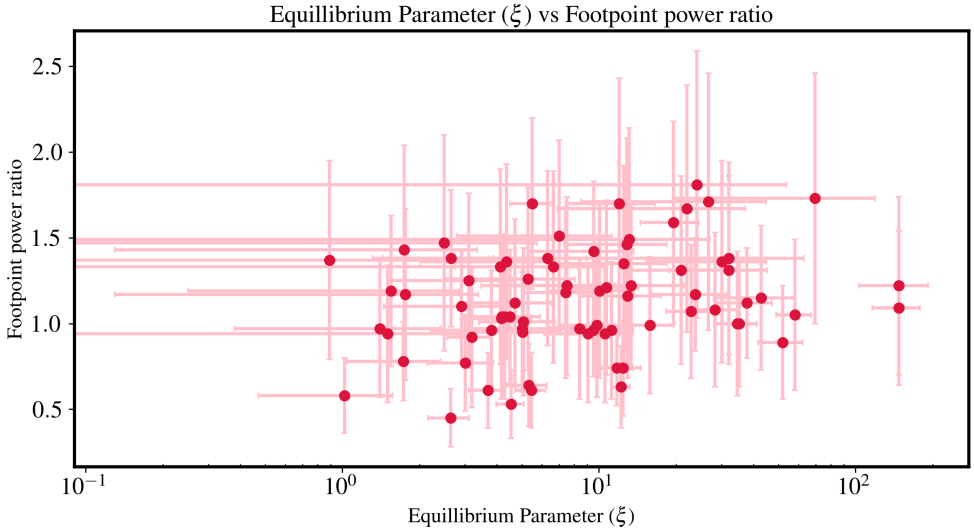

Fig. 4.14 Variation of equilibrium parameter ξ (red circle) on the footpoint power ratio length, with associated error bars (pink).

loops (less than half loop length of 350 Mm). In smaller loops flows can play an important role and can lead to amplification of waves (Soler et al., 2011; Antolin & Verwichte, 2011). The smaller loops being close to the solar disk have larger errors associated with estimating their power. The ξ of these loops seem to be dependent on the footpoint power ratio of these loops. These shorter loops with very small negative ξ need further investigation as discussed in Subsection 4.3.3.

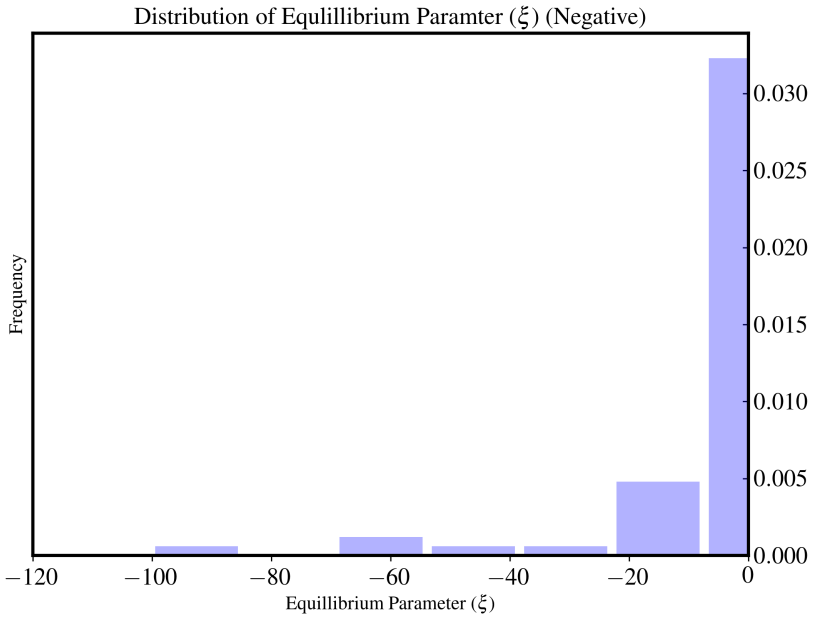

Fig. 4.15 Distribution of negative values of ξ, implying amplification of waves.

4.3.6 Comparison with the damped standing kink waves

This work utilises the large volume of available studies of damped standing kink waves to draw comparisons. The comparison focuses on the statistical work done by Goddard et al. (2016); Goddard & Nakariakov (2016); Nechaeva et al. (2019). The table generated from their work is used and modified for our study. The entries in tehe table which did not have any mention of either the damping time or the period were dropped. The equillibrium parameter was calculated from the table by taking a ratio of the damping time and the period. We also assumed all oscillations to be in the fundamental mode and calculated the kink speed as $v_{kink} = 2L/P$, where L is the looplength and P is the period.

The loop length is estimated under the assumption that the loops are close to the semicircular shape, by either measuring the projected distance between the footpoints or by the apparent height. For each of the TD map, the amplitude of the initial displacement and initial oscillation amplitude was recorded. The semi-circular approximation for the loop was taken into account thus $L = \pi R$. The data points for each oscillation were identified and a sinusoidal function of the form (assuming exponential damping)

$$y = A(\sin 2\pi t/P + \phi) \tag{4.3}$$

The initial displacement is the difference between the initial loop position and the first maximum, and the initial amplitude is defined between the first maximum and minimum. In this case, the displacement of the loop's upper edge was estimated. The kink speed which is not provided in the catalogue of Nechaeva et al. (2019) is

calculated as follows:

$$v_{kink} = \frac{\omega}{k} = \frac{2L}{P}, \tag{4.4}$$

where v_{kink} is the kink speed, L is the loop length and P is the period of the waves observed. The loop lengths along with the other parameters including calculated kink speed for the damped standing kink waves are listed in Appendix A.2. Due to missing values of damping time, period or loop length some observations from Nechaeva et al. (2019) are dropped and the total number of loops after this selection is 103 over the course of solar cycle 23.

The selected damped standing waves AIA/SDO loops have a loop length distribution akin to the loop length distribution for the propagating kink waves observation from CoMP, as seen in grey in Figure 4.4. The loop lengths measured were in between 50- 650 Mm. The most common loop length is in the range of 220-260 Mm. However, it must be noted that the loop lengths measured by CoMP and SDO/AIA are different. The CoMP instrument has a coronagraph and the observations start at 1.05 $R_{\odot}$, the loop lengths measured do not necessarily measure the footpoint of the loops, due to the limitation of instrument FOV, which varies depending on the orientation of the loops. The loop lengths measured in Table 4.1 in case of CoMP observations are half of the loop length measured. The SDO/AIA images the solar-disk, making the loop footpoints visible in the instrument field of view as opposed to the CoMP instrument (True when one observes the images in the photospheric spectral lines but then the loops are not visible as the apex lies in the corona). The projected loop length is estimated for each loop. The major radius (using the apparent loop height) or diameter (using the distance between footpoints) is measured manually, depending on the orientation of the loop with respect to the line-of-sight (LOS).

The difference in the histograms of the propagation speed and the kink speed of the propagating and the standing kink waves point towards the difference between these observations of the loops in which these two different wave modes are observed (see right panel of Figure 4.5). In case of standing waves, the kink speeds observed have mean of 1481.9 km s^{-1} which is greater than the mean value of propagation speed for propagating waves 486.7 km s^{-1}. The difference in propagation speeds reflects the difference between the magnetic field strengths in each region. The typical magnetic strength found in the active region coronal loops lies in the range of 4-30 Gauss (e.g. Nakariakov & Ofman, 2001; White & Verwichte, 2012), while the magnetic field of the quiet sun loops are estimated to be between 1-9 Gauss (Morton et al., 2015; Long, D. M. et al., 2017)[1] The differences in the measured speeds could

[1]It should be noted that the magnetic field measurements obtained by coronal magneto-siesmology provide an underestimate of the magnetic field values (Verwichte et al., 2013a).

potentially be explained by this difference in the strength of magnetic field at the location of the footpoints.

A comparison of the distributions of equilibrium parameters for the standing and propagating waves is also provided, which is shown in Figure 4.7. The standing waves (ξ_{median} 1.8) have smaller values of quality factor implying that the standing kink waves are damped at a faster rate than the propagating waves (ξ_{median} 9.08). In case of loops with a footpoint in the active region the loops undergo increased heating. The greater the heating, larger contribution of chromospheric evaporation is expected (Aschwanden, 2004). Moreover, the larger density of active region loops can be inferred from EUV observations, where the AR loops appear significantly brighter than quiescent loops (as the intensity is proportional to ρ^2). The measured ξ values for the standing waves are evenly distributed with a mean value of 2.28 and a median value of 1.8. The active regions have been modelled to understand the role of resonant absorption and phase mixing in the thermal equillibrium of these loops. The active region environment (larger values of density contrast and smaller values of ξ) show that the loop heating via phase mixing appears to be insufficient for balancing the radiative losses (De Moortel & Nakariakov, 2012; Howson et al., 2019; Prokopyszyn et al., 2019; Howson et al., 2020), which implies that in case of quiet Sun loops (smaller values of density contrast and larger values of ξ), the wave heating would not be sufficient to support the radiative losses.

The kink speed of the standing kink waves show a positive correlation with the quality factor. A linear trend is observed between the phase speed and equilibrium parameter with a Pearson correlation coefficient of 0.56 (see Figure 4.13). The rate of damping decreases depends on the measured kink speed of the waves, this might be due to non-linear effects (Goddard et al., 2016).

4.4 Conclusion

This work provides a statistical study of the damped propagating kink waves. This is the first such attempt to study the statistical properties of damped propagating kink waves. This work also does a comparative study with the long observed standing kink waves and highlights some stark differences between the propagating and standing kink waves. These differences occur most likely due to the difference in the magnetic environment of these observed loops. The standing kink waves have been reported predominantly in loops that have at least one footpoint in the active region, however, the propagating kink waves have been reported to be ubiquitous in the solar corona. The excitation mechanism of these waves is also starkly different. The origin of the standing kink waves is found to be the flaring activity nearby however the ubiquity of the propagating kink waves hint a potential global driver (Morton et al., 2019).

The study gives further credibility to the notion of frequency-dependent damping of the propagating kink waves and resonant absorption as the damping mechanism. The data, however, suffers from averaging effects due to the poor spatial sampling of the CoMP instrument. The LOS effect has a significant effect on the observation of these waves, numerical simulations by (De Moortel & Pascoe, 2012; Pant et al., 2019) have shown this discrepancy reducing the energy budget of wave damping by 2-3 orders of magnitude. This study further proves the damping behaviour of loops with loop length or the height in the corona. As the loop length increases (loops reaching higher altitudes in the corona) the rate of damping decreases verifying claims of Tiwari et al. (2019). In case of standing waves an opposite behavior is observed from the study of damped standing kink waves, in contrast to claims by Verwichte et al. (2013b), where they found that the equilibrium parameter increases with the increased looplength. The study also reports the amplification of waves (amplification is suggested only for the negative ξ), the source of which are unclear at this time. The measured values of ξ suggests a decrease in the heating due to phase mixing. The damping length of the propagating kink waves is also calculated, which is found to be broadly comparable to the the previous estimates of (Hahn & Savin, 2014). This study raises doubts about wave heating as an efficient heating mechanism for coronal loops in the quiet Sun. The larger damping length (L_d) and larger values of measured (ξ) makes the dissipation of energy via phase mixing less effective in the quiet sun atmosphere. Further studies, especially 3D MHD simulations in quiet Sun conditions are needed to understand the role of resonant absorption in the wave damping of propagating transverse waves. These full numerical 3D-MHD simulations can shed the light on the dependence of flows and the interplay between the density and the magnetic field on the behaviours of resonant absorption in these different family of coronal loop observations.

Chapter 5

Conclusion and Future Work

5.1 Conclusion

This thesis starts with the discussion of the Sun and the solar atmosphere. As discussed previously in Chapter 1, understanding the solar coronal heating is one of the holy grails of solar physics and of plasma physics. The long-standing problem has motivated some very elegant studies conducted to understand the underlying heating mechanism of the solar corona. The various coronal heating models can be broadly classified into two main categories, a) reconnection-based models and b) wave based models. The recently observed ubiquity and diversity of the MHD waves in the solar corona present a strong case to study these wave modes. MHD waves could provide part of the solution to the long-standing coronal heating problem. Section 1.7 discusses the various MHD wave modes observed so far.

Of these MHD waves, the transverse MHD waves are of particular interest due to their ability to carry large amounts of energy, and thus potentially to contribute significantly to coronal heating (e.g. Uchida & Kaburaki, 1974; Wentzel, 1974; McIntosh et al., 2011b). The transverse waves were first observed in the solar corona (Aschwanden et al., 1999; Nakariakov et al., 1999) in active region loops following flaring activity. The observation of these waves revealed periods of 5-3 minutes and rapid damping, and led to various follow-up studies to explain the rapid damping of these waves. The damping of these large amplitude waves is thought to be explained by the mechanism of resonant absorption (Goossens et al., 2002; Aschwanden et al., 2003; Van Doorsselaere et al., 2004; Goossens et al., 2011). Resonant absorption (and mode coupling), is an ideal candidate for energy transfer between different wave modes (Ionson, 1978; Hollweg, 1984). In the presence of density inhomogeneity, resonant absorption predicts that the global kink mode can resonantly couple with azimuthal Alfvén waves. The global kink mode, which consists of a purely transverse displacement of the loop, is transferred to the local azimuthal Alfvén waves at the resonance layer where the kink speed matches the Alfvén speed. The 3D MHD numerical simulations (e.g. Pascoe et al., 2012; De Moortel & Nakariakov, 2012) provide evidence for the efficient and robust energy transfer via resonant absorption.

The propagating kink waves were discovered in the seminal paper by Okamoto et al. (2007); Tomczyk et al. (2007); Tomczyk & McIntosh (2009). These observations which were interpreted as propagating kink waves (Van Doorsselaere et al., 2008) and were found to be ubiquitous throughout the corona, as LOS Doppler velocity fluctuations. The damping mechanism for these waves was also thought to be resonant absorption (e.g. Terradas et al., 2010; Verth et al., 2010). Phase mixing via resonant absorption can explain the dissipation of this energy in the corona.

The study of MHD waves also complement the magnetic reconnection models by providing a measure of the magnetic field in the corona, using techniques of coronal magneto-seismology. Coronal magneto-seismology is at its infancy, there have been

several developments on trying to estimate the magnetic field measurements, the TRACE observation (Aschwanden et al., 1999) paved the way for the development of coronal magneto-seismology. However, the standing kink waves were found to be always associated with some low-coronal eruptions (e.g.flares) and thus posed a difficulty in getting continuous measurements of coronal parameters (Nakariakov & Ofman, 2001; Nakariakov, 2003). This problem can be mitigated with the discovery of ubiquitous propagating kink waves (Yang et al., 2020). The propagating kink waves have made the measurement of the strength of magnetic field possible for quiet Sun corona (Long, D. M. et al., 2017). The measurement of magnetic field in the corona (plasma $\beta \ll 1$) is crucial for understanding the physical processes on the sun in general and solar corona in particular. The LOS magnetic field of a flaring coronal loop has been measured by Kuridze et al. (2019), fairly recently. They report coronal magnetic field strengths up to 350 G at heights reaching 25 Mm above the solar limb, with implications for our understanding of the Sun. The values of magnetic field strength measured by them are considerably higher than previous estimates for the coronal fields (Nakariakov & Verwichte, 2005; Tomczyk et al., 2007). The low values reported by previous studies is attributed to the effects of spatial and temporal resolution with an underestimation of up to 80% for previous low resolution studies to determine the magnetic field values.

The thesis outlines the various types of waves and focuses on the study of propagating kink MHD waves in the solar corona. The focus of this thesis lies with the propagating kink waves observed using the CoMP instrument (Tomczyk et al., 2007; Tomczyk & McIntosh, 2009; Morton et al., 2015, 2016; Tiwari et al., 2019).

In the first study, the method to analyse the Doppler velocity image sequences is presented in full detail (see Chapter 3). The coherence based method to track the propagation of waves in the solar corona is found to be particularly well suited to the study of propagating kink waves. The first observational evidence for the damping of propagating kink waves via resonant absorption was provided in the study of Verth et al. (2010). However, as it is shown in Subsection 3.3.4, the statistics used in that study was inadequate and biased. Motivated by this, in Chapter 3, the statistics of the power ratio (ratio of two χ distributions) is discussed for the first time (Tiwari et al., 2019). The likelihood function is also derived using the derived probability density function $(p.d.f)$. The results of Verth et al. (2010), that the damping is frequency dependent was also confirmed by the study. It is also noted that energy injected in the loop at the footpoint is similar, which was also previously reported in (Verth et al., 2010). This along with the ubiquity of the propagating kink waves support the excitation of these waves via a global driver. There have been various studies to understand how the photospheric motion can lead to waves in the loops observed in the solar corona (Jain et al., 2009, 2011; Hindman & Jain, 2008). Studies

by Morton et al. (2019) suggest *p*-mode as a possible driving mechanism for these waves. The result in the study also highlights the importance of the loop geometry and the changes in the loop plasma environment. The damping of these waves are found to be frequency dependent, consistent with the resonant absorption as the damping mechanism (Verth et al., 2010) for propagating kink waves. The study find that the damping rate decreases for longer loops that reach higher up in the solar corona, which means that the longer loops are damped at a decreased rate. The observations consisted of analysis of just seven wave-tracks (loops) which is not a reasonable statistical size to comment on this behaviour. This necessitates the need for studying these waves in a statistical manner which is achieved by Chapter 4. The limitations of the CoMP observations (namely the poor spatial sampling) and the relevance of accounting for flows in the study of damping of waves in solar corona is also highlighted.

The work presented in Chapter 3 motivates the need for a large scale statistical study of damped propagating kink waves. This is explored in Chapter 4, where a total of 108 loops were observed between 2012-2014. To be consistent with the study discussed in Chapter 3, the same analysis techniques were adopted for the statistical analysis of damped propagating kink waves. This study provides an understanding of statistical properties of damped propagating kink waves and further confirms the results from Chapter 3. In addition to this, some interesting new findings are also reported. The results reaffirm the role of resonant absorption as the damping mechanism for the propagating kink waves. The rate of damping was found to be decreasing for longer loops that reach higher up in the solar corona, consistent with the results from Tiwari et al. (2019). This difference in the damping rates could be attributed to the difference between the density of the plasma inside and outside the coronal loops. Under the assumption that the coronal loops are subjected to similar rates of heating, and the chromospheric evaporation rate is also similar, then the average density of the longer loops is likely to be less than those of shorter loops. This leads to the density ratio (ρ_i/ρ_e) for longer loops to decrease than for the shorter loops, compared to the ambient plasma.

One of the other key features of this study was the comparative study of damped propagating kink waves and damped standing kink waves. The composed table of damped propagating kink waves parameters (see Table 4.1) are compared to the damped standing kink waves parameters (see Table A.2). The data for the damped standing waves was taken from the study by Nechaeva et al. (2019). The analysis for damped standing waves analyses 101 loops across the solar cycle 24, using data from AIA/SDO. The standing kink waves are found to be associated by a low coronal eruptive event (Zimovets & Nakariakov, 2015), hinting at the excitation mechanism of these standing waves. The equilibrium parameters, phase speed are studied across the distributions of loop length for both the standing and propagating kink waves.

The rate of damping varies in between these two different modes of kink waves. By comparing the Equilibrium parameter (quality factor) of these two modes of kink waves, it is found that for loops with similar loop lengths, the rate of damping is significantly higher in case of standing kink waves as compared to the propagating kink waves. The median of the quality factor is 9.08 and 1.8 for damped propagating and damped standing kink waves, respectively. It is also observed that in case of standing kink waves the rate of damping increases with increasing loop lengths which is contrary to the observation for the propagating kink waves. This could be due to the difference in the excitation mechanism of these waves, but further studies needs to be done to understand this behaviour. The differences between the phase speed of propagating kink waves and the kink speed of standing kink waves become evidently similar from the distribution for these two waves. It also highlights the difference between these two kinds of waves. On one hand the kink speed of the standing waves can go up to a few thousands of km s^{-1} and on the other the speed for propagating kink waves are distributed around 600-800 km s^{-1}. The phase velocity depends on the magnetic field of the plasma, which might be able to explain the vastly different values of phase velocities measured for the propagating and standing kink waves. It should also be noted that the excitation of the standing kink waves in the coronal loops due to eruptive processes in corona makes them biased and very selective as opposed to the ubiquitous propagating kink waves. The catalogue of the propagating kink waves, provide us with another tool for coronal magneto-seismology independent of eruptive processes on the Sun. This is also important as the direct magnetic field measurement of quiet Sun corona is very difficult, the observations and understanding of damping of the propagating kink waves can provide a diagnostic tool to study quiet sun coronal magnetic fields.

The damping length (L_d) for propagating kink waves is also estimated, and found to be broadly consistent with previously reported values of 100-200 Mm (Hahn & Savin, 2014). Using the data provided in the Hahn & Savin (2014) study ξ is calculated and found to be in between 3.7 -7.4. The values obtained are overestimates for their study, but are broadly in agreement with the range of values obtained in the statistical study.

The comparative study of damping of standing kink waves, which are found in loops with footpoints in the active region (strong magnetic field) and the propagating kink waves found in the loops with footpoints assumed to be in the inter-network regions (weak magnetic field) also helps us understand the heating of these loops. 3D MHD simulations of heating of active region loops (De Moortel & Nakariakov, 2012; Howson et al., 2019; Prokopyszyn et al., 2019; Howson et al., 2020) show that the loop heating via phase mixing appears to be insufficient for balancing the radiative losses. The difference between the quality factor of standing kink waves (representing active region environment, larger values of density contrast and smaller

values of ξ) and propagating kink waves (representing quiet Sun region environment, lower values of density contrast and larger values of ξ) implies that in case of quiet Sun loops the wave heating would not be sufficient to support the radiative losses, and thus a different heating mechanism is at play.

Lastly another interesting feature from this study (see Chapter 4) is the observation of amplification of waves. Out of 108 observed loops, 31 loops have a negative value of equilibrium parameter (ξ), which implies that these waves were amplified. The amplification of these waves is of unknown origin. However, some of the statistical properties might be helpful in explaining the origin of this amplification. The equilibrium parameter (ξ) for these observations seem to be dependent on the footpoint power ratio of these loops as seen in Figure 5.1. The amplification is typically observed in smaller loops.There is a possibility that this could be an artifact of the analysis method. Further studies using numerical simulations are needed to explain the amplification of these waves.

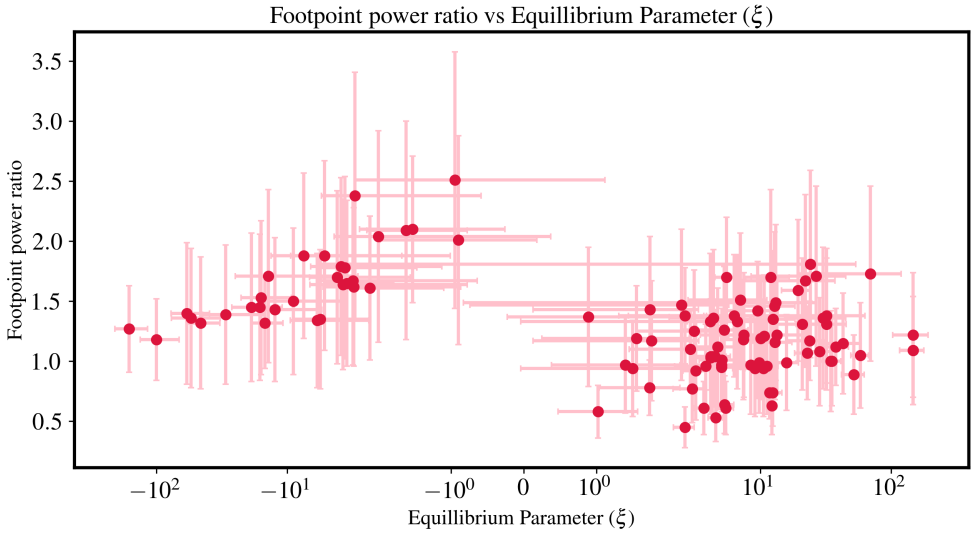

Fig. 5.1 Variation of equilibrium parameter with footpoint power ratio, in case of propagating kink waves. the positive X-axis shows the damped propagating kink waves and the negative X-axis shows amplified kink waves.

The thesis furthers our understanding of the damping of waves in the solar atmosphere, with the implications for coronal magneto-seismology and wave heating of the solar coronal loops and the solar corona.

5.2 Future work and questions

Within this thesis the analysis method for studying propagating waves in the solar corona is developed. The interesting properties of the decrease in the damping rate with the increase in loop length is presented and a possible explanation is provided. There are however some unanswered questions, such as a) What is the source of

these ubiquitous wave phenomenon? b) The energy budget of these waves in the corona? These are important questions in their own merit and require future studies.

Some of the studies that can contribute to our understanding of the solar in particular and stellar atmospheres in general are briefly discussed. These studies can benefit from the work done in this thesis. Some future expectations are also discussed.

5.3 Open questions

5.3.1 Energy budget of corona

The various studies however have huge discrepancies in the energy budget for example Tomczyk et al. (2007) suggested an energy budget that is several orders of magnitude too small to account for coronal heating. However using the SDO/AIA observation, McIntosh et al. (2011b) suggests that the observed small amplitude oscillatory displacements contain sufficient energy to account for the heating requirements of the quiet Sun and coronal holes ($1-2\times10^5$ erg cm^{-2} s^{-1}). However, in active region loops the energy budget is estimated to be at least an order of magnitude too small (10^5 erg cm^{-2} s^{-1} vs 2×10^5 erg cm^{-2} s^{-1} needed to account for the heating of coronal loops. This vast discrepancies could arise from the the effects of superposition of Doppler velocities. This superposition can be a result of integration along the line of sight and/or a result of lower spatial sampling by instruments. This superposition results in a significant proportion of the wave energy flux being "hidden" in the large (observed) nonthermal line widths (McIntosh & De Pontieu, 2012; Gupta et al., 2019). 3D numerical Simulations to explain the "hidden" energy suggest (De Moortel & Pascoe, 2012; Pant et al., 2019) that the observed wave energy is only 0.2%-1% of the true wave energy, which explains the 2-3 order-of-magnitude energy discrepancies. In addition, The interpretation of wave mode from the observations of waves is not an easy task, this further complicates the estimation of energy budget (Goossens et al., 2013). Complications also arises due to the highly active nature of the solar atmosphere. The presence of wave energy does not guarantees local heating due to the various phenomena such as wave damping and dissipation. The Parker Solar Probe (PSP) and and the SOlar Orbitor along with new generation of large aperture telescopes such as DKIST have hopes of the solar physicists up to understand the energy budget of solar corona via the study and validation of both wave and reconnection based heating models.

5.3.2 Wave damping and dissipation

The mechanism for damping of these waves is considered to be either resonant absorption (Verth et al., 2010; Terradas et al., 2010) or mode coupling (Pascoe et al., 2012; De Moortel et al., 2016). Mode coupling and resonant absorption can aid in transferring energy from one wave mode to another. This might be observed as rapid damping of observable transverse oscillation. However, the presence of damping does not necessarily implies dissipation (and hence heating) on the same rapid timescale. The heating of solar plasma requires the wave energy to be transferred into the kinetic energy of plasma. However, the dissipation is inefficient in the the solar atmosphere unless very short spatial scales are involved. This is naturally achieved by the by phase mixing of Alfvén waves. Phase mixing leads to small-scale structures forming in the resonant layer (boundary of the loops) (Soler et al., 2011; Soler & Luna, 2015; Soler & Terradas, 2015; Cargill et al., 2016; Howson et al., 2017). The existence of small scale structures in the boundary layers of the loops (flux tubes) was predicted by Heyvaerts & Priest (1983). The small scale structures that have been observed in numerical simulations and satisfy the conditions of wave dissipations at small-scales are the Transverse Waves Induced Kelvin-Helmholtz (TWIKH) rolls (Antolin et al., 2014; Okamoto et al., 2015; Antolin et al., 2015; Antolin et al., 2017). Kelvin-Helmholtz Instability (KHI) benefits significantly from the resonance, from which it extracts kinetic energy. (Karampelas et al., 2017) has shown that resonant absorption is key to energize TWIKH rolls and spread them all over the loop. These KH instability leading to smaller-scale structures have also been analytically and numerically predicted from the shear flow of other transverse waves, such as torsional Alfvén waves (Zaqarashvili & Erdélyi, 2009). The DKIST (Tritschler et al., 2016) has created a buzz in the scientific community about observations of these small scale structures using the vastly improved spatial resolution of the instruments. The energy discrepancy between different observations of propagating transverse waves is an perplexing question. The resolved measurements of the propagating transverse waves is provided by the chromospheric and transition region observations using imaging data from the Solar Optical Telescope (SOT) on board Hinode (De Pontieu et al., 2007) and the AIA/SDO observations (McIntosh et al., 2011b). These studies reported waves with amplitudes of 20 km s^{-1} suggesting the energy flux of 100-200 W m^{-2} to accelerate and balance the fast solar wind and balance radiative losses in the quiet corona. However the coronal counterpart of this propagating transverse waves was seen using Doppler velocity data from CoMP (e.g. Tomczyk et al., 2007; Tomczyk & McIntosh, 2009; Morton et al., 2016). The measured Doppler velocities however suggest an energy flux of 0.01 W m^{-2}, a reduction of 3-4 orders of magnitudes. The CoMP data also provides measures of coronal line widths, providing estimates of the non-thermal component that are comparable to

previously reported values. There have been various studies to measure the non-thermal components using the coronal line widths data (e.g McIntosh & De Pontieu, 2012; Hahn et al., 2012; Gupta et al., 2019). The studies have demonstrated an increase in the amplitude of non-thermal line-widths as one radially moves away from the solar disk. The line width observed in coronal holes by (e.g Hahn & Savin, 2014; Morton et al., 2015) vary from 30-60 km s^{-1} for distances up to 1.4 $R_{\odot}$. These observations provide evidence for the role of these propagating kink waves in the acceleration of the solar wind.

5.4 Future work

One of the limitations as highlighted throughout Chapter 3 and Chapter 4 is the lower spatial sampling and the effect of line of sight integration effect on the observation and measurement of wave properties in the solar corona. The increasingly complex and detailed 3D MHD numerical simulations can provide a pivotal role in understanding and interpreting these observations. The validity of these numerical simulations as already been established (e.g. Reale, 2010; De Moortel et al., 2016; Pascoe et al., 2016b, 2017, 2018). To this end one of the future work is to understand and validate the model that is used to interpret the damping of propagating kink waves (Equation 1.34). A numerical simulation has been designed study the influence of spatial averaging on observations of damping in propagating kink waves and to validate the analysis method developed as part of this thesis. The 3D multi-stranded coronal loop (MHD) simulations with colleagues from KU Leuven are performed, to study the damping behaviour in forward modelled loops. The numerical setup has a dimensions of 200 Mm $\times$ 5 Mm $\times$ 5 Mm (See Figure 5.2), with multiple random Gaussian density enhancements across the straight magnetic field, while along the magnetic field the plasma was homogeneous. The obtained simulation was forward modelled using the FoMo[1] tool (Van Doorsselaere et al., 2016). The forward modelled loops were 'degraded' to match the CoMP spatial resolution of 4.5″. The same steps as performed in Chapter 3 and Chapter 4 can then be used to estimate the damping in the simulated loops and the same can be obtained for the high resolution simulated loops. This can provide a test for the analysis method used in this thesis at the same time.

The results from Chapter 4 also highlight the need for performing simulations for quiet Sun conditions to understand the role of wave damping and dissipation in the heating of the quiet Sun coronal loops and the solar corona.

The exponential damping profiles is assumed in the study throughout, however there some evidences supporting a Gaussian profile for damping, especially during

[1] FoMo

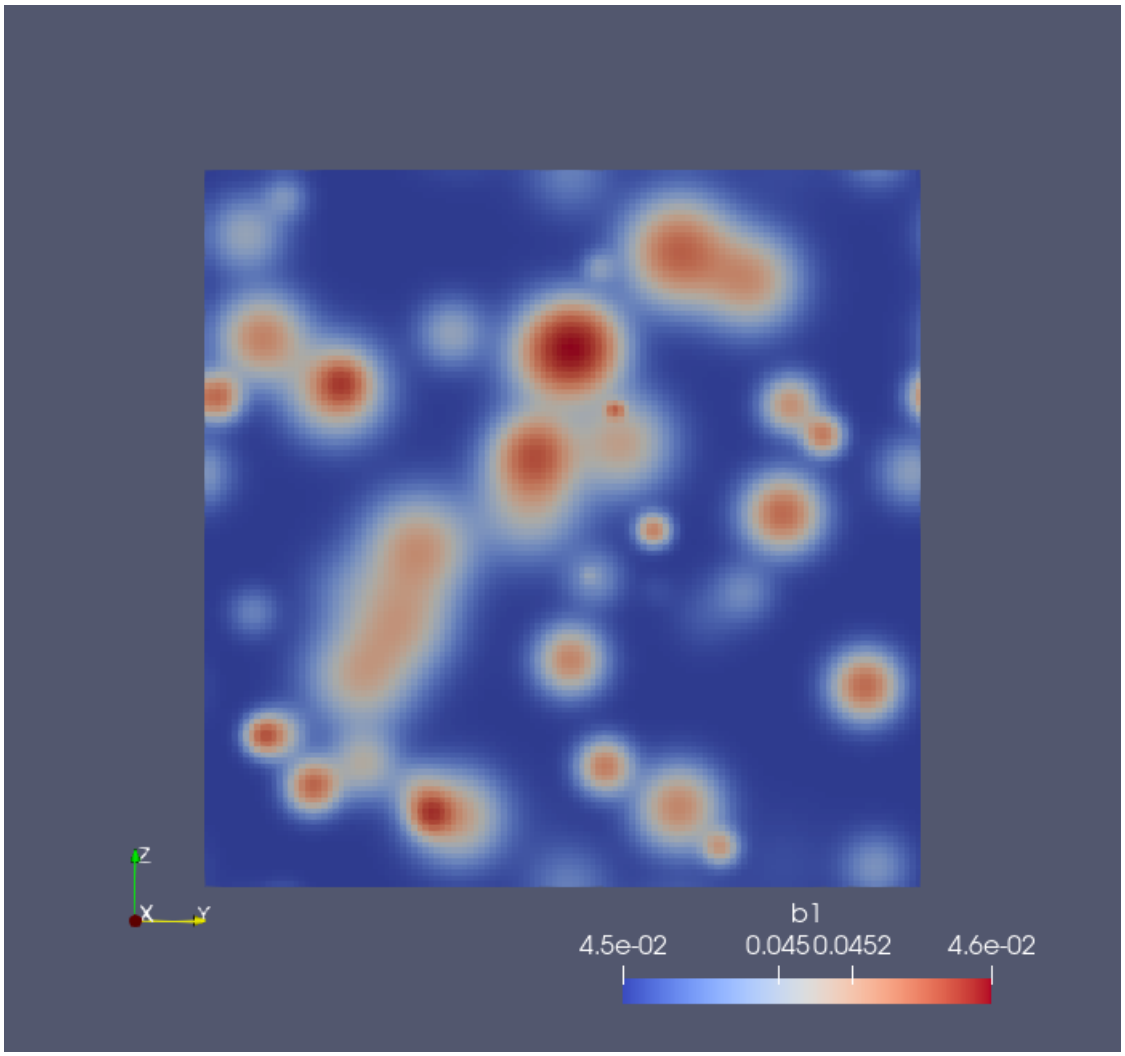

Fig. 5.2 Flux tubes in the multi-stranded 3D numerical simulation setup. The red dense regions correspond to the fluxtubes and the blue region corresponds to the background ambient medium.

the initial phases of damping (e.g. Pascoe et al., 2016b, 2017, 2018). Further analysis should take these into consideration. The poor spatial samping of CoMP instrument limits the possibilities of inferences from the data, which has been discussed in Chapter 3 and Chapter 4, it has been shown that the line-of-sight integration has a significant impact on observations (De Moortel & Pascoe, 2012). The DKIST, which boasts to be the world's largest solar telescope with a 4-m aperture has the potential to mitigate this issue. DKIST begins science operation from July 2020. The CoMP instrument is being upgraded as well which will improve the spatial sampling of the instrument (called uCoMP). This upgrade provides near constant ground based coverage of the solar corona. These improvements will help address the questions that could not be addressed in this thesis and this can be used to constrain the results regarding damping of the waves further. The recent study by Morton et al. (2019) suggest the excitation of these waves by a contribution of solar p-modes,

the connection between the observed propagating kink waves and the solar wind warrants a study by itself.

Future studies should also try to include the role of background flow to try to measure the background flow speeds in coronal loops in the solar corona. The work in the thesis can also be used to estimate the magnetic field of the corona and create a magnetic field map of the solar corona.

The coming decade is going to be particularly exciting as DKIST observations would coincide the first encounter missions aimed at mapping the physical conditions in the vicinity of the Sun, the NASA/PSP (launched, August 2018) and the ESA/NASA mission Solar Orbiter (launched, February 2020). DKIST, PSP, and Solar Orbiter will form an unprecedented solar corona and inner heliospheric campaign addressing the long standing problems of coronal heating and acceleration of solar wind. These observations will also further our understanding about how stars create and maintain their magnetic environments.

References

Afanasyev, A., Karampelas, K., & Van Doorsselaere, T. 2019, ApJ, 876, 100

Akasofu, S. I. 1981, SSRv, 28, 121

Anfinogentov, S., Nisticò, G., & Nakariakov, V. M. 2013, A&A, 560, A107

Anfinogentov, S. A., Nakariakov, V. M., & Nisticò, G. 2015, A&A, 583, A136

Antolin, P., De Moortel, I., Van Doorsselaere, T., & Yokoyama, T. 2016, ApJL, 830, L22

Antolin, P., Moortel, I. D., Doorsselaere, T. V., & Yokoyama, T. 2017, The Astrophysical Journal, 836, 836

Antolin, P., Okamoto, T. J., De Pontieu, B., et al. 2015, ApJ, 809, 72

Antolin, P. & Verwichte, E. 2011, ApJ, 736, 121

Antolin, P., Yokoyama, T., & Van Doorsselaere, T. 2014, ApJL, 787, L22

Appourchaux, T. 2003, A&A, 412, 903

Arlt, R. & Vaquero, J. M. 2020, Living Reviews in Solar Physics, 17, 1

Aschwanden, M. J. 2004, Physics of the Solar Corona. An Introduction (Praxis Publishing Ltd)

Aschwanden, M. J. 2019, New Millennium Solar Physics, Vol. 458

Aschwanden, M. J., de Pontieu, B., Schrijver, C. J., & Title, A. M. 2002, SoPh, 206, 99

Aschwanden, M. J., Fletcher, L., Schrijver, C. J., & Alexander, D. 1999, ApJ, 520, 880

Aschwanden, M. J., Nightingale, R. W., Andries, J., Goossens, M., & Van Doorsselaere, T. 2003, ApJ, 598, 1375

Astropy Collaboration, Price-Whelan, A. M., Sipőcz, B. M., et al. 2018, AJ, 156, 123

Astropy Collaboration, Robitaille, T. P., Tollerud, E. J., et al. 2013, A&A, 558, A33

Ayres, T., Uitenbroek, H., Cauzzi, G., et al. 2009, The Solar Chromosphere: Old Challenges, New Frontiers, in astro2010: The Astronomy and Astrophysics Decadal Survey, Vol. 2010, 9

Banerjee, D., Erdélyi, R., Oliver, R., & O'Shea, E. 2007, SoPh, 246, 3

Barnes, A. 1979, Reviews of Geophysics and Space Physics, 17, 596

Barret, D. & Vaughan, S. 2012, ApJ, 746, 131

Basu, S., Chaplin, W. J., Elsworth, Y., New, R., & Serenelli, A. M. 2009, The Astrophysical Journal, 699, 1403

Bergmann, U. & Riisager, K. 2002, Nuclear Inst. and Methods in Physics Research, A, 489, 489

Bevington, P. R. & Robinson, D. K. 2003, Data reduction and error analysis for the physical sciences

Bhowmik, P. & Nandy, D. 2020, Prediction of Sunspot Cycle 25: Based on a Century-scale Data-driven Magnetic Field Simulations, in AAS/Solar Physics Division Meeting, Vol. 52 of AAS/Solar Physics Division Meeting, 209.02

Bohlin, J. D. & Sheeley, N. R., J. 1978, SoPh, 56, 125

Borrero, J. M. & Ichimoto, K. 2011, Living Reviews in Solar Physics, 8, 4

Bray, R. J., Cram, L. E., Durrant, C., & Loughhead, R. E. 1991, Plasma Loops in the Solar Corona

Browning, P. K. & Priest, E. R. 1984, A&A, 131, 283

Burroughs, W. J. 2007, Climate Change: A Multidisciplinary Approach, 2nd edn. (Cambridge: Cambridge University Press)

Cally, P. S. 2003, SoPh, 217, 95

Cally, P. S. 2017, MNRAS, 466, 413

Cargill, P. J., De Moortel, I., & Kiddie, G. 2016, ApJ, 823, 31

Carrington, R. C. 1858, MNRAS, 19, 1

Chandran, B. D. G., Perez, J. C., Verscharen, D., Klein, K. G., & Mallet, A. 2015, ApJ, 811, 50

Chatterjee, S., Banerjee, D., & Ravindra, B. 2016, The Astrophysical Journal, 827, 827

Christensen-Dalsgaard, J. 2002, Reviews of Modern Physics, 74, 1073

Cooley, J. W. & Tukey, J. W. 1965, Mathematics of computation, 19, 19

Cowling, T. G. 1966, QJRAS, 7, 121

Cox, A. N., Livingston, W. C., & Matthews, M. S. 1991, Solar interior and atmosphere

Cranmer, S. R. 2018, ApJ, 862, 6

Cranmer, S. R. & Van Ballegooijen, A. A. 2005, ApJS, 156, 265

Cranmer, S. R., Van Ballegooijen, A. A., & Edgar, R. J. 2007, ApJS, 171, 520

de La Torre, L., Gimeno, L., Añel, J. A., & Nieto, R. 2007, Advances in Atmospheric Sciences, 24, 191

De Moortel, I. 2005, Royal Society of London Philosophical Transactions Series A, 363, 2743

De Moortel, I. & Brady, C. S. 2007, ApJ, 664, 1210

De Moortel, I., Falconer, I., & Stack, R. 2020, Astronomy and Geophysics, 61, 2.34

De Moortel, I., Ireland, J., & Walsh, R. W. 2000, Astronomy & Astrophysics, 355, L23

De Moortel, I. & Nakariakov, V. M. 2012, Philosophical Transactions of the Royal Society of London Series A, 370, 3193

De Moortel, I. & Pascoe, D. J. 2012, ApJ, 746, 31

De Moortel, I., Pascoe, D. J., Wright, A. N., & Hood, A. W. 2016, Plasma Physics and Controlled Fusion, 58, 014001

De Pontieu, B., McIntosh, S. W., Carlsson, M., et al. 2007, Science, 318, 318

DeForest, C. E. & Gurman, J. B. 1998, ApJL, 501, L217

Delaboudinière, J.-P., Artzner, G. E., Brunaud, J., et al. 1995, SoPh, 162, 291

Deubner, F.-L. & Gough, D. 1984, Annual Review of Astronomy and Astrophysics, 22, 593

Dikpati, M. & Gilman, P. A. 2007, New Journal of Physics, 9, 297

Domingo, V., Fleck, B., & Poland, A. I. 1995, SoPh, 162, 1

Domínguez Cerdeña, I., Sánchez Almeida, J., & Kneer, F. 2006, The Astrophysical Journal, 636, 496

Duckenfield, T., Anfinogentov, S. A., Pascoe, D. J., & Nakariakov, V. M. 2018, ApJL, 854, L5

Eddington, A. S., S. 1942, MNRAS, 102, 154

Eddy, J. A. 1976, Science, 192, 1189

Edwin, P. M. & Roberts, B. 1983, SoPh, 88, 179

Engvold, O., Vial, J.-C., & Skumanich, A. 2019, The Sun as a Guide to Stellar Physics

Erdélyi, R. 2004, Astronomy and Geophysics, 45, 34

Erdélyi, R., Doyle, J. G., Perez, M. E., & Wilhelm, K. 1998, Astronomy & Astrophysics, 337, 287

Foullon, C., Verwichte, E., Nakariakov, V. M., Nykyri, K., & Farrugia, C. J. 2011, ApJL, 729, L8

Fowler, J. W. 2014, J. Low. Temp. Phys., 176, 176

Frankland, E. & Lockyer, J. N. 1869, Proceedings of the Royal Society of London Series I, 18, 79

Freeland, S. L. & Handy, B. N. 1998, SoPh, 182, 497

Friis-Christensen, E. & Lassen, K. 1991, Science, 254, 698

Gary, G. A. 2001, SoPh, 203, 71

Geweke, J. & Porter-Hudak, S. 1983, Journal of Time Series Analysis, 4, 4

Gimeno, L., de la Torre, L., Nieto, R., et al. 2003, Earth and Planetary Science Letters, 206, 15

Goddard, C. R. & Nakariakov, V. M. 2016, A&A, 590, L5

Goddard, C. R., Nisticò, G., Nakariakov, V. M., & Zimovets, I. V. 2016, A&A, 585, A137

Goldreich, P. & Sridhar, S. 1995, ApJ, 438, 763

Goossens, M., Andries, J., & Arregui, I. 2006, Philosophical Transactions of the Royal Society of London Series A, 364, 433

Goossens, M., Andries, J., & Aschwanden, M. J. 2002, A&A, 394, L39

Goossens, M., Erdélyi, R., & Ruderman, M. S. 2011, SSRv, 158, 289

Goossens, M., Terradas, J., Andries, J., Arregui, I., & Ballester, J. L. 2009, A&A, 503, 213

Goossens, M., Van Doorsselaere, T., Soler, R., & Verth, G. 2013, ApJ, 768, 191

Groth, E. J. 1975, ApJS, 29, 285

Gupta, G. R., Del Zanna, G., & Mason, H. E. 2019, A&A, 627, A62

Hahn, M., Landi, E., & Savin, D. W. 2012, ApJ, 753, 36

Hahn, M. & Savin, D. W. 2014, ApJ, 795, 111

Handy, B. N., Acton, L. W., Kankelborg, C. C., et al. 1999a, Solar Physics, 187, 229

Handy, B. N., Acton, L. W., Kankelborg, C. C., et al. 1999b, SoPh, 187, 229

Heinemann, M. & Olbert, S. 1980, J. Geophys. Res., 85, 1311

Heintze, J. R. W., Hubenet, H., & de Jager, C. 1964, BAN, 17, 442

Heyvaerts, J. & Priest, E. R. 1983, A&A, 117, 220

Hindman, B. W. & Jain, R. 2008, ApJ, 677, 769

Hindman, B. W. & Jain, R. 2013, ApJ, 778, 174

Hindman, B. W. & Jain, R. 2018, ApJ, 858, 6

Hinode Review Team, Al-Janabi, K., Antolin, P., et al. 2019, PASJ, 71, R1

Hollweg, J. V. 1984, ApJ, 277, 392

Howson, T. A., De Moortel, I., & Antolin, P. 2017, A&A, 602, A74

Howson, T. A., De Moortel, I., & Reid, J. 2020, A&A, 636, A40

Howson, T. A., De Moortel, I., Reid, J., & Hood, A. W. 2019, A&A, 629, A60

Hunter, J. D. 2007, Computing in Science and Engineering, 9, 90

Hurlburt, N., Cheung, M., Schrijver, C., et al. 2012, SoPh, 275, 67

Ionson, J. A. 1978, ApJ, 226, 650

Jacques, S. A. 1977, ApJ, 215, 942

Jafarzadeh, S., Solanki, S. K., Gafeira, R., et al. 2017, ApJS, 229, 9

Jain, R., Gascoyne, A., & Hindman, B. W. 2011, MNRAS, 415, 1276

Jain, R., Hindman, B. W., Braun, D. C., & Birch, A. C. 2009, Absorption of p Modes by Magnetic Plage, in Solar-Stellar Dynamos as Revealed by Helio- and Asteroseismology: GONG 2008/SOHO 21, eds. M. Dikpati, T. Arentoft, I. González Hernández, C. Lindsey, & F. Hill, Vol. 416 of Astronomical Society of the Pacific Conference Series, 55

Jenkins, G. M. & Watts, D. G. 1969, Spectral analysis and its applications

Jess, D. B., Mathioudakis, M., Erdélyi, R., et al. 2009, Science, 323, 1582

Jess, D. B., Morton, R. J., Verth, G., et al. 2015, SSRv, 190, 103

Jiang, J., Cameron, R. H., Schmitt, D., & Schüssler, M. 2011, A&A, 528, A83

Jones, E., Oliphant, T., & Peterson, P. 2001, SciPy: Open source scientific tools for Python

Karampelas, K. & Van Doorsselaere, T. 2018, A&A, 610, L9

Karampelas, K., Van Doorsselaere, T., & Antolin, P. 2017, A&A, 604, A130

Karampelas, K., Van Doorsselaere, T., & Guo, M. 2019, A&A, 623, A53

Karpen, J. T., Antiochos, S. K., Dahlburg, R. B., & Spicer, D. S. 1993, ApJ, 403, 769

Katsiyannis, A. C., Williams, D. R., McAteer, R. T. J., et al. 2003, Astronomy & Astrophysics, 406, 709

Kelvinsong. 2015, http://en.wikipedia.org/wiki/User:Kelvinsong/File:Sun_poster.svg, accessed: 2015-01-01. License: Creative Commons Attribution-ShareAlike 3.0 Unported.

Klimchuk, J. A. 2006, SoPh, 234, 41

Kluyver, T., Ragan-Kelley, B., Pérez, F., et al. 2016, Jupyter Notebooks – a publishing format for reproducible computational workflows, 87–90

Kohutova, P., Verwichte, E., & Froment, C. 2020, A&A, 633, L6

Kuridze, D., Mathioudakis, M., Morgan, H., et al. 2019, The Astrophysical Journal, 874, 874

Lemen, J. R., Title, A. M., Akin, D. J., et al. 2012, Solar Physics, 275, 17

Levine, R. H. 1977, ApJ, 218, 291

Levine, R. H. 1978, J. Geophys. Res., 83, 4193

Levine, R. H., Altschuler, M. D., Harvey, J. W., & Jackson, B. V. 1977, ApJ, 215, 636

Li, B. & Li, X. 2007, ApJ, 661, 1222

Liu, J., McIntosh, S. W., Moortel, I. D., Threlfall, J., & Bethge, C. 2014, The Astrophysical Journal, 797, 797

Lockwood, M., Harrison, R. G., Woollings, T., & Solanki, S. K. 2010, Environmental Research Letters, 5, 024001

Long, D. M., Valori, G., Pérez-Suárez, D., Morton, R. J., & Vásquez, A. M. 2017, A&A, 603, 603

Loughhead, R. E. & Bray, R. J. 1958, Australian Journal of Physics, 11, 177

Magyar, N. & Van Doorsselaere, T. 2016, ApJ, 823, 82

Marsh, M. S., Walsh, R. W., & Bromage, B. J. I. 2002, Astronomy & Astrophysics, 393, 649

Matsumoto, T. & Shibata, K. 2010, ApJ, 710, 1857

McFadden, L. A. A., Weissman, P. R., & Johnson, T. V. 2007, Encyclopedia of the solar system

McIntosh, S. W. & De Pontieu, B. 2012, ApJ, 761, 138

McIntosh, S. W., de Pontieu, B., Carlsson, M., et al. 2011a, Nature, 475, 477

McIntosh, S. W., de Pontieu, B., Carlsson, M., et al. 2011b, Nature, 475, 477

McIntosh, S. W., de Pontieu, B., & Tomczyk, S. 2008, SoPh, 252, 321

McKenzie, J. F. 1994, J. Geophys. Res., 99, 4193

Meyer, F., Schmidt, H. U., Wilson, P. R., & Weiss, N. O. 1974, Monthly Notices of the Royal Astronomical Society, 169, 35

Mighell, K. J. 1999, ApJ, 518, 380

Montes-Solís, M. & Arregui, I. 2017, ApJ, 846, 89

Morin, A., Eisenbraun, B., Key, J., et al. 2013, eLife, 2, 2

Morton, R., Tomczyk, S., & Pinto, R. 2016, ApJ, 828, 89

Morton, R. J., Tomczyk, S., & Pinto, R. 2015, Nature Communications, 6, 7813

Morton, R. J., Verth, G., Jess, D. B., et al. 2012a, Nature Communications, 3, 1315

Morton, R. J., Verth, G., Jess, D. B., et al. 2012b, Nature Communications, 3, 1315

Morton, R. J., Weberg, M. J., & McLaughlin, J. A. 2019, Nature Astronomy, 3, 3

Muñoz-Jaramillo, A. & Vaquero, J. M. 2019, Nature Astronomy, 3, 205

Müller, D., Nicula, B., Felix, S., et al. 2017, A&A, 606, A10

Mumford, S., Freij, N., Christe, S., et al. 2020a, Journal of Open Source Software, 5, 5

Mumford, S. J., Christe, S., Freij, N., et al. 2020b, SunPy

Myung, I. J. 2003, Journal of Mathematical Psychology, 47, 47

Nakariakov, V. M. 2003, Coronal oscillations, ed. B. N. Dwivedi & E. Parker, 314–334

Nakariakov, V. M. 2007, Advances in Space Research, 39, 1804

Nakariakov, V. M., Anfinogentov, S. A., Nisticò, G., & Lee, D. H. 2016a, A&A, 591, L5

Nakariakov, V. M. & Ofman, L. 2001, A&A, 372, L53

Nakariakov, V. M., Ofman, L., Deluca, E. E., Roberts, B., & Davila, J. M. 1999, Science, 285, 862

Nakariakov, V. M., Pilipenko, V., Heilig, B., et al. 2016b, SSRv, 200, 75

Nakariakov, V. M. & Verwichte, E. 2005, Living Reviews in Solar Physics, 2, 3

Nandy, D., Bhatnagar, A., & Pal, S. 2020, Research Notes of the American Astronomical Society, 4, 30

Narain, U. & Ulmschneider, P. 1990, SSRv, 54, 377

Narain, U. & Ulmschneider, P. 1996, SSRv, 75, 453

Nechaeva, A., Zimovets, I. V., Nakariakov, V. M., & Goddard, C. R. 2019, ApJS, 241, 31

Nisticò, G., Nakariakov, V. M., & Verwichte, E. 2013, A&A, 552, A57

Ofman, L. & Aschwanden, M. J. 2002, The Astrophysical Journal, Letters, 576, L153

Ofman, L., Davila, J. M., & Steinolfson, R. S. 1994, Geophys. Res. Lett., 21, 2259

Ofman, L., Romoli, M., Poletto, G., Noci, G., & Kohl, J. L. 1997, The Astrophysical Journal, Letters, 491, L111

Ofman, L. & Thompson, B. J. 2011, ApJL, 734, L11

Ofman, L. & Wang, T. J. 2008, A&A, 482, L9

Okamoto, T. J., Antolin, P., De Pontieu, B., et al. 2015, ApJ, 809, 71

Okamoto, T. J., Tsuneta, S., Berger, T. E., et al. 2007, Science, 318, 1577

Olcott, W. 1914, Sun Lore of All Ages: A Collection of Myths and Legends Concerning the Sun and Its Worship (G.P. Putnam's sons)

Ossendrijver, M. 2003, A&A Rv, 11, 287

Pagano, P. & De Moortel, I. 2017, A&A, 601, A107

Pagano, P. & De Moortel, I. 2019, A&A, 623, A37

Page, D. & Hirsch, J. G., eds. 2000, Lecture Notes in Physics, Berlin Springer Verlag, Vol. 556, From the Sun to the Great Attractor

pandas development team, T. 2020, pandas-dev/pandas: Pandas

Pant, V., Magyar, N., Doorsselaere, T. V., & Morton, R. J. 2019, The Astrophysical Journal, 881, 881

Parnell, C. E. & De Moortel, I. 2012, Royal Society of London Philosophical Transactions Series A, 370, 3217

Pascoe, D. J., Anfinogentov, S. A., Goddard, C. R., & Nakariakov, V. M. 2018, ApJ, 860, 31

Pascoe, D. J., Goddard, C. R., Anfinogentov, S., & Nakariakov, V. M. 2017, A&A, 600, L7

Pascoe, D. J., Goddard, C. R., & Nakariakov, V. M. 2016a, A&A, 593, A53

Pascoe, D. J., Goddard, C. R., Nisticò, G., Anfinogentov, S., & Nakariakov, V. M. 2016b, A&A, 585, L6

Pascoe, D. J., Hood, A. W., de Moortel, I., & Wright, A. N. 2012, A&A, 539, A37

Pascoe, D. J., Hood, A. W., & Van Doorsselaere, T. 2019, Frontiers in Astronomy and Space Sciences, 6, 22

Pascoe, D. J., Wright, A. N., & De Moortel, I. 2010, ApJ, 711, 990

Pascoe, D. J., Wright, A. N., De Moortel, I., & Hood, A. W. 2015, A&A, 578, A99

Pawitan, Y. 2001, In All Likelihood: Statistical Modelling and Inference Using Likelihood, Oxford science publications (OUP Oxford)

Payne, C. H. 1925, Stellar Atmospheres; a Contribution to the Observational Study of High Temperature in the Reversing Layers of Stars., PhD thesis, RADCLIFFE COLLEGE.

Pérez, F. & Granger, B. E. 2007, Computing in Science and Engineering, 9, 9

Pesnell, W. D., Thompson, B. J., & Chamberlin, P. C. 2012, Solar Physics, 275, 3

Peter, H. 2001, A&A, 374, 1108

Petrovay, K. 2020, Living Reviews in Solar Physics, 17, 2

Phillips, K. J. H. 1995, Guide to the Sun, 400

Pneuman, G. W. 1980, A&A, 81, 161

Priest, E. 2014, Magnetohydrodynamics of the Sun (Cambridge University Press)

Priest, E. R. 1984, Solar magneto-hydrodynamics (Springer)

Prokopyszyn, A. P. K., Hood, A. W., & De Moortel, I. 2019, A&A, 624, A90

Reale, F. 2010, Living Reviews in Solar Physics, 7, 5

Riesebieter, W. & Neubauer, F. M. 1979, SoPh, 63, 127

Rieutord, M. & Rincon, F. 2010, Living Reviews in Solar Physics, 7 [1005.5376]

Roberts, B. 2000, SoPh, 193, 139

Roberts, B. 2019, MHD Waves in the Solar Atmosphere (Cambridge University Press)

Roberts, B., Edwin, P. M., & Benz, A. O. 1984, ApJ, 279, 857

Romanchuk, P. R. 1963, Soviet Ast., 7, 365

Rosner, R., Tucker, W. H., & Vaiana, G. S. 1978, ApJ, 220, 643

Rouse, C. A. 1966, Nature, 212, 803

Rudenko, G. V. 2001, SoPh, 198, 5

Ruderman, M. S. & Erdélyi, R. 2009, Space Science Reviews, 149, 199

Ruderman, M. S. & Roberts, B. 2002, ApJ, 577, 475

Rutten, R. J. 2007, Astronomical Society of the Pacific Conference Series, Vol. 368, Observing the Solar Chromosphere, ed. P. Heinzel, I. Dorotovič, & R. J. Rutten, 27

Rutten, R. J. 2012, Philosophical Transactions of the Royal Society of London Series A, 370, 3129

Rutten, R. J. & Severino, G. 2012, Solar and Stellar Granulation, Nato Science Series C: (Springer Netherlands)

Saha, M. N. 1921, Proceedings of the Royal Society of London Series A, 99, 135

Sakurai, T. 2017, Proceeding of the Japan Academy, Series B, 93, 87

Scherrer, P. H., Bogart, R. S., Bush, R. I., et al. 1995, SoPh, 162, 129

Schou, J., Antia, H. M., Basu, S., et al. 1998, ApJ, 505, 390

Schou, J., Scherrer, P. H., Bush, R. I., et al. 2012, Solar Physics, 275, 229

Schrijver, C. J. & DeRosa, M. L. 2003, Solar Physics, 212, 212

Schrijver, C. J., Title, A. M., Berger, T. E., et al. 1999, Solar Physics, 187, 261

Schwabe, H. 1844, Astronomische Nachrichten, 21, 233

Schwenn, R. 2006, Living Reviews in Solar Physics, 3, 2

Solanki, S. K. 2003a, Astronomy & Astrophysics Reviews, 11, 153

Solanki, S. K. 2003b, A&A Rv, 11, 153

Solanki, S. K. & Steiner, O. 1990, A&A, 234, 519

Soler, R. & Luna, M. 2015, A&A, 582, A120

Soler, R. & Terradas, J. 2015, ApJ, 803, 43

Soler, R., Terradas, J., Oliver, R., Ballester, J. L., & Goossens, M. 2010, ApJ, 712, 875

Soler, R., Terradas, J., Verth, G., & Goossens, M. 2011, ApJ, 736, 10

Soward, A. M., Jones, C. A., Hughes, D. W., & Weiss, N. O., eds. 2005, Fluid Dynamics and Dynamos in Astrophysics and Geophysics: reviews emerging from the Durham Symposium on Astrophysical Fluid Mechanics held July 29 to August 8, 2002

St. Cyr, O. C., Sánchez-Duarte, L., Martens, P. C. H., Gurman, J. B., & Larduinat, E. 1995, SoPh, 162, 39

Stepanov, A. V., Zaitsev, V. V., & Nakariakov, V. M. 2012, Physics Uspekhi, 55, A04

Sterling, A. C. 2000, SoPh, 196, 79

Stix, M. 2004, The Sun: An Introduction, Astronomy and Astrophysics Library (Springer Berlin Heidelberg)

Strong, K., Bruner, M., Tarbell, T., Title, A., & Wolfson, C. J. 1994, Space Science Reviews, 70, 119

SunPy Community, T., Mumford, S. J., Christe, S., et al. 2015, Computational Science and Discovery, 8, 014009

Tassoul, J.-L. & Tassoul, M. 2004, A concise history of solar and stellar physics

Terradas, J., Andries, J., Goossens, M., et al. 2008, ApJL, 687, L115

Terradas, J., Goossens, M., & Verth, G. 2010, A&A, 524, A23

The SunPy Community, Barnes, W. T., Bobra, M. G., et al. 2020, The Astrophysical Journal, 890, 890

Thurgood, J. O., Morton, R. J., & McLaughlin, J. A. 2014, ApJL, 790, L2

Tian, H., Curdt, W., Teriaca, L., Landi, E., & Marsch, E. 2009, Astronomy & Astrophysics, 505, 307

Tian, H., Tomczyk, S., McIntosh, S. W., et al. 2013, SoPh, 288, 637

Tiwari, A. K., Morton, R. J., Régnier, S., & McLaughlin, J. A. 2019, The Astrophysical Journal, 876, 106

Tomczyk, S., Card, G. L., Darnell, T., et al. 2008, SoPh, 247, 411

Tomczyk, S. & McIntosh, S. W. 2009, ApJ, 697, 1384

Tomczyk, S., McIntosh, S. W., Keil, S. L., et al. 2007, Science, 317, 1192

Toriumi, S., Iida, Y., Kusano, K., Bamba, Y., & Imada, S. 2014, Solar Physics, 289, 3351

Tritschler, A., Rimmele, T. R., Berukoff, S., et al. 2016, Astronomische Nachrichten, 337, 1064

Uchida, Y. & Kaburaki, O. 1974, SoPh, 35, 451

Van Ballegooijen, A. A., Asgari-Targhi, M., Cranmer, S. R., & DeLuca, E. E. 2011, ApJ, 736, 3

Van Doorsselaere, T., Andries, J., Poedts, S., & Goossens, M. 2004, ApJ, 606, 1223

Van Doorsselaere, T., Antolin, P., Yuan, D., Reznikova, V., & Magyar, N. 2016, Frontiers in Astronomy and Space Sciences, 3, 4

Van Doorsselaere, T., Nakariakov, V. M., Li, B., & Antolin, P. 2020, Frontiers in Astronomy and Space Sciences, 6, 6

Van Doorsselaere, T., Nakariakov, V. M., & Verwichte, E. 2007, A&A, 473, 959

Van Doorsselaere, T., Nakariakov, V. M., & Verwichte, E. 2008, ApJL, 676, L73

Vaughan, S. 2005, A&A, 431, 391

Vernazza, J. E., Avrett, E. H., & Loeser, R. 1981, The Astrophysical Journal, Supplement, 45, 635

Verth, G., Terradas, J., & Goossens, M. 2010, ApJL, 718, L102

Verwichte, E., Nakariakov, V. M., & Cooper, F. C. 2005, Astronomy & Astrophysics, 430, L65

Verwichte, E., Nakariakov, V. M., Ofman, L., & Deluca, E. E. 2004, SoPh, 223, 77

Verwichte, E., Van Doorsselaere, T., Foullon, C., & White, R. S. 2013a, ApJ, 767, 16

Verwichte, E., Van Doorsselaere, T., White, R. S., & Antolin, P. 2013b, A&A, 552, A138

Viticchié, B., Sánchez Almeida, J., Del Moro, D., & Berrilli, F. 2011, Astronomy & Astrophysics, 526, A60

Wang, T., Ofman, L., Davila, J. M., & Su, Y. 2012, ApJL, 751, L27

Wang, T. J. 2016, Washington DC American Geophysical Union Geophysical Monograph Series, 216, 395

Wang, T. J., Solanki, S. K., Curdt, W., et al. 2003, Astronomy & Astrophysics, 406, 1105

Waskom, M., Botvinnik, O., Ostblom, J., et al. 2020, mwaskom/seaborn: v0.10.0 (January 2020)

Wentzel, D. G. 1974, SoPh, 39, 129

Wes McKinney. 2010, Data Structures for Statistical Computing in Python, in Proceedings of the 9th Python in Science Conference, eds. Stéfan van der Walt & Jarrod Millman, 56 – 61

White, R. S. & Verwichte, E. 2012, A&A, 537, A49

Wiegelmann, T., Thalmann, J. K., & Solanki, S. K. 2014, A&A Rv, 22, 78

Williams, D. R., Mathioudakis, M., Gallagher, P. T., et al. 2002, Monthly Notices of the Royal Astronomical Society, 336, 747

Williams, D. R., Phillips, K. J. H., Rudawy, P., et al. 2001, Monthly Notices of the Royal Astronomical Society, 326, 428

Withbroe, G. L. & Noyes, R. W. 1977, ARA&A, 15, 363

Wolf, R. 1859, MNRAS, 19, 85

Woods, T. N., Eparvier, F. G., Hock, R., et al. 2012, Solar Physics, 275, 115

Yang, Z., Bethge, C., Tian, H., et al. 2020, Science, 369, 694

Zaqarashvili, T. V. & Erdélyi, R. 2009, Space Science Reviews, 149, 355

Zimovets, I. V. & Nakariakov, V. M. 2015, A&A, 577, A4

Appendix A

Tables from (Chapter 4)

A.1 Positions of loop

The following Table A.1 notes the positions of the identified loop tracks as discussed in Section 4.2.3. The points represent the loop apex identified by finding the inflexion point.

Table A.1 Position of loop apexes identified as shown in Figure 4.2

Loop No.	Solar-X (arcsecs)	Solar-Y (arcsecs)	Date
1	-836.749	702.485	20120423
2	-989.575	460.7	20120626
3	1143.01	-191.493	20120410
4	589.619	884.311	20120810
5	-905.257	-626.738	20120719
6	-1100.37	-219.12	20120410
7	-917.755	-600.778	20120626
8	581.283	940.528	20120410
9	-1013.47	-675.221	20120410
10	1120.27	-156.174	20120423
11	922.341	480.758	20120810
13	337.831	1128.28	20120719
14	-961.839	586.351	20130717
12	551.719	985.554	20120120
15	-991.906	463.986	20130717
16	-1098.83	194.083	20120121
17	-1081.26	-190.223	20120719
18	842.873	-661.366	20120410
19	-934.339	481.913	20120120
20	-984.19	478.482	20130717

Table A.1 continued from previous page

Loop No.	Solar-X (arcsecs)	Solar-Y (arcsecs)	Date
21	-1063.73	-103.316	20120626
22	-1023.75	486.778	20120410
23	610.279	-928.917	20120810
24	-374.774	1048.45	20120719
25	-952.975	418.094	20120410
26	-1064.34	-111.295	20120410
31	1069.03	68.5343	20130717
30	1085.54	77.3289	20120410
27	875.421	-633.739	20120423
28	-1092.94	-88.1161	20120121
29	-694.081	828.018	20120121
32	-1088.95	-108.385	20120423
33	1209.13	-128.97	20120120
34	631.645	-874.571	20120120
35	-960.584	-455.081	20120121
36	1184.89	-154.668	20120810
37	602.033	-892.791	20120810
38	669.385	-872.151	20130717
39	-975.912	-480.902	20120120
40	-1086.52	24.9296	20120121
41	-974.841	-464.217	20120410
43	-1017.25	-483.423	20120121
42	563.485	-991.248	20140102
44	1111.66	-128.335	20120120
45	-1022.27	-472.45	20120810
46	-1049.69	-487.588	20120121
47	-1126.27	55.5354	20120120
48	-316.995	1032.62	20120121
49	-316.995	1032.62	20120423
50	-322.679	1050.09	20120810
51	-322.679	1050.09	20120719
52	596.258	-935.787	20120410
53	596.258	-935.787	20120719
55	-105.355	1031.59	20120423
54	-111.158	1030.64	20120410
56	-149.926	1036.9	20120423
57	-149.927	1036.9	20130717
58	1003.38	278.568	20120410

Table A.1 continued from previous page

Loop No.	Solar-X (arcsecs)	Solar-Y (arcsecs)	Date
59	-974.841	-464.217	20120120
60	-339.561	1007.43	20120410
61	-1048.32	40.1427	20120719
62	-418.59	1004.38	20120120
63	1102.7	-207.835	20120423
64	1098.0	-220.957	20120120
65	1139.13	203.939	20120121
66	565.977	-942.744	20120423
67	1057.52	264.131	20120121
69	-364.738	1059.9	20120423
68	-1149.07	-37.3129	20120719
70	583.793	-974.754	20120719
71	993.548	532.001	20120121
72	559.775	-1031.05	20120120
73	1127.22	-127.23	20120120
74	-1094.45	-56.8706	20130717
75	1111.05	-63.6959	20120410
76	-1062.69	9.00183	20120121
77	1039.45	230.53	20120410
78	1049.77	-168.193	20120810
79	564.797	-953.776	20120120
80	-369.515	1028.94	20120423
81	1101.27	268.271	20130410
84	-419.756	1012.89	20140102
82	-1077.38	-109.119	20120120
83	274.92	-1004.83	20120120
85	-1137.79	-80.0138	20120121
86	1030.3	206.402	20120719
87	566.204	-934.279	20120719
88	1097.27	317.643	20120719
89	-343.386	1002.95	20120121
90	1052.04	-79.3839	20120121
91	1077.84	-104.255	20120121
92	1077.95	-192.267	20130717
93	1042.74	366.635	20120121
94	749.017	821.448	20120120
96	991.107	484.019	20120120
97	961.987	510.705	20120121

Table A.1 continued from previous page

Loop No.	Solar-X (arcsecs)	Solar-Y (arcsecs)	Date
95	1144.3	138.301	20120120
98	512.391	-931.485	20120719
99	-1081.16	191.915	20120526
100	1075.96	-40.2086	20120423
101	-1093.74	44.2791	20140102
102	568.06	-961.379	20120121
103	594.952	-974.778	20120120
104	-1141.3	81.3959	20120121
105	1012.32	415.887	20120120
106	528.502	-944.595	20120121
107	974.839	496.024	20120121
108	504.412	944.643	20120121

A.2 Damping of standing kink waves

The table obtained for the statistical study of damping of standing kink waves.

Table A.2 Table obtained from Nechaeva et al. (2019), this analyses damping of standing kink waves in the solar corona using SDO in the solar cycle 24.

Serial No.	Date	Period (Mins)	Period error (Mins)	Loop length (Mm)	Loop length error (Mm)	Loop displ-acement (Mm)	Amplitude (Mm)	Amplitude error (Mins)	Damping time (Mins)	Damping time error (Mins)	ξ	Kink speed km s^{-1}
1	2010-Aug-2	1.69	0.05	78.0		7.0	1.2		10.76	2.79	2.62	632.67
2	2014-Sep-10	2.17	0.46	87.0	19.0	12.8	1.7	1.0	8.2	4.6	2.38	843.0
3	2013-Feb-17	2.29	0.04	92.0		0.7	3.1		7.82	1.66	3.15	1236.5
4	2016-Feb-12	2.32	0.27	94.0	11.0	3.4	1.6	0.7	3.3	1.0	1.14	1080.5
5	2014-Sep-8	2.46	0.09	115.0	12.0	1.8	3.0	0.8	6.0	1.8	2.08	1326.34
6	2011-Feb-13	2.48	0.05	118.0		3.1	3.7		8.84	1.5	3.4	1512.84
7	2016-Feb-12	2.79	0.23	127.0	18.0	3.2	2.1	0.6	14.8	6.8	3.05	872.84
8	2012-May-26	2.9	0.09	138.0		13.0	9.1		17.57	2.35	1.83	479.67
9	2011-Aug-11	2.95	0.07	146.0		17.4	3.2		2.69	0.64	1.14	2071.0
10	2017-May-24	3.04	0.51	147.0	9.0	2.7	3.7	1.2	10.9	4.6	1.82	818.0
11	2015-Apr-23	3.22	0.13	148.0	12.0	0.3	0.8	0.3	6.9	3.6	3.18	2273.5
12	2016-Oct-29	3.38	0.43	150.0	10.0	9.2	2.4	1.1	7.6	2.7	1.29	850.34
13	2011-Sep-6	3.42	0.04	153.0		9.5	3.4		9.99	4.59	4.83	2463.84
14	2012-May-8	3.47	0.05	154.0		7.4	5.3		7.83	0.62	2.11	1383.67
15	2011-Dec-22	3.58	0.11	156.0		2.0	3.0		8.0	5.0	1.56	1013.67
16	2012-May-26	3.62	0.04	162.0		19.6	9.4		24.22	2.02	3.16	704.0
17	2011-Feb-10	3.71	0.02	162.0		2.9	3.2		7.23	1.3	4.28	3195.34
18	2011-Feb-9	3.81	0.03	181.0		1.4	1.2		7.44	1.0	2.14	1738.67
19	2016-Jul-10	3.81	0.42	181.0	10.0	5.1	6.2	1.5	17.3	5.4	1.99	692.67
20	2017-Jan-12	4.11	0.33	183.0	15.0	4.6	1.5	0.8	4.4	2.2	1.49	2067.84
21	2011-Feb-9	3.96	0.03	183.0		2.9	4.4		7.18	1.5	3.14	2663.84
22	2015-Apr-2	3.85	0.07	183.0	10.0	8.9	4.7	0.9	27.3	10.2	6.13	1370.84
23	2013-Oct-11	4.38	0.18	191.0		10.4	13.0		9.37	1.22	1.17	792.83
24	2011-Feb-10	4.59	0.07	207.0		1.2	1.6		10.0	1.0	2.67	1845.0
25	2010-Nov-3	4.69	0.03	213.0		1.4	4.7		8.8	1.8	3.58	2886.17
26	2010-Aug-2	5.09	0.06	232.0		5.1	1.7		5.34	1.12	1.56	2261.17
27	2012-May-30	5.14	0.02	233.0		4.0	5.3		19.11	4.85	5.65	2297.84
28	2012-May-30	5.16	0.02	234.0		2.2	8.8		15.55	1.22	3.63	1822.5
29	2015-Oct-27	5.2	0.18	236.0	12.0	1.6	2.3	0.5	32.0	14.8	5.14	1264.67
30	2012-Oct-20	5.27	0.08	238.0		10.3	12.1		9.01	2.16	2.08	1832.17
31	2013-Jan-7	5.39	0.03	241.0		9.7	3.1		9.44	0.92	2.62	2231.5
32	2011-Nov-14	5.56	0.23	253.0		2.6	3.7		16.19	7.67	3.02	1573.34
33	2015-Sep-21	5.56	0.05	254.0	12.0	1.1	2.1	0.4	14.4	7.0	6.05	3557.51

Table A.2 continued from previous page

Serial No.	Date	Period (Mins)	Period error (Mins)	Loop length (Mm)	Loop length error (Mm)	Loop displ-acement (Mm)	Amplitude (Mm)	Amplitude error (Mins)	Damping time (Mins)	Damping time error (Mins)	ξ	Kink speed km s^{-1}
34	2017-Aug-27	5.61	0.31	254.0	14.0	8.4	5.7	1.4	8.6	2.4	0.92	908.5
35	2017-Sep-7	5.67	0.31	255.0	15.0	14.4	3.9	1.3	9.1	2.4	1.4	1305.67
36	2014-Feb-10	5.72	0.1	257.0		3.6	2.9		19.72	3.23	4.11	1784.67
37	2012-Oct-20	5.77	0.04	258.0		3.6	2.5		7.32	1.08	1.32	1555.17
38	2013-Jan-7	5.78	0.02	260.0		1.3	2.2		14.0	2.0	3.11	1926.0
39	2010-Nov-3	5.8	0.08	262.0		4.4	9.7		4.12	0.47	1.14	2412.5
40	2011-Feb-10	5.88	0.17	264.0		3.0	4.3		5.09	0.98	0.99	1712.0
41	2012-Oct-19	5.94	0.08	270.0		3.0	2.1		15.23	5.5	2.93	1730.84
42	2017-Aug-1	6.08	0.19	274.0	14.0	4.7	5.0	0.4	13.0	5.4	1.39	973.67
43	2011-Sep-22	6.22	0.11	284.0		1.4	1.7		12.2	3.47	1.28	994.34
44	2016-Oct-1	6.49	0.5	286.0	12.0	5.5	4.7	1.4	24.3	12.8	3.16	1239.67
45	2013-Jan-7	6.54	0.06	295.0		2.8	12.3		15.75	3.09	2.18	1360.0
46	2017-Jun-1	6.93	0.33	304.0	11.0	9.3	2.7	1.0	15.6	8.3	4.13	2680.84
47	2014-Jun-10	7.03	0.26	313.0	36.0	4.3	2.5	0.6	24.8	12.1	3.37	1417.5
48	2014-Feb-11	7.06	0.13	314.0		17.8	27.6		19.62	2.96	1.65	881.0
49	2015-Dec-20	7.18	0.15	317.0	11.0	8.2	4.0	0.7	20.8	6.4	3.05	1549.34
50	2014-Jul-8	7.23	0.86	319.0	19.0	6.5	6.4	1.6	18.4	8.2	1.65	952.84
51	2015-Apr-23	7.3	0.2	324.0	9.0	5.0	4.4	0.5	35.9	14.1	4.99	1502.17
52	2017-Sep-7	7.44	0.1	326.0	9.0	26.9	21.5	2.4	21.4	4.9	2.57	1306.17
53	2011-Feb-10	7.46	0.14	326.0		3.6	3.2		11.83	4.76	1.32	1214.17
54	2015-Oct-27	7.64	0.32	328.0	10.0	8.4	6.1	1.3	21.8	4.6	1.7	853.5
55	2015-Oct-28	7.67	0.4	330.0	11.0	13.2	6.2	1.7	15.5	4.3	1.57	1116.84
56	2017-Apr-3	7.95	0.26	333.0	19.0	4.2	5.4	1.4	19.0	4.8	1.96	1145.5
57	2012-Aug-7	7.73	0.27	333.0		15.4	7.4		16.7	1.03	1.68	1115.5
58	2012-Oct-20	8.1	0.03	347.0		9.6	4.4		24.83	3.41	4.43	2061.84
59	2011-Sep-23	8.27	0.12	348.0		7.5	10.0		16.55	1.44	1.47	1029.34
60	2013-Jan-7	8.32	0.14	352.0		17.2	4.8		9.0	3.0	1.29	1688.17
61	2012-Oct-20	8.33	0.06	353.0		3.1	3.4		14.17	2.73	2.48	2057.17
62	2013-Jan-7	8.48	0.07	363.0		8.0	16.3		7.53	1.45	1.05	1694.67
63	2011-Nov-17	8.48	0.4	365.0		6.4	4.3		19.19	1.55	1.25	792.17
64	2013-Jan-7	8.52	0.08	368.0		2.1	12.7		15.04	1.81	1.8	1469.0
65	2014-Nov-3	9.09	0.66	385.0	9.0	6.5	5.9	2.2	27.4	12.5	2.86	1338.17
66	2013-Oct-11	9.23	0.17	386.0		17.9	8.0		15.38	2.58	1.47	1231.34
67	2015-Oct-2	9.38	0.76	394.0	20.0	7.4	12.8	3.6	21.1	5.8	1.23	764.0
68	2011-Feb-11	9.52	0.17	397.0		4.7	8.9		8.02	1.09	0.7	1154.67
69	2014-Feb-11	9.69	0.14	403.0		9.3	7.8		20.71	4.71	2.28	1481.0
70	2017-Aug-1	9.78	0.62	403.0	13.0	3.6	6.9	2.2	12.7	4.6	1.37	1453.84
71	2015-Oct-28	10.21	0.16	410.0	9.0	2.9	1.2	0.3	27.8	13.7	5.0	2458.0
72	2014-Jun-10	10.45	1.02	411.0	10.0	1.6	3.7	1.7	8.6	3.6	1.01	1608.0
73	2015-Jun-4	10.56	0.49	412.0	12.0	11.7	8.8	2.0	25.6	6.9	1.44	770.67
74	2015-Dec-20	10.58	0.72	416.0	8.0	4.6	6.7	1.8	18.2	5.9	1.37	1042.67
75	2014-Jun-11	10.68	0.73	423.0	11.0	10.0	5.8	1.5	15.6	4.4	1.2	1088.84
76	2015-Apr-23	11.35	0.47	431.0	8.0	3.4	14.5	2.6	29.6	7.5	1.45	703.17
77	2014-Feb-11	11.46	0.16	431.0		6.9	10.7		24.17	5.13	1.79	1064.17
78	2011-Nov-18	11.56	0.3	432.0		14.5	15.6		27.43	4.26	1.54	806.33
79	2016-Jul-10	11.83	0.16	435.0	12.0	9.6	9.7	1.2	26.8	7.6	3.16	1709.84
80	2015-Dec-20	11.88	0.78	436.0	9.0	8.8	13.4	2.1	49.3	20.6	2.65	781.83
81	2017-Apr-3	12.07	0.57	445.0	12.0	14.8	9.7	2.5	20.1	5.5	1.61	1185.67
82	2014-Jun-11	12.51	0.42	448.0	11.0	2.6	4.1	0.8	27.3	11.1	2.02	1105.34
83	2014-Jun-11	12.51	0.42	450.0	9.0	6.2	6.6	1.3	43.0	13.5	2.66	927.67
84	2014-Jun-11	12.57	0.38	451.0	10.0	5.5	6.8	1.5	23.2	8.9	1.69	1093.34
85	2017-Aug-1	12.81	0.32	457.0	10.0	1.7	3.9	1.0	25.1	10.8	4.23	2564.51
86	2014-Feb-11	12.95	0.55	457.0		4.9	15.0		13.64	3.93	0.96	1075.84
87	2012-Oct-20	13.43	0.05	473.0		12.5	13.7		13.15	2.66	2.13	2551.17
88	2012-Jan-16	13.3	0.13	473.0		2.5	9.2		18.71	4.5	1.57	1319.34
89	2014-Jul-11	14.3	0.38	489.0	10.0	6.4	7.5	1.3	31.7	10.6	2.68	1377.84
90	2014-Sep-27	14.38	0.33	494.0	10.0	3.9	3.6	1.2	11.1	5.2	2.14	3172.84
91	2015-Dec-21	15.36	0.48	506.0	9.0	9.4	3.7	0.9	16.5	4.6	1.62	1652.0
92	2015-Oct-17	15.68	0.66	507.0	11.0	3.5	2.1	0.8	11.3	5.0	1.54	2302.5
93	2013-Jan-7	15.83	0.19	512.0		15.8	13.4		14.62	4.96	1.49	1745.0
94	2017-Apr-17	16.45	0.83	537.0	14.0	2.8	3.0	1.1	14.4	5.1	1.27	1577.17
95	2011-Nov-18	16.73	0.58	538.0		31.8	26.6		35.01	6.44	1.71	876.5
96	2013-Jul-18	17.19	0.16	540.0		12.3	22.0		21.98	15.6	1.44	1178.0
97	2016-Jul-10	17.82	0.28	547.0	11.0	6.2	12.1	1.1	15.4	3.8	1.43	1694.5
98	2017-Aug-1	17.86	1.18	551.0	13.0	9.3	5.3	1.8	15.5	6.5	1.13	1335.84
99	2015-Apr-23	18.59	1.03	570.0	11.0	14.2	9.8	2.4	28.4	7.3	1.37	915.17
100	2013-Jul-18	20.46	0.12	588.0		25.4	27.4		26.64	2.17	1.69	1243.67
101	2013-Jul-18	20.76	0.21	597.0		19.9	23.7		15.76	3.09	0.98	1237.5